KU LEUVEN

ARENBERG DOCTORAL SCHOOL
Faculty of Engineering Science

Metallic Nanopores for single-molecule DNA sensing

Fabrication, Characterization and Applications

Yi Li

Supervisor:
Prof. dr. ir. Guido Groeseneken
Prof. dr. ir. Liesbet Lagae

Dissertation presented in partial fulfillment of the requirements for the degree of Doctor in Engineering Science

May 2015

Metallic Nanopores for single-molecule DNA sensing

Fabrication, Characterization and Applications

Yi LI

Examination committee:
Prof. dr. Adhemar Bultheel, chair
Prof. dr. ir. Guido Groeseneken, supervisor
Prof. dr. ir. Liesbet Lagae, supervisor
Dr. ir. Tim Stakenborg
Prof. dr. ir. Pol Van Dorpe
Prof. dr. ir. Robert Puers
Prof. dr. ir. Giovanni Maglia
Prof. dr. ir. Magnus P. Jonsson
(Linköping University)

Dissertation presented in partial
fulfillment of the requirements for
the degree of Doctor
in Engineering Science

In collaboration with:

May 2015

Uitgegeven in eigen beheer, Yi Li, Kasteelpark Arenberg 10, B-3001 Heverlee (Belgium)

Acknowledgments

Very first and foremost, I would like to thank my promoter, Prof. Guido Groeseneken. It was back to 2010 when I asked Guido whether I can become one of his doctoral students. The scene of me sitting beside him and his question on why I wanted to be a PhD in the electrical engineering are still fresh in my mind. I was nervously and anxiously waiting for Guido's answer. Finally, he said yes, which became the moment when my PhD started to run.

It is an honor to convey my sincere gratitude to my promoter, Prof. Liesbet Lagae who granted me the opportunity to start my PhD study in the field of nanopores at imec. As an open-minded promoter, she shows great respect to my research and provides farsighted, wise guidance to me, along with sufficient freedom to my development as a researcher I would like to be. Thanks for solving all kinds of issues for me during these years!

A special thanks to Prof. R. Puers for allowing me to use the furnace in the MICAS cleanroom. I cannot forget the afternoon you spent with me when I wanted to convince you the importance of thermal oxide for my research. From that on, PhD research is not only about enthusiasm, critical thinking and exploring the unknown to me, but also about how to coordinate and motivate with others in limited resources. I feel really lucky to have you on board as my assessor.

I am also grateful to Prof. G. Maglia who provided suggestions when the project started and a lot of helps on my research in the past years. Thanks for allowing me to test my chips with the temperature-controlled setup. I really appreciate the discussions with you, especially from a bionanopore expert's perspective!

I would like to address special thanks to Prof. M.P. Jonsson. Magnus, I really enjoy the time that we spent together both in the lab and online discussions. You always show interest in my work and make me feel warm and welcome. It is my honor to have a publication with you! ;-)

My sincere thanks go to all my jury members for their precious time in evaluating the thesis manuscript. Their critical comments and constructive suggestions have led to significant improvement on my thesis. I would also like to thank Prof. A. Bultheel for taking the time and effort to chair my defenses.

I own endless deep gratitude to my daily advisers, Dr. Tim Stakenborg and Prof. Pol Van Dorpe. You are always there and patient even when my questions are sometimes stupid. Without your invaluable guidance and enormous helps, this research cannot be smoothly conducted and generate fruitful results. There are not enough words to express my gratitude and appreciation for all that you have done. I owe you a lot.

I would like to thank Junior Mobility Programme (JuMo/13/025), which offers me the opportunity to visit Prof. Cees Dekker's Lab (2013-2014) in Delft University of Technology (TU Delft). I am grateful to all people from TU Delft. I have learn a lot from discussions in their regular team meetings. Particularly, I am very much indebted to Cees for allowing me to stay in his lab, sharing their expertise. His illustration on the power sweep is really fascinating and gives me great inspiration for further investigations. My gratitude also goes to Prof. Henny Zandbergen and Dr. Meng-Yue Wu. Without their art of TEM, I could not perform my research with sufficient well-sculpted pores. Besides Magnus, my sincere thanks also go to Francesca, Daniel and Misha for your assistance on the experimental details and the fruitful discussions. Thanks for all the support and the fun time in the lab!

Next up to our nanopore team. Ronald, thanks for leading me into the interesting nanopore field! Nima, Liesbeth and Henny, whom I worked with at the start of my PhD. I am heartily grateful to Dr. Chang Chen, who is always optimistic both to the research and to life. You have set a model to me and I have learnt so much from you. Pieter, Sven and Silke, thanks for the time and all the efforts that we together spent on the nanovibe project! Sarp, Kherim as well as Nicolo, who lighten up my days on nanopores and provide me enormous helps.

Working at Life science technology (LST) department has brought me great pleasure. My gratitude also goes to all the members: Wim, Jian, Niels, Yan, Dries, Jiaqi, John, Hasan, Finub in the Biophotonics team; Sara, Hilde, Shuo, Tim, Karolien, Jesse, Ruben, Jef, Chengjun, Frederik ($\LaTeX$!), Rita, Chengxun, Ujjal, Lei, Ben, Evelien, Rodrigo, Karen & Karen, Andim, Luis, Danny... thank all of you!

Many thanks to the colleagues at imec, KU Leuven and UGhent: Pauline, Inge and Marianne, for their great helps with many administrative matters; Erwin, Kim and many others in the III/V region for the valuable cleanroom support; Jos and Josine for the great assistance on ebeam exposure; Hugo and Olivier for the useful discussions on FIB and TEM characterization of my nanocavity pores; Benny and Karel for providing the mechanical components; Frank for his help with electronic elements and tools; Prof. Hiroshi Uji-i for his kind support on flowcell fabrication at the Department of Chemistry; Prof. Christophe Detavernier and Dr. Shaoren Deng for their generous assistance on plasma-enhanced atomic layer deposition (PEALD) of oxides, which pave the great potential of my research.

Appreciation also goes to all my Chinese friends in Leuven, especially in imec: Yangyin, Lin Zhou, Xuanwu, Xuezhi, Shuzhen, Ming & Xiumei, Bo & Xia, Sijia & Huan, Leqi, Yiting (hot pots!), Chunshu & Blair, Liping, Shengping & Jia, Ziyang, Wei Wang, Xubin, Weiming, Jie Hu, Yuandong, Cheng Xing, Hao Yu, Haodong, Jingdong, Dun & Shuyan, Yiming, Shun Zhao, Liang Su to name a few. 以及已经离开比利时的余辉、甘彤、张珂、王亮、张丽、刘舒扬、叶坚、黄成军、凌方舟、王硕、唐保军、李岩、孙建武等。 Thanks for your companion!

Last but not the least, I would like to convey my sincere thanks to my family. I deeply appreciate my parents for their understanding and unlimited support for my staying far away at the other side of the continent in the past five years. No word can express my gratitude to Lai (魏来), who experienced a lot of memorable good time and bad time with me in this journey. I am fortunate to have your love and trust in my life.

路漫漫其修远兮
The road ahead will be long
吾将上下而求索
but I will climb up and down.

李毅
于鲁汶

Yi Li,
May 2015,
Leuven

Abstract

In an emerging field of nanopore-based biosensors, DNA and other biomolecules are detected at the single-molecule level by monitoring the ionic current changes that occur upon the passage of single molecules through a nanopore. Analysis of the transient ionic current response of a nanopore upon passage of a single molecule can reveal many biophysical properties including DNA/RNA sequence information and structural and mechanical features of a single biomolecule. There are still, however, major challenges related to the molecular specificity and resolution of the read-out and related to the control of the biomolecule translocation process. Improving these items has become a hot topic for generating new types of label-free nanopore biosensors.

In addition to the current on-going research, which is mainly focused on either biological nanopores in lipid membranes or either solid-state nanopores in dielectric membranes, another front that may contribute significantly to single-molecule identification and manipulation is metallic nanopores. The introduction of metal building blocks can provide various possibilities such as local electrical control and detection and highly confined, deep subwavelength optical detection. This optical strategy can include both fluorescence techniques and label-free vibrational methods, for example, surface enhanced Raman spectroscopy (SERS). SERS is especially attractive, as it has been shown to reveal a molecular fingerprint at the single molecule level, enabling direct molecular identification.

In this PhD, we proposed a novel device consisting of a solid-state nanopore and an integrated metallic nanocavity, supporting both ionic and optical readout. Such hybrid nanopores were designed and fabricated. We experimentally characterized the ionic performance of the nanocavities and nanopore-in-cavity devices, both in dark conditions and upon laser illumination. We further interpreted the characterization results and developed a numerical model to describe the ionic and heat transport in our metallic nanopore system. We finalize by presenting the results of DNA transport through these devices without and with laser illumination.

Laser illumination was shown to exhibit a significant impact on the electrical properties of gold nanocavities, especially on the noise characteristics. We were able to attribute the increased noise to plasmon enhanced light absorption in the silicon membrane and we successfully designed and demonstrated a mitigation strategy.

We also demonstrated that for the particular case of a dielectric nanopore embedded in a metallic nanocavity, the ionic performances without laser illumination are comparable to conventional SiN pores. We also observed that strong laser illumination leads to a reversible collapse of the ionic current. In addition, this light induced switching phenomenon shows hysteresis as function of the applied laser power. We were able to explain this qualitatively by invoking nanobubble generation effects.

Summarizing, the nanopore-in-cavity devices pave the way to simultaneous ionic and optical readout of single biomolecules that can contribute to the realization of high-resolution optical spectroscopy of single molecules.

Beknopte samenvatting

In het opkomende onderzoeksdomein van nanoporie-gebaseerde biosensoren, worden DNA en andere biomoleculen gedetecteerd met een nauwkeurigheid tot op het niveau van één enkelvoudige molecule. Dit wordt gerealiseerd door het uitlezen van de verandering in de ionische stroom door de nanoporie die optreedt na de passage van één molecule door diezelfde nanoporie. Analyse van deze verandering in ionische stroom kan veel biofysische eigenschappen, waaronder DNA/RNA sequentie-informatie en structurele en mechanische eigenschappen van biomoleculen onthullen. Er zijn echter nog steeds grote problemen met betrekking tot de moleculaire specificiteit en resolutie van de uitlezing en de controle over het translocatieproces van biomoleculen. Het verbeteren van deze items is uitgegroeid tot een hot topic voor onderzoek naar van nieuwe vormen van label-vrije, nanoporie-gebaseerde biosensoren.

Naast het lopende onderzoek, dat voornamelijk gericht is op zowel biologische nanoporiën in lipide membranen of vaste-stof nanoporiën in diëlektrische membranen, bestaat er een ander concept dat aanzienlijk kan bijdragen tot de identificatie en manipulatie van enkelvoudige moleculen: metaal-gecoate nanoporiën. De introductie van de metalen bouwstenen biedt verschillende mogelijkheden zoals lokale elektrische controle, en zeer gelokaliseerde optische detectie, niet gelimiteerd door de diffractielimiet. Deze optische strategie is geschikt voor het lokaal versterken van fluorescentietechnieken en labelvrije vibrationele methoden, zoals Oppervlakte-versterkte Raman-spectroscopie (SERS). Vanwege de mogelijkheid een moleculaire vingerafdruk van slechts één enkel molecule op te meten, is SERS een uiterst interessante techniek om rechtstreekse moleculaire identificatie uit te voeren.

In dit doctoraat hebben we voorgesteld om een nieuwe component te creëren die bestaat uit een vaste-stof nanoporie en een geïntegreerde metalen nanocaviteit, die het uitlezen van zowel de ionische en optische componenten mogelijk maakt. Dergelijke hybride nanoporiën werden ontworpen en gefabriceerd. We hebben de ionische performanties van de nanocaviteiten en nanoporie-in-caviteit-

combinaties experimenteel gekarakteriseerd, zowel in donkere omstandigheden als bij laser excitatie. Verder hebben we deze resultaten geïnterpreteerd en gebruikt om een numeriek model te ontwikkelen dat het ionische en warmte transport in onze metalen nanoporie systeem beschrijft. We eindigen met DNA-transport doorheen de poriën zonder en met laser verlichting.

Laserbelichting bleek een belangrijke invloed te hebben op de elektrische eigenschappen van gouden nanocaviteiten, vooral met betrekking tot de ruis. We konden de toename in ruis toekennen aan plasmon-verhoogde lichtabsorptie in het silicium membraan en we ontworpen met succes een mitigatiestrategie.

We hebben ook aangetoond dat voor het specifieke geval van een diëlektrische nanoporie ingebed in een metalen nanocaviteit, de ionische performantie zonder laserbelichting vergelijkbaar is met conventionele vaste-stof nanoporiën. We hebben ook vastgesteld dat sterke laser belichting leidt tot een reversibele afname van de ionenstroom. Daarnaast vertoont dit lichtgeïnduceerde schakelen hysteresis als functie van het toegepaste laservermogen. We waren in staat om dit fenomeen kwalitatief te verklaren door de generatie van nanobubbels.

Samenvattend, de nanoporie-in-caviteit componenten effenen de weg naar gelijktijdige ionische en optische uitlezing van enkelvoudige biomoleculen. Dit kan bijdragen tot het realiseren van een hoge-resolutie optische spectroscopie van enkelvoudige moleculen.

Abbreviations

α-HL	α-hemolysin
4-ATP	4-Aminobenzenethiol
Ag	Silver
AgCl	Silver chloride
Al_2O_3	Aluminum oxide
ALD	Atomic layer deposition
ATP	Adenosine triphosphate
Au	Gold
BHF	Buffered hydrofluoric acid
BN	Boron nitride
BOX	Buried oxide layer
bp	Base-pair
ClyA	Cytolysin A
CMOS	Complementary metal–oxide–semiconductor
dAMP	Deoxyadenosine monophosphate
dCMP	Deoxycytidine monophosphate
dGMP	Deoxyguanosine monophosphate
DNA	Deoxyribonucleic acid
dNMP	Deoxyribonucleoside monophosphate
dTMP	Thymidine monophosphate
DUV	Deep ultraviolet
ECD	Event charge deficit
EDL	Electrical double layer
EDTA	Ethylenediaminetetraacetic acid

FDTD	Finite-difference time domain
FEM	Finite element method
FWHM	Full width at half maximum
HfO_2	Hafnium oxide
KCl	Potassium chloride
KNO_3	Potassium nitrate
KOH	Potassium hydroxide
LPCVD	Low-pressure chemical vapor deposition
LSP	Localized surface plasmon
MoS_2	Molybdenum disulfide
MspA	Mycobacterium smegmatis porin A
NBA	Nile Blue A
PDE	Partial differential equations
PDMS	Polydimethylsiloxane
PECVD	Plasma-enhanced chemical vapor deposition
PMMA	Poly(methyl methacrylate)
PSD	Power spectral density
RMS	Root-mean-square
RNA	Ribonucleic acid
SE	Secondary electron
SERS	Surface enhanced Raman spectroscopy
Si_3N_4	Silicon nitride
SiO_2	Silicon dioxide
SNR	Signal-to-noise ratio
SOI	Silicon on insulator
SPP	Surface plasmon polariton
TEM	Transmission electron microscopy
TiN	Titanium nitride
TLD	Through-lens-detector
TMAH	Etramethylammonium hydroxide
VHF	Vapor hydrofluoric acid

List of Symbols

δI	Current deviation
δt	Time interval between successive events
γ	Rectification ratio at V_{app}
σ	Surface charge density
σ_d	Device conductivity
c_0	Bulk concentration
c_i	Concentration of each specie i
c_{KCl}	KCl salt concentrations
Cl^-	Chloride ion
D_i	Diffusion constant of each specie i
E_x	Electric field on the lateral direction
E_z	Electric field on the z-direction
I_0	Baseline current
I_{RMS}	Root-mean-square of current
K^+	Potassium ion
N_A	Avogadro constant
P_{down}	Laser power where current switches from high to low
P_{up}	Laser power where current switches from low to high
t_d	Dwelling (duration) time

u_+	Electrophoretic motility of potassium ions
u_-	Electrophoretic motility of chloride ions
V_{app}	Applied voltage
z_i	Ion valence of each specie i
d	Diameter of a nanopore
e	Elementary charge
F	Faraday constant
G	Nanopore conductance
L	Length of bottom rectangle vertex inside the nanocavity
l	Effective thickness of a nanopore
R	Gas constant
W	Width of bottom rectangle vertex inside the nanocavity
X	Parameter introduced to account for the fixed surface charge

Contents

Abstract **v**

Contents **xiii**

1 General Introduction **1**

- 1.1 State-of-the-art of Nanopores 3
  - 1.1.1 Principle of Nanopores - Miniaturized Coulter-Counter . 3
  - 1.1.2 Realization of nanopores 5
  - 1.1.3 Nanopore applications 9
- 1.2 Metallic nanopores with surface enhanced Raman spectroscopy (SERS) 20
  - 1.2.1 Raman spectroscopy 20
  - 1.2.2 Plasmonic induced electro-magnetic field enhancement . 22
  - 1.2.3 Surface Enhanced Raman Spectroscopy (SERS) 24
  - 1.2.4 Metallic substrates for SERS applications 25
  - 1.2.5 Combination of SERS with nanopores 27
- 1.3 Challenges (Motivation) 29
- 1.4 Objectives 33
- 1.5 Contents of this work 34

2 **Research Methodology** **37**

2.1 Nanocavity Fabrication 38

2.1.1 E-beam based processing 38

2.1.2 Wafer Scale Processing in 200 mm CMOS Fab Environment 42

2.1.3 Sub-10 nm nanopore fabrication 44

2.2 Electrical measurements of nanopores 47

2.2.1 Flow cell and Setup 47

2.2.2 IV Linearity 52

2.2.3 Device Noise 53

2.2.4 DNA translocations as typical events 54

2.3 Numerical simulation 55

2.3.1 Electrical and fluidic simulation 55

2.3.2 Plasmonic simulation 58

2.4 Conclusions 61

3 **Characterization of metallic nanocavities without laser irradiation** **63**

3.1 Introduction 63

3.2 IV Linearity and Device Conductivity 65

3.3 Noise Performance 69

3.4 DNA translocations 70

3.5 Conclusions 72

4 **Characterization of metallic nanocavities with plasmonic excitation** **75**

4.1 Introduction 75

4.2 Plasmonic induced ionic noise 76

4.3 Probing local potential inside metallic nanocavities with SERS 87

4.4 Conclusions 95

5 Characterization of nanopore-in-cavity device without laser irradiation 97
5.1 Introduction . . . 98
5.2 IV Linearity and Device Conductivity . . . 100
5.3 Noise Performance . . . 103
5.4 DNA translocations . . . 105
5.5 Conclusions . . . 107

6 Characterization of nanopore-in-cavity device with plasmonic excitation 109
6.1 Introduction . . . 110
6.2 IV Linearity . . . 111
6.3 Noise Performance . . . 126
6.4 DNA translocations . . . 128
6.5 Conclusions . . . 129

7 Conclusions and Outlook 131
7.1 Conclusions . . . 131
7.2 Outlook . . . 133

Bibliography 137

Scientific Contributions 161

Curriculum Vitae 163

Chapter 1

General Introduction

When people look into the opposites - “big” vs “small”, how big is big in our cognition? And how small do we define as small? The length dimension of a big body like the universe [1] is about 10^{26} m – made up of small building blocks such as atoms (which diameter is about 10^{-10} m), electrons (which diameter ranges in 10^{-15} m), and as tiny as the predicted size of a spin foam with the Planck length at 10^{-35} m [2]. Unaided by any tools, the smallest things that a human being can usually see are human hairs and dusts (about 0.1 millimeters), whereas our naked eye can also encounter large objects such as airplanes (10^2 m). In contrast to these dazzling 60 orders of magnitude from the unsolved bottom to the edge of the vast universe [3], one’s observation and understanding have been restricted in only 6 orders of magnitude. Fortunately, humans can develop tools to overcome such limitations. Tiny things such as germs and bacteria (Figure 1.1) that cannot be observed with the naked eye, can be visualized by means of powerful microscopes. Different microscopes would allow one to look at things as small as sub-micrometers. However, by no means is the standard microscopy the end game of visualizing “small”.

Below the longstanding optical diffraction limit, a lot of activities - particularly most of biological processes - emerge at the nanometer scale. One example is the discovery of deoxyribonucleic acid (DNA), which is not only of fundamental importance in medicine and biology, but also raises a wide range of interests in the understanding of the blueprint of life. DNA (for some viruses also RNA) contains the basic instruction sets for all known forms of life, encodes ribonucleic acid (RNA) and proteins that drive all cellular activity. Chemically, DNA consists of two long polymers, that are composed of simple subunits, called nucleotides arranged in a double helix structure with a diameter of $\sim$2.5

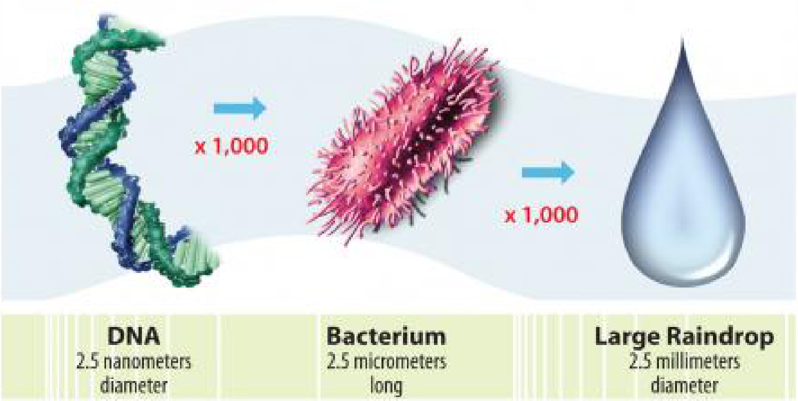

Figure 1.1: The size of "nano" scale [4]. A nanometer is defined as one-billionth of a meter. The typical diameter of double stranded DNA molecules is about 2.5 nm, 1000 fold-smaller than the typical size of bacteria which in turn is another 1000 folds smaller than a large raindrop of about 2.5 mm in diameter.

nanometer (see Figure 1.1). Nowadays top-quality optical microscopes can only resolve two points that are about 0.25 micrometers apart, still far beyond the size of individual nucleotide, awaiting the development of technologies at the nanoscale.

Nanotechnology as a fast technological revolution was already predicted by Richard P. Feynman in his legendary presentation "There's plenty of room at the bottom" [5] in 1959. He stated that soon we would be able to control matter at the nanoscale, atom by atom [5]. One of the most interesting features at the "nano" scale is that the physical and chemical properties of materials may be different from those of bulk ones. First, the behaviors of melting point, fluorescence, electrical conductivity, magnetic permeability, and even chemical reactivity can be dominated by quantum effects, which change in discrete amounts and not in a continuous way [6]. Second, nanoscaled materials have much larger surface areas. When the surface area per mass of a material increases, a greater amount of the material can come into contact with surrounding materials, thus affecting reactivity. The nanoscale is also the scale of which nature has perfected the art of biology [4]. Not only nucleic acids, but also enzymes, antibodies and many of the biological building blocks are contributing to the inner workings of cells in the nanoscale range. In short, nanotechnology is not simply a copy of larger objects to smaller dimensions. Furthermore, working at the nanoscale enables us to trigger new effects and construct new processes, the impact of which has already emerged in medicine, imaging, computing, printing, chemical catalysis, materials synthesis, and many other fields.

In this chapter, the inspiration and the motivation of the thesis as well as the basic concepts of the field of nanopores and surface enhanced Raman spectroscopy are expounded. The objectives and the outline of the thesis are also depicted.

1.1 State-of-the-art of Nanopores

1.1.1 Principle of Nanopores - Miniaturized Coulter-Counter

Nanopores are defined as tiny holes through thin membranes. Their dimensions are typically comparable to the size of single molecules (such as DNA). When the membrane with a nanopore separates a conductive liquid into two reservoirs, the working mechanism of nanopores is similar to the well-known *Coulter-Counter* principle, which was patented in 1953 under the title of “Means for Counting Particles Suspended in a Fluid”. If particles can be placed in the fluidic channel, the occupied volume can block the transport of the fluid, therefore lead to an impedance change of the fluid. In the patent, the principle of Coulter-Counter states that particles can be pulled through an orifice and produce a change in impedance that is proportional to the volume of the particle traversing the orifice [7]. The volume occupied by the particle gives rise to the blockade of the displacement of the electrolyte, that leads to the pulse change in impedance. Over the past 20 years the Coulter-Counter has been a popular technique mainly to count and size various cells.

As stated, a nanopore is basically a nanometer-sized version of the Coulter Counter. Figure 1.2 illustrates the working principle of a pore through a free-standing membrane. When DNA is present in a nanopore, the occupied volume of DNA, on one hand, can block the ion flow, the amplitude of which depends on the salt concentration. On the other side, since DNA is negatively charged, its surface conductivity may boost the ion transport, which can be assumed to be constant. When individual charged molecules are dragged through the pore by an applied electric field, they can be detected when being translocated over a nanopore by a deviation δI (i.e. a current dip) with respect to the current baseline I_0. Such a translocation event of a molecule from one side of the membrane through the nanopore to the other side is generally described by three parameters: the dwelling time (t_d), the average event amplitude (δI), and the time between successive events (δt). Although nanopores can be used to monitor various single molecules, they are mostly used for DNA applications. The diameter of DNA, namely ~1.4 nm for single stranded and ~2.5 nm for

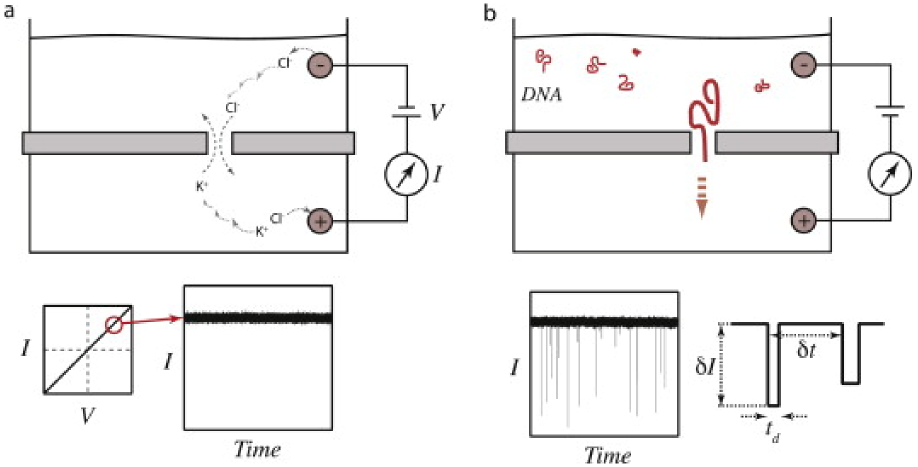

Figure 1.2: The basics of nanopore measurements [8]. (a) Electric measurement of ion transport through a pore for a reservoir filled with a KCl buffer solution. The trans-membrane voltage triggers the half electrochemical reactions on the two electrodes, which leads to K^+ and Cl^- migrating towards the membrane. This ionic current is monitored using an Ammeter. The current–voltage response of a nanopore is expected to be linear. The ionic current at a constant applied voltage results in a stable level I_0, holding with certain level of noise. (b) Electric measurement when molecules, here DNA, are injected on one side of the nanopore. The electric field is concentrated around the nanopore and these charged molecules usually diffuse towards the pore. Due to the negatively charges of DNA, they can stochastically enter the nanopore following the electric field. The molecule passing through the pore can block the ion flow and produce a measurable ionic current change.

double stranded DNA, makes the size of nanopores ideal for threading DNA molecules through them. If the ionic detection of DNA can be pushed to identify single DNA bases with different current levels, nanopores can be ultimately envisioned to read out the genetic code of DNA in a single go. This principal idea originates from a paper of biophysicist David Deamer published in 1989 [9]. When he was figuring out how to get the molecule of adenosine triphosphate (ATP) through a lipid membrane to supply energy to enzymes [9], he realized that his theories might also work for DNA as shown in Figure 1.3a. If the ion current levels through the channel would be different for different DNA bases, the current changes as a function of time for a linear single strand DNA could in principle open up a new way of sequencing (i.e. determining the order of different nucleotides in a DNA strand). Such direct sequencing method using nanopores is still under exploration by many researchers and start-up companies because of its potentially non-labeled, low-cost, long read-length and high speed. As such, nanopore sequencing is considered as one of the few technologies to further surmount the limits of next-generation sequencing (see also “Figure 1.9”).

1.1.2 Realization of nanopores

Nanopores can be categorized into two classes: the biological and the solid-state nanopores. In the following section, both types of pores will be shortly described followed by a number of commonly used applications described in literature.

Biological nanopores

Biological nanopores (also called Porins) are beta barrel proteins that cross a cellular membrane and act as a pore through which molecules can diffuse. Isolating such pore-forming proteins to create pores *in vitro* in lipid membranes with ultimate resolution and reproducibility has driven the nanopore research field. Although biological nanopores cannot spontaneously drive DNA molecules from one side to the other, they can be used as the core element to govern the transport of DNA under certain trans-membrane voltage. The first working and still most used biological nanopore makes use of a protein porin named α-hemolysin (α-HL) from *Staphylococcus aureus*. The minimum diameter of this pore is only 1.4 nm (shown in Figure 1.3b) which only allows single-stranded RNA or DNA fragments to translocate. Another pore called MspA (i.e. *Mycobacterium smegmatis* porin A) has even a minimal diameter of 1.3 nm (shown in Figure 1.3c) and might be even better suited to generate strong ionic current signals when nucleic acids pass through. Besides the use of natural wild-type biological pores, more recently, protein modifications have been introduced to tweak the pore’s characteristics. For example, by altering the MspA’s gene, the constricted part of the pore was made more neutral to enable DNA to pass through [11]. Besides the description of small pores for translocating single strands of nucleic acids, larger pores have been introduced as well. A notable example is the ϕ29 connector protein [12]. As shown in Figure 1.3d, this protein contains a channel of 3.6 nm in diameter, which can allow the translocations of double-stranded DNA.

In general, biological nanopores have two sides of the same coin. On one hand, biological nanopores are mostly used, because of their extremely reproducible nature as a result of the intrinsic, 3D self-folding characteristics of a protein. Besides as stated above, the use of genetic modification advances the fine tune of the nanopores at the single amino acid level. Moreover, genetic modifications

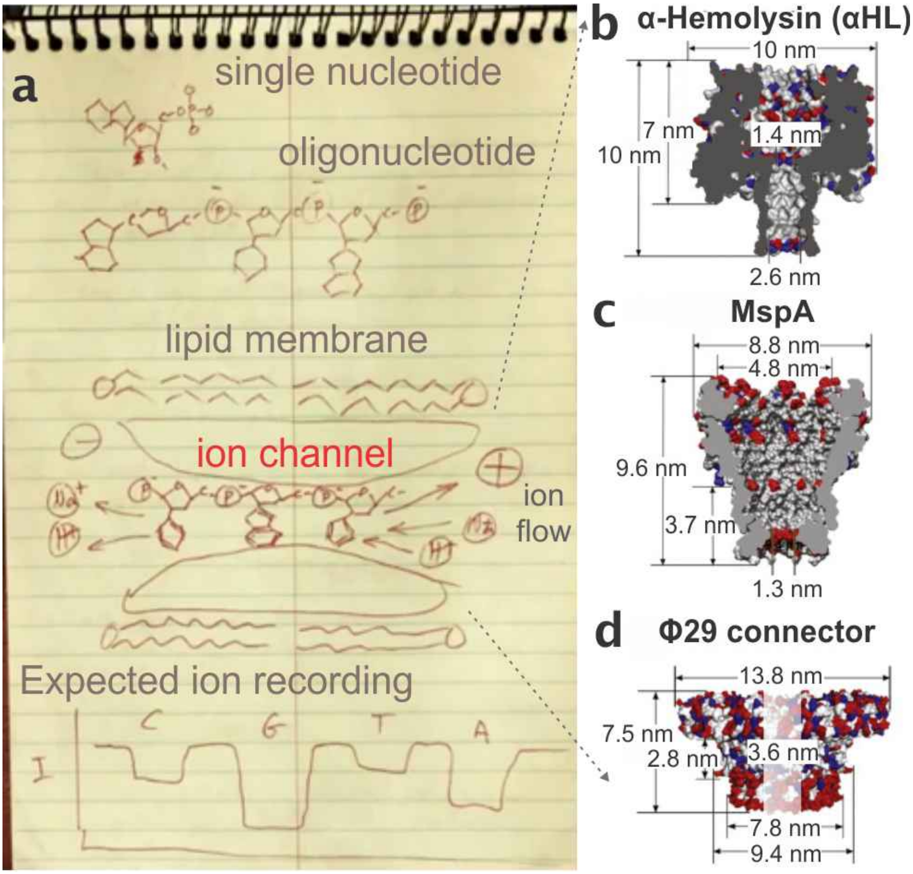

Figure 1.3: Schematics of nanopore sequencing and biological nanopores. (a) David Deamer's sketch on a lab notebook in 1989 for the idea for nanopore sequencing [9]. Single nucleotide and oligonucleotide containing three bases with negative charges are shown on top. This charged oligonucleotide is placed into a narrow channel which is surrounded by bilayer lipid membrane. The positive and negative signs indicate the voltage polarity across the membrane channel. The flows of ion species are marked by the arrows. The expected ionic current of different bases is illustrated at the bottom plot. (b-d) Three commonly-used protein ion-channels as nanopores in panel a [10]. Side and top views of (b) Heptameric α*-hemolysin from Staphylococcus aureus; (c) Octameric MspA from Mycobacterium smegmatis and (d) Dodecameric connector channel from bacteriophage phi29 DNA packaging motor. Acidic, basic, and other amino acids are shown in red, blue and white.*

can facilitate to couple a nanopore with another protein of interest. On the other hand, although some biological nanopores are relatively stable, they need to be incorporated in easily deformed lipid bilayer membranes. Hence, reagents –especially the lipid membrane layers- should be freshly prepared before use. Since the nanopores are floating in the lipid membranes, their precise positions are less controlled and limited by Poisson' statistics.

Solid-state Nanopores

To solve some of the issues related to biological nanopores, many have started to probe into solid-state nanopores. Nanopores fabricated in silicon nitride membranes have been actively explored by far. Different fabrication methods to manufacture nanopores in low-stress silicon nitride membranes have been described, including ion- [13] and electron beam [14] methods. Figure 1.4 shows two examples of nanopores which are created by ion beam and electron beam etching, respectively. In Figure 1.4b, an ion-beam sculpted pore is examined by TEM. The 3D tomogram in panel c shows detailed information on the ion-beam sculpted pore structure. Electron beams require thinner membranes. Figure 1.4d illustrates an ebeam sculpted SiN nanopore. The inset high-resolution TEM is able to clearly identify the boundaries of a pore, while the bottom inset depicts the drilled hour-glass shape nanopores [15].

Besides the widely used SiN, other dielectric materials with different surface charges (Al_2O_3, HfO_2) have been investigated as membrane materials. Lately, more research is also focusing on forming solid state-nanopores in 2D materials, such as graphene. As their thickness is only a single atomic layer, 2D materials may provide ultimate resolution. In addition to the conductive and hydrophobic graphene, insulating boron nitride (BN) and hydrophilic molybdenum disulfide (MoS_2) [16] have been demonstrated for highly sensitive DNA single-molecule detection. Theoretical simulations predict that the different nucleotides could be distinguished in graphene nanopores [17, 18] or MoS_2 nanopores[19]), indicating the potential of this material system. However, the practical realization of single-nucleotide identification on 2D materials still needs further developments.

Solid-state nanopores have emerged as a versatile alternative to biological nanopores owing to their unique properties including well-defined geometries and dimensions, mechanical robustness, ease of modifications, and compatibility with various electronic and/or optical measurement techniques. Another benefit and strategy applied for solid-state nanopores is brought by feasibly adding active and electrical components. For instance, metal electrodes introduced onto the nanopores can be used to examine tunneling currents. These electrodes also

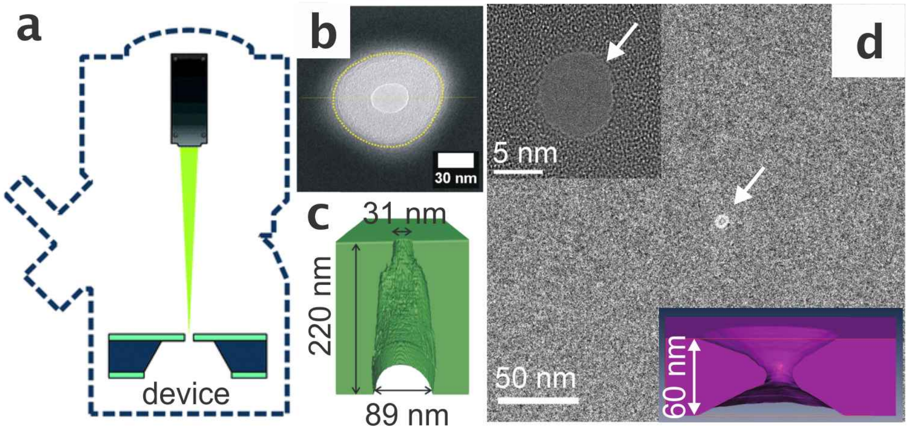

Figure 1.4: Solid-state nanopores. (a) Schematic representation of the nanopore fabrication on a device with a free-standing membrane. Ion beam or electron beam can be focused onto the surface of the membrane. (b) Transmission electron microscopy (TEM) image of an Ion beam sculpted nanopore [20]. (c) 3D tomographic reconstruction of the same pore in panel b. (d) TEM image of a nanopore with the size of 8 nm [15]. The top inset show high-resolution TEM (HR-TEM) image, while the bottom one presents the 3D surface reconstruction image of the e-beam sculpted nanopore. The diameter of the nanopore is 20 nm.

have been introduced to stretch DNA molecules inside the nanopore [21, 22], which is the second promising direction for nanopore devices.

Compared to biological nanopores, solid-state nanopores yields faster translocation events due to large pore size and different inner wall materials. The fast translocation speeds are typically thousands of base pairs per millisecond, which means that one need to differentiate the current level at sub-microseconds. This raises a huge challenge for present electronic instruments to provide high signal-to-noise ratio at picoampere level. Furthermore, unlike identical biological nanopores, the fabrication of solid-state nanopores with precise dimensions remains challenging due to the process variation at the sub-10 nm scale. These limitations may be overcome by a hybrid nanopore with both the advantages of biological nanopores and the advantages of solid-state ones. Hall et al [23] demonstrated the formation of protein pores (α-HL) on artificial pores in solid-state membrane. This hybrid structure remains functional for the translocation of single-stranded DNA.

1.1.3 Nanopore applications

The threading of single-molecules, such as DNA, makes nanopores unique devices for various applications. We can classify the potential applications based on the requirement of spatial and temporal resolution. Taking DNA as an example, the applications range from basic single-molecule DNA detection, DNA mapping to high-resolution DNA sequencing. Moreover, other kinds of biopolymers have been examined by virtue of nanopores as well.

Single-molecule DNA sizing

Considering a long stranded DNA, its length, secondary structures and polymer dynamics may potentially be discriminated using a nanopore. Principally, the dwelling time can yield information about the DNA length, while the time between events can give an idea about the DNA concentration.

Different research groups have characterized the length discrimination using different size of pores. For biological nanopores (for example, alpha-hemolysin), the translocations of RNA of the length up to kilobases have been found to yield a linear increase in duration time t_d with increasing length with a well-defined major population of long events [24, 25, 26]. However, Deamer et al [27] observed the translocation velocity differences between homopolymers with molecular species (poly(A) for $\sim$20 μs/base, poly(U) for 6 μs/ base and poly(C) for 2 μs/ base), which encourage the distinction among different molecular species, but limit size discrimination to some extent.

For the sizing of double-stranded DNA, Wanunu's group used a solid-state nanopore with a diameter-of 2.9 nm and confirmed the existence of a nonlinear dependence on DNA length. In the example of length discrimination in Figure 1.5a,b, the DNA events between 100 and 500 bp can be separated with an accuracy of 98.4% and 97.6%, respectively, when dividing the populations at 450 ms [28]. Besides the length, Fologea et al [29] experimentally demonstrated that linear, circular relaxed, or supercoiled forms of plasmid DNA could be discriminated. Figure 1.5c describes the length scaling of the translocation time for 35 bp to 20 kbp. The fast translocation of DNA follows a power law dependency of $t_d \sim N^{1.37}$ [28]. This can be attributed to additional mechanisms of the interactions of external DNA with the pore material, the interactions of the DNA coil with itself, or a coil-dependent electric-field profile that is affected by co-ion exclusion by the DNA coil [8].

The transport through solid-state nanopores is also largely dependent on the nanopore diameter size. Storm et al [30] used solid-state pores with a diameter of 10 nm and found a nonlinear dependence on DNA length. The duration

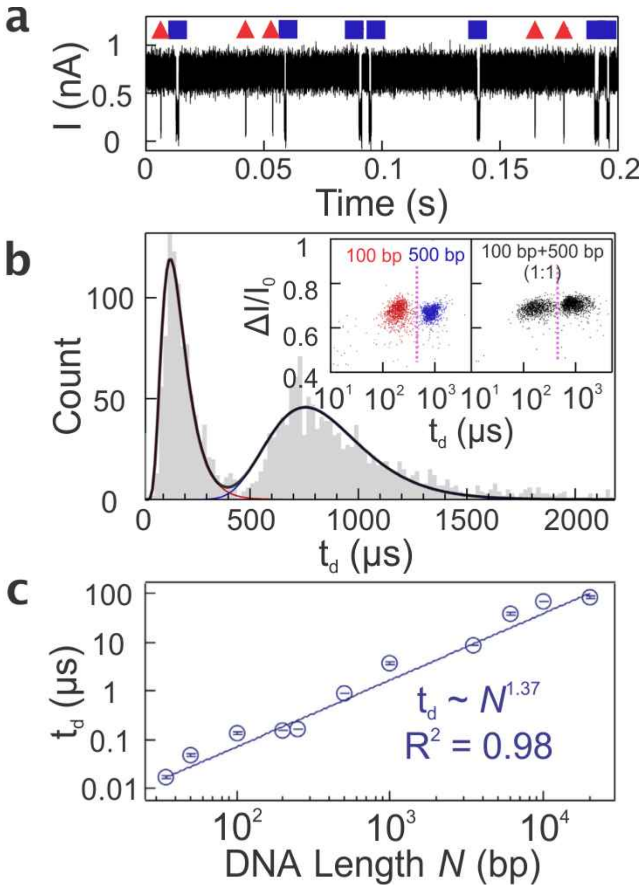

Figure 1.5: Scaling of transport time t_d as a function of DNA length N and DNA length discrimination [28]. (a) Current trace for a equimolar mixture of 100 bp and 500 bp in a small, thin nanopore shows a clear distinction between the two different lengths as denoted by the red triangle and blue squares (100 and 500 bp). (b) Dwell time distributions of translocation data from panel a, showing distinct peaks for 100 and 500 bp. Inset: Scatter plots of the fractional current blockade versus dwell time for the translocation of 100 bp (red, left) and 500 bp (blue, right) separately and together in an equimolar mixture (black) in pores of comparable size (d=2.6 nm). (c) A logarithmic plot of dwell time t_d vs. N for DNA translocation through pores in panel c. By fitting the data using a power-law function ($t_d \sim N^\alpha$) for 35 bp $<$ N $<$ 20,000 bp, a power exponent α=1.37 can be extracted [28].

time scaled as $t_d \sim N^{1.27}$, which was attributed to the hydrodynamics of the shrinking Gaussian DNA coil outside the pore during translocation.

Despite of the simplicity of the idea, the main limitation for nucleic acid sizing is the velocity interfaces from different base species. Moreover, because of the DNA folds, knots and other secondary structures, the broaden distributions increase the complexity of the sizing discrimination. Additionally, biological and especially solid state nanopores are limited by the fast translocation speed of the power scaling law and the irregularity of the individual translocation events. We note that the temporal resolution of short oligonucleotides (less than 20 bp) may confront with barriers.

To increase resolution, enormous efforts have been made to control the speed of DNA translocations in three general regimes: the construction of a nanopore, the properties of the electrolyte solution and the analytes. First, the pore material has been engineered with atomic layer deposition (ALD) [31, 32] or have been covered with self-assembled monolayers [33, 34, 35, 36], yielding 4-10 folds slower translocation speeds compared to conventional SiN pores. Also by control the viscosity [37], pressure [38, 39, 40] , concentration [41, 42] or temperature [43] in the manners of homogenous profile, localized profile or in a gradient profile, the translocation velocity has been decreased with several folds. Finally, especially for biological nanopores, other molecules such as enzymes or histones have been coupled to the nanopore to pull or push DNA through the pores in a more consistent speed. An extreme example is the use of a ϕ29 DNA polymerase to achieve forward and reverse ratcheting of DNA during nanopore tranlocation. This approach yielded 0.5 nm resolution and slowed down translocation to hundreds ms/base [44, 45]. Such regulated translocation is also naturally essential for DNA mapping and sequencing (see below) [46, 47, 48, 49].

DNA mapping using nanopores

DNA mapping is a technique that allows to provide long-distance information along a DNA molecule (typically between 50 kilobases and several megabases) [50]. Figure 1.6a shows the concept of this application. First, molecular markers are labeled at the sequence-specific positions (shown in the top panel). The distance between these elements can be determined by ionic current changes or fluorescent signal. One can employ 1 color to determine the distance between the tags or utilize multiple colors to determine the order of colors. Since the genetic markers are bound to short but highly specific sequences, the physical location of a gene and the relative distance between genes can be reconstructed.

The map of DNA at the bottom panel of Figure 1.6a provides global detection that is not included in the conventional short DNA sequencing.

In many applications, DNA sequence data at the single nucleotide resolution are not always compulsory. For instance, to probe into genomic reorganizations such as insertion/deletions or repeats, or to investigate pathogen similarities in epidemiological studies, a barcode of the genome is often sufficient to provide related information. Additionally, genomic mapping for very long stretches of DNA has proven of vital importance in the field of *de novo* genome sequencing or to span long regions of repetitive elements.

Nanopores are ideal devices to probe DNA maps since the target DNA strand can be linearized and sequentially be threaded through the pore. As the binding of specific molecular markers (e.g. short complementary synthetic DNA oligos) lead to a specific current blockage, the distance between the markers can be determined. The distance discrimination can also be complemented by differentiate double stranded segments from single stranded DNA. In addition, fluorescence labeled markers can be optically captured when passing through the pore, allowing for fluorescent based DNA mapping.

Figure 1.6 illustrates the two methods for DNA mapping using either electrical detection (panel a) or optical detection (panel b). For example, DNA binding protein was used to coat on tagged DNA. Due to the huge volume that the protein could occupy, strong secondary current blockades induced by tagged DNA and binding proteins have been resolved through the electrical readout by Nabsys Inc [53]. The minimum discriminable distance between two binding location can be as short as 1000 bp. Recently, this company claimed that the feasibility of the mapping and genome assembly can be achieved as long as $\sim$150 kbp DNA [53]. However, the twice binding makes the whole process too specific for other markers, which may have limited applications.

Instead of DNA probes and binding proteins,specific sequence of peptide nucleic acid (PNA) has been adopted to reduce the complexity. In the reports from Singer et al [54, 55], they were able to barcode genes with a measured relative spacing as close as 100 bp, which is approximately 34 nm. However, this extreme discrimination was demonstrated with a 3.7 nm pore, which requires the further processing development of high-throughput devices. The highly specificity of PNA as well as the pore requirements, currently limits the commercialization.

An alternative method could be the combination of electrical and optical readout. An example is illustrated in Figure 1.6b. Divergent from measuring the enlarged signals from translocating bound markers on the target DNA, the working principle goes to detect the releasing of bound markers. On the positioned target DNA, fluorophores are designed neighboring the quenchers so that no

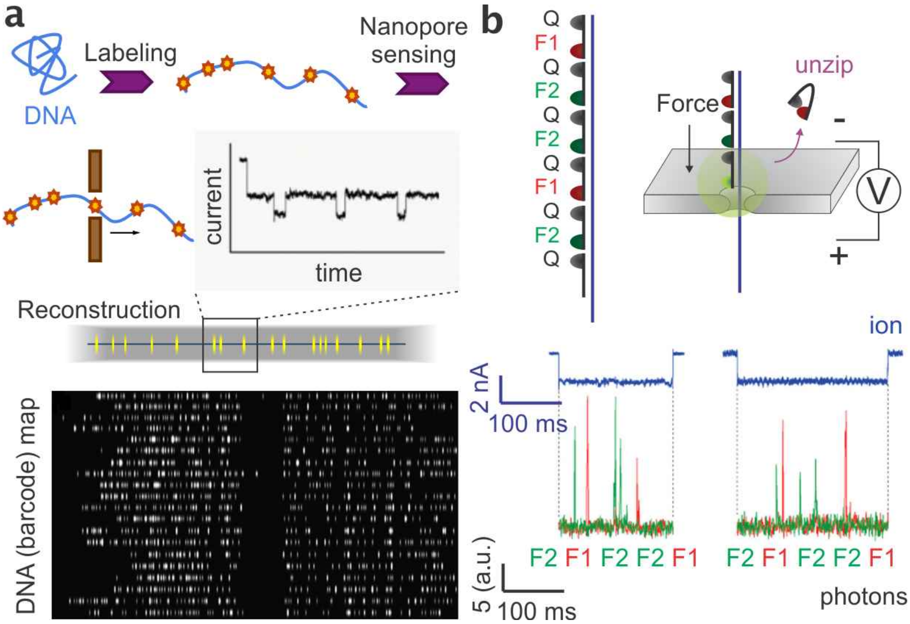

Figure 1.6: Mapping DNA profiles using nanopores. (a) The concept of DNA mapping using ionic detection. DNA strands labeled with short specific sequence can generated a secondary current blockade due to the larger occupied volume. The positional map can be reconstructed and finally contributed to a DNA barcode map [51]. (b) Two-colors fluorophores DNA mapping. Single-stranded DNA is tagged with specific sequences, which are labelled with a fluorophore (F1 or F2) on one side and a quencher (Q) on the other side. Since the fluorophore is located close to the neighbor quencher, the assembled DNA complex is designed as quenched at the resting state. While translocating DNA complex through a low photoluminescence 3 nm pore, the unzipping process occurs and releases a quencher from the DNA complex. The fluorophore nearby thus can contribute a burst of photons. For the simultaneous recording of optical and electrical signals, the examples show five clear photon bursts per event in the green and red channels [52].

fluorescent signal can be generated in the resting state. When dragging the positioned target DNA through a narrow pore, the binding markers along with fluorophore are unzipped from target DNA, resulting in the separation between the fluorophore and the neighboring quencher. As a consequence, one can observe a strong photon burst through a nanopore. The binding markers can be sequentially stripped off, resulting in a series of detectable photon bursts. This technique is possible for simultaneous parallelization to extend to large arrays. However, the translocation speeds of events are still quite fast for optical readout, which require the instruments for optical detection to operate at a high bandwidth.

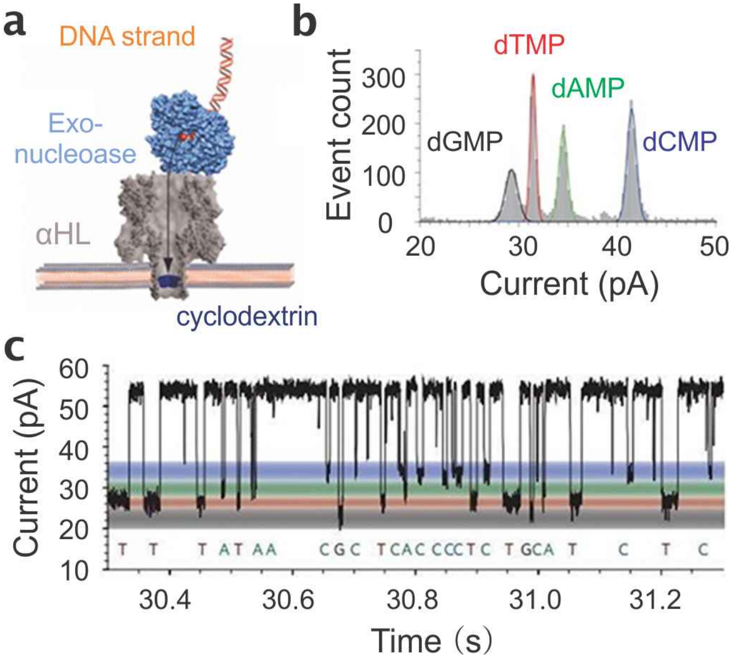

Figure 1.7: Sequencing by digesting [10]. (a) Proposed exonuclease-sequencing with α-HL (porin) and exonucleoase (enzyme). An exonuclease (light blue) attaches to the top of an α-HL pore through a genetically encoded (deep blue), or chemical linker. It ***sequentially cleaves*** *dNMPs (red) off the end of a DNA strand. A dNMPs identity (A, T, G or C) is determined by the level of the current blockade it causes when driven into an aminocyclodextrin adaptor (the narrowst confinement, dark blue) lodged within the pore. (b) Ionic recording of the re-engineered α-hemolysin pore upon addition of mono-nucleotides showing dGMP, dTMP, dAMP and dCMP discrimination; colored bands added to represent the residual current distribution for each nucleotide [56]. (c) Corresponding residual current histogram of nucleotide binding events, including the Gaussian fits [56].*

Nanopore nucleic acid sequencing

DNA sequencing has been considered as the holy grail of nanopore research. Reading single nucleotides during translocation in principle allows for the direct sequence analysis of single, native DNA molecules. Naturally, the required resolution, the control of translocation speed and the necessary signal-to-noise ratio have proven to be challenging. Still, many groups have shown significant steps forward and, recently, even first DNA sequences using nanopores are being reported. Some of the latest explored results and approaches are described below.

Sequencing by digesting. To turn nanopore sequencing into a reality, Bayley's group [56] pursued the idea of using an enzyme that would digest a DNA strand base by base. By translocating the released nucleotides in sequential order through a pore and differentiating the single nucleotides, the original sequence could be determined. This sequencing method, so-called exonuclease sequencing, is depicted in Figure 1.7. Each kind of bases can be clearly identified in Figure 1.7c, based on their specific current drop profiles. Although the differentiation of different nucleotides based on their electrical signal has been demonstrated convincingly, the available data and simulations [58] suggested that the exonuclease-nanopore could be problematic when the read-length goes longer than 80 bases due to the high diffusion property of mononucleotides [58]. In other words, the chance that the cleaved nucleotides do not enter the nanopore or not in the right order makes this approach not applicable in practice. Still, the published research was pioneering to demonstrate the differentiation of single nucleotides using a nanopore.

Sequencing by synthesis. To maintain nucleotides on the strand, an alternative approach was exploited. In this method, a single DNA-strand was pulled through a pore while being copied by a polymerase. Gundlach's group [46] showed that when coupling ϕ29 DNA polymerase with MspA, the current through the pore was co-determined by 4 neighboring nucleotides passing through the nanopore (shown in Figure 1.8). This means that the current values can be revealed when all possible combinations of 4 base-pairs (4^4 combinations) could be differentiated. The current blockades for the 256 combinations have been tested by immobilizing them into a pore one by one beforehand. As such, the sequence of the bacteriophage phi X 174 genome which is 4,500 bases long, could be highly predicted [48, 47]. However, because of its low accuracy and the difficulty to differentiate all the current levels, this approach may have limited influences on sequencing technology, especially for unknown DNA sequences.

Direct sequencing. Commercial nanopores use the same sequencing-by-synthesis strategy, therefore confronting the same issues on the detection and control of DNA molecules. Oxford Nanopore Technologies (ONT), as the pioneer company, distributed MinION^{TM} (shown in Figure 1.9a) to early access sites, using an array of multiplexed protein nanopores [59]. The device in Figure 1.9a scaled down to a USB hand-held portable size. Here, the improved protein pores are announced to be able to achieve 3 base-pairs resolution, which largely

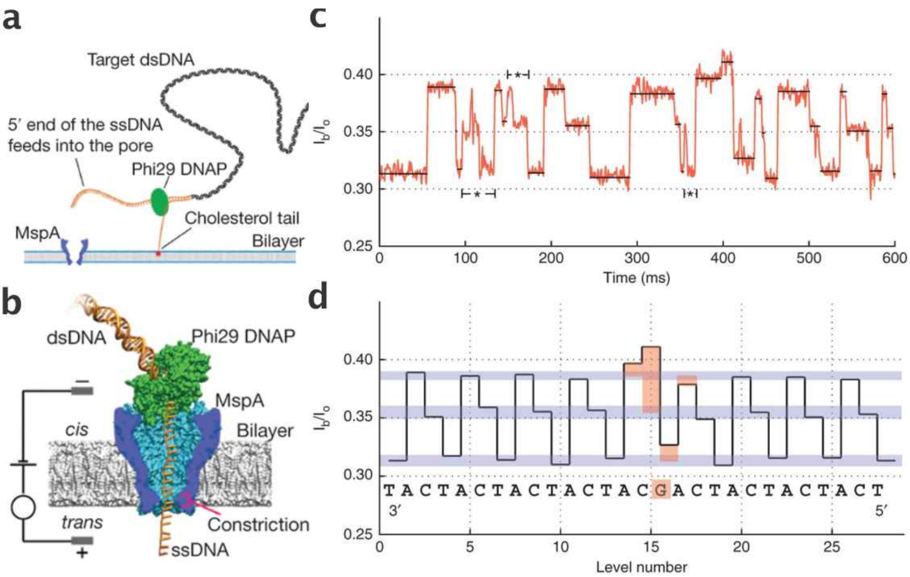

Figure 1.8: Sequencing by synthesis [46, 47]. (a) The first adapter (orange) includes a cholesterol tail that inserts into the membrane, increasing DNA capture rates [57], whereas the long 5' single-stranded overhang facilitates insertion into the pore. A second adaptor (green) enables the rereading of the DNA using the DNAP's synthesis mode. (b) The protein nanopore MspA is shown in blue, ϕ29 DNAP in green and DNA in orange. An applied voltage across the membrane drives an ion current through the pore and an amplifier measures the current. DNA bases within the constriction determine the ion current. ϕ29 DNAP steps DNA through the pore in single-nucleotide steps. Reading a repetitive DNA template. Decoding long reads of natural bacteriophage phi X-174 genome DNA [47]. (c) Example trace for a DNA template composed of repeated "CAT" tri-nucleotides, with the exception of one "CAG" triplet in the middle of the sequence. (d) Mean currents of levels extracted from a with the associated DNA sequence are shown. The current trace exhibits a repeating pattern of three levels (blue bars) interrupted by the single dG substitution (highlighted in orange). Four levels are affected by the single dG with the largest deviations closest to the substitution. This indicates that the residual current is principally influenced by one or two nucleotides with a lesser influence from neighboring nucleotides [46].

decrease the uncertainty of the discrimination. Therefore, these pores could be used for direct sequencing. The device consists of an array of 2048 pores multiplexed into 512 read channels and embedded in a flowcell. It was noted

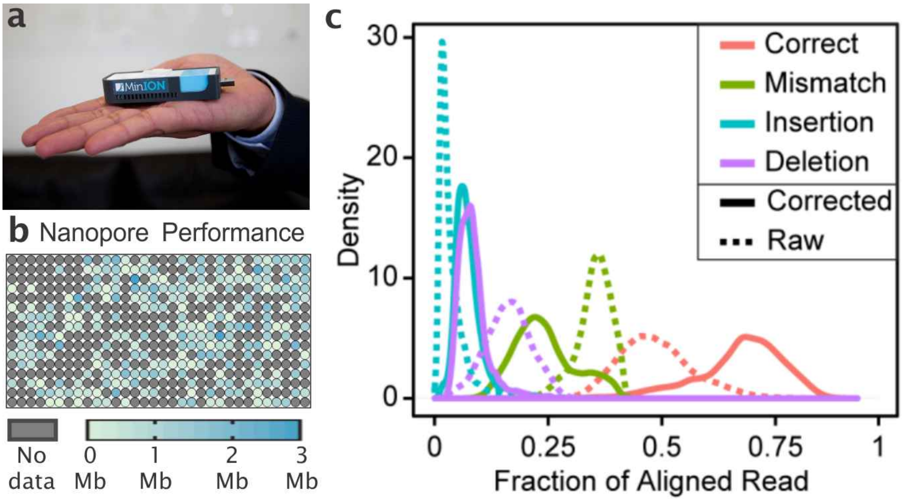

Figure 1.9: Commercial available nanopore sequencer - the MinlON (Oxford Nanopore Sequencing, UK) [59]. (a) A MinION device on hand. (b) Yield plot of DNA sequence produced per channel. Each channel is represented by a circle. Channels in gray produced no data. The average yield from other channels has a mean of 0.9 Mb and a standard deviation of 0.6 Mb with a max yield of 2.9 Mb. (c) Correct, mismatched, inserted or deleted base desnity versus the fraction of aligned reads. Both raw (dotted) and processed (solid) fractions are plotted.

that not all membranes were active (see Figure 1.9b). For the raw data of known lambda reference genome, Timp et al [59] found out that 48.7% of the bases were correct, 35.1% mismatched, 3.8% insertions and 16.2% deletions relative to the length of the aligned read. In contrast, after error correction in Figure 1.9c, the result improves to 67.4% correct, 24.2% mismatched, 7.5% insertions and 8.3% deletions. Insertion could be related to the enzymatic step of specific polymerase, while deletion in particular could be interpreted as DNA slipping through the pore with a high speed. The results in Figure 1.9c provide us the present status that *both base-calling (mismatches) and translocation control are still problematic.*

Despite the enormous progress made for biological nanopores in the field of DNA sequencing, the researches using solid-state nanopores are lagging behind. The main reason is the intrinsic limitations towards accurate control of the pore size, the overall faster translocation speeds, and the overall thickness of the solid state membranes. Still, different approaches have been explored. Using a solid-state pore which geometry is similar to biological nanopores, Venta et al [60] was able to resolve ionic current levels for short (30 base-pair) ssDNA homo-polymers (poly(dA), poly(dC), poly(dT)). The mean current blockade for the homopolymers can be differentiated with the criteria of 200-900 pA, whereas biological pore can provide the criteria of only 5-15 pA (α-HL) [27] or 6-11 pA (MspA) [61]. However, the differentiation on individual bases still needs to be explored with a great concern.

Besides looking at current blockades, alternative readout schemes have been explored as well. For example, DNA bases have been successfully identified using scanning tunneling probes. Statistical identification of the nucleotides have been demonstrated based on their tunneling currents (electrical conductivity) [62] and functionalized recognition of tunneling current signals [63]. The capability to discriminate single nucleotides largely triggered the integration of ***tunneling electrodes*** with a nanopore [64, 65, 62]. Engineered nanogaps between metal electrodes have been scaled down to 2 nm [66]. Still, for tunneling, both the ideal distance and the alignment between gap and pore require the atomic resolution (0.5-0.8 nm).

To circumvent the required resolution, hybrid systems in which a biological pore is inserted onto the solid-state one have been explored as well. Although the protein pores (α-HL and MspA) hold great promises and is about to be commercialized to the sequencing market, topping it on the solid-state pore will decrease the resolution of base-calling due to the high noise level originated from the solid-state substrate.

Other applications using nanopores

Although the up-mentioned DNA related applications are by far governing the field of research for nanopore technologies, other interesting applications have been described. For instance, nanopores have been described to assess protein structural domains, modifications as well as to probe protein-protein interactions [68]. Figure 1.10a illustrates a spontaneous unfolding during a translocation, which can be used to discriminate site-specific phosphorylation states of thioredoxin [68]. Another example is the use of an unfoldase (shown in Figure 1.10b) to ratchet target protein through a pore [69]. This also further needs to be tested for tightly folded proteins.

The conformation and binding functionality of proteins are of particular interests in drug metabolism and medicines. Maglia and his colleagues [70] evolved Cytolysin A (ClyA) from *Salmonella typhi*, which is a larger nanopore with a tunable size among 3.3 nm, 3.7 nm and 4.2 nm. In Figure 1.10c, these three pores showed that subnanometer variations in the diameter of nanopores greatly affect the recognition of analyte proteins. Engineering ClyA pores also allow for folded domains or proteins to enter the pore, which provide more understanding

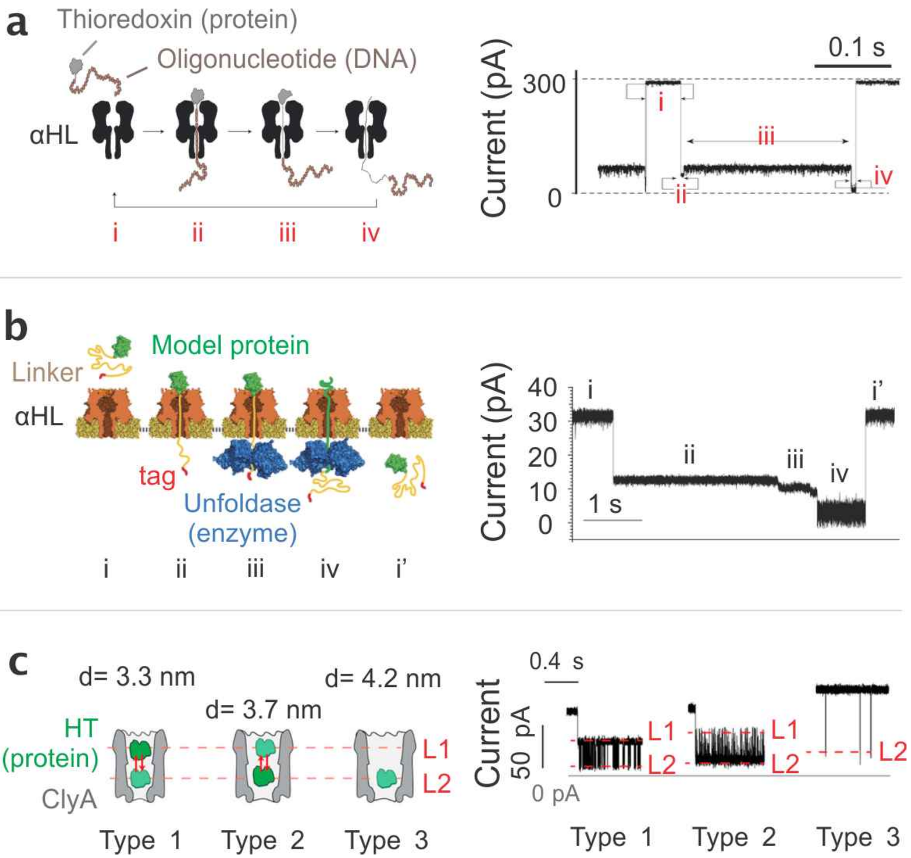

Figure 1.10: Alternative sensing technique using protein nanopores. (a) Co-translocational unfolding of oligonucleotide-linked thioredoxin model protein [67]. Level i: The complex is in solution and the pore is unoccupied. Level ii: the oligonucleotide threads into the pore and pulls on the protein. Level iii: the pulling force causes partial unfolding, allowing the oligonucleotide to traverse the pore and the unfolded segment of the polypeptide to enter. Level iv: the remainder of the polypeptide unfolds, diffuses through the pore and leaves through the trans entrance [67, 68]. (b) Unfoldase-mediated protein translocation [69]. A model protein bearing an green domain at its N terminus is coupled to a charged flexible linker (yellow) with a red tag at its C terminus. In the trans solution, an unfoldase binds the C-terminal sequence. Fueled by ATP hydrolysis, the unfoldase translocates along the protein toward the channel, and catalyzes unfolding and translocation of the green domain through the pore. Level i-v are corresponded to the panels. (c) Size-tunable ClyA nanopores and current blockades provoked by human thrombin (HT) to the different ClyA types [70]. L1 and L2 stand for the two current levels that the protein could occupy.

on the protein interactions with other proteins, drugs or substrates [71, 72]. Moreover, the current blockade and duration time can be used to discriminate conformational heterogeneity in protein-DNA interactions [72]. However, these large protein pores are underestimated and need more investigations to exploit their full potentials.

Solid-state nanopores also allow the transport of proteins, which in principle can have the identical functionality as the protein pores. However, the detection of proteins in their native state remains a major challenge, because most of proteins translocate through the pore too quickly to produce a resolvable signal. Detection of these fast translocations is challenging given the bandwidth limitations of the conventional current instruments [73]. To solve the issue, higher bandwidth amplifiers with low noise [74] have been developed, showing the possibilities to record fast protein events with sub-microsecond temporal resolution. In parallel, the manipulation techniques should be introduced to slow down protein translocations to the resolvable dwelling times. An example is the creation of light modulated electro-osmotic flow moving in opposition to the translocating proteins, which results in an average of $\sim 10\times$ longer dwelling events [75]. Better detection resolution and control methods are still the two key issues to be further investigated to fulfill the requirements.

1.2 Metallic nanopores with surface enhanced Raman spectroscopy (SERS)

Surface enhanced Raman spectroscopy (SERS) holds great promise and allows the observation of subtle spectroscopic phenomena at the single-molecule level. In this section, we start from the explanation of the principle of Raman spectroscopy and SERS. Then, we will introduce different devices and substrates to facilitate SERS. Finally, we will describe the approaches to combine SERS with nanopores for simultaneous detection of single molecules in both optical and electrical methods, which points towards the topic of this thesis.

1.2.1 Raman spectroscopy

Raman spectroscopy is a noninvasive label-free technology which can provide an intrinsic chemical “fingerprint” of a molecule. More specifically, the vibrations of chemical bonds in a molecule are reflected through the inelastic scattering of incident laser light. The working principle of the Raman process is illustrated in Figure 1.11. A scattered photon may maintain its energy, gain energy from or lose energy into molecular vibrations. The process which energy keeps unchanged

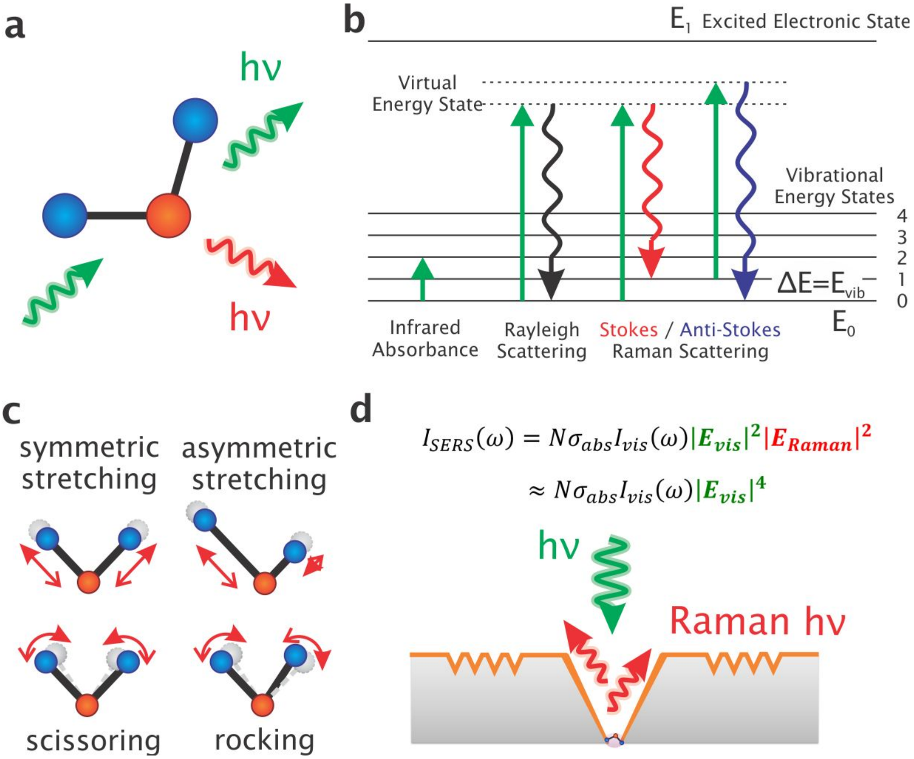

$$I_{SERS}(\omega) = N\sigma_{abs}I_{vis}(\omega)|\boldsymbol{E_{vis}}|^2|\boldsymbol{E_{Raman}}|^2$$
$$\approx N\sigma_{abs}I_{vis}(\omega)|\boldsymbol{E_{vis}}|^4$$

Figure 1.11: (a) Schematic presentation of Raman scattering. (b) Schematics of an infrared absorbance process, a Rayleigh scattering process, a Stokes process and an anti-Stokes process. A vibrational mode of energy E_{vib} generates (Stokes) or loses (anti-Stokes), respectively. (c) Schematic drawing of four typical Raman molecular vibrations. (d) Raman scattering process in a nanocavity device.

(inelastic process) is the Rayleigh scattering, while the energy change causes a frequency shift of the scattered photons. For the latter, the incident light excites the molecule into a “virtual excited state”. When the molecule relaxes, a photon is emitted. The energy of this photon depends on the vibrational state of the molecule. The process that the molecule returns to a higher vibrational energy state than the resting one, is called Stokes Raman scattering, containing lower energy photons. When the molecule settles down at a lower vibrational state than the original one, the higher energy photons are cataloged as Anti-Stokes Raman scattering. The spectrum of Raman scattered photons is composed of the different vibrational levels (e.g. Figure 1.11c). Naturally, the spectrum (as a result of vibrations) is specific for each analyte and, hence, allows for molecule identification.

1.2.2 Plasmonic induced electro-magnetic field enhancement

Normal Raman scattering is a rather weak phenomenon, the signal of which is up to several orders of magnitudes lower than Rayleigh scattering or competing fluorescence. Plasmonics have been shown to extensively enhance the Raman scattering.

The term "Plasmon" is used to describe the *collective oscillations* of *the free electron gas density* – a type of electro-magnetic properties of metals. The rapid oscillations of the electron density in the body of conducting media are *bulk plasmons*, while *surface plasmons* are the electro-magnetic excitations between a metal and a dielectric interface. Figure 1.12 show two types of surface plasmons.

To understand the "Plasmon", we need to characterize the oscillation of free electrons. For bulk plasmon, it can be described by its dispersion relation, which can be derived from classical Maxwell equations as following

$$k_{bulk} = \frac{\omega}{c}\sqrt{\varepsilon_m} = \frac{\omega}{c}\sqrt{1 - \frac{\omega_p^2}{\omega^2}}, \tag{1.1}$$

where k_{bulk} is the wave vector of the bulk plasmon, ω is the angular frequency, c is the speed of light in the vacuum, ε_m is the dielectric constant of the metal. The dielectric constant of the metal can be expressed with the plasmon frequency ω_p which is an intrinsic property of a given metal. Figure 1.12a show this dispersion relation in blue curve. Below the plasmon frequency $\omega < \omega_p$, we cannot obtain a real wave vector. Therefore, there is no propagation of electro-magnetic waves in this region. In most metals, the plasma frequency is in the ultra-violet regime.

For surface plasmons, we can obtain the wave vector at the the metal and the dielectric interface as

$$k_{sp} = \frac{\omega}{c}\sqrt{\frac{\varepsilon_m \varepsilon_d}{\varepsilon_m + \varepsilon_d}}, \tag{1.2}$$

where ω is the angular frequency, c is the speed of light in the vacuum, ε_m is the dielectric constant of the metal and ε_d is the dielectric constant of the dielectric medium. Surface plasmons can thus exist only when a metal ε_m<0 and a dielectric medium ε_d>0 and fulfill ε_m=-ε_d. The dispersion relationship for surface plasmons is shown as the red curve in Figure 1.12a. Resonant surface plasmons (or more exactly surface plasmon polaritons, SPPs) can propagate along the interface between a metal and a dielectric medium.

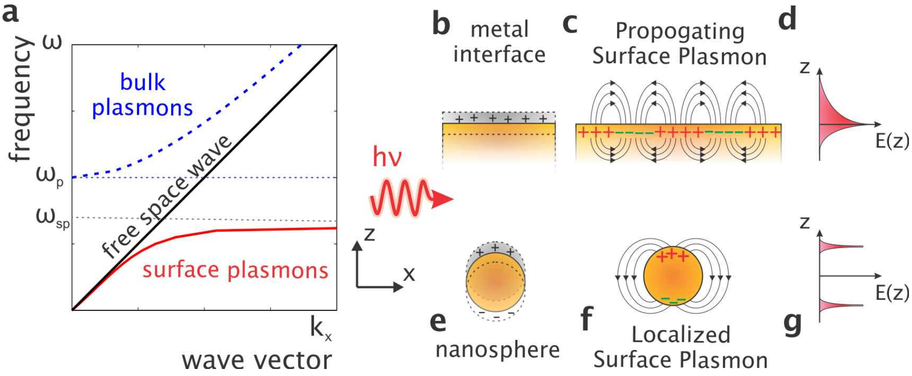

Figure 1.12: Surface plasmon polaritons verses localized surface plasmons. (a) Dispersion relation for bulk plasmons (blue dashed curve), free-space electromagnetic waves (black line), and surface plasmons (red line). (b) Oscillation of the electron gas for a metal-vacuum interface and polarization of plasmons. (c) Schematic representation of a surface wave propagating along x-axis [76]. (d) Schematic representation of the exponential decay along z direction of the electric field of a SPP. (d) Oscillation of the electron gas for a nanosphere. Schematics of the surface charge density of a localized surface plasmons. (e) The surface charge density wave and (f) the electric field of localized surface plasmons are thus elliptically polarized in the plane (x,z). (g) Double peaks along z direction of the electric field of a LSP.

Surface plasmon polaritons (SPPs) vs. Localized surface plasmons (LSPs)

Two distinct types of surface plasmons are known to exist, depending on the geometry of the metal. Surface plasmon polaritons (SPPs, shown in Figure 1.12b-d) sustained at a flat metal–dielectric interface are propagating electromagnetic surface waves associated with a collective oscillation of the free electrons in the metal driven by the electromagnetic field. Figure 1.12d shows efficient coupling to an SPP mode, which enables light at the metal surface to be concentrated into an intense and confined surface wave whose intensity is dramatically larger than the incident intensity.

Unlike SPPs on flat and extended metal interfaces, the localized surface plasmons (LSPs) in Figure 1.12e are associated with bound electron plasmas in metallic nanostructures with dimensions much smaller than the wavelength of the incident light. The spectral position of this resonance is governed by the particle's size and shape, as well as by the dielectric functions of both the metal and the surrounding media. LSPs can be directly coupled with propagating light and confine light into strong electro-magnetic field enhancement at the interfaces (shown in Figure 1.12e).

Both SPPs and LSPs can confine light to the nanometer scale and induce strong electromagnetic field at the interfaces, which facilitate the enhancement of SERS process at the metal interfaces.

1.2.3 Surface Enhanced Raman Spectroscopy (SERS)

Surface enhanced Raman spectroscopy is a specific manifestation of enhanced Raman scattering of molecules at metal surfaces. Signal enhancements reach up to several orders of magnitude, enabling Raman spectroscopy of single molecules. In principle, the Raman scattering of the cross-section of a molecule is too small to be easily detected. For example, the cross-section of single organic molecules are around 10^{-30} to 10^{-28} cm^2 [77], more than 10^{10} smaller than that of fluorescence. High sensitivity detection with strong enhancement is of importance for collecting sufficient Raman photons from small amount of molecules. The SERS signal is enhanced dramatically due to the introduction of a (resonant) metal surface. Therefore, researchers focus on the mechanism how the SERS signal gets enhanced and how to design and engineer metal structures as SERS substrates with strong enhancement.

It is still a matter of debate in the literature on the exact enhancement mechanism observed for SERS. One of the probable mechanisms is believed to be a result of charge-transfer complexes (CT effects). The chemical interaction between the analytes and the metal substrate usually provides an enhancement factor of $\sim 10^2$ [78]. The main mechanism involves an enhancement of the local electromagnetic field due to excitation of surface plasmon (EM effect). The signal enhancement of $10^5 \sim 10^{10}$ can be attributed to the electro-magnetic interaction of light with the metal-dielectric interfaces. The EM enhanced Raman intensity depends on the number of analyte molecules in the enhanced EM field volume (SERS hot spot), the effective Raman cross-section of the molecule and the enhancement of both incident and scattered photons. The SERS intensity $I_{SERS}(\omega)$ can be described as

$$I_{SERS}(\omega) = N\sigma_{abs}I_{vis}(\omega)|E_{vis}|^2|E_{Raman}|^2 \tag{1.3}$$

where N is the amount of analytes, σ_{abs} is the Raman cross-section of specific molecule, $I_{vis}(\omega)$ is the photon intensity of incident light at the frequency ω, and E_{vis} and E_{Raman} are the electric field enhancement of incident frequency and Raman scattering frequency. The equation can be simplified when the Raman frequency shift are much smaller than the incident frequency, described as the following equation,

$$I_{SERS}(\omega) \approx N\sigma_{abs}I_{vis}(\omega)|E_{vis}|^4. \tag{1.4}$$

The SERS intensity therefore is proportional to the 4^{th} power of the electric field enhancement, which can be strongly enhanced due to the excitation of surface plasmon.

1.2.4 Metallic substrates for SERS applications

SERS was first observed on an electrochemical roughened silver substrate by Fleischmann et al in 1973 [79]. Various nanoparticle aggregates or designed nanostructures show the feasibilities for SERS measurements. Some of the enhancement factor can be as high as 10^{10} to 10^{11}, which means the SERS technique may potentially detect individual molecules. However, the enhancement on such SERS substrates is generated by random aggregates of metallic nanoparticles with very small gaps which are not controllable and, hence unreproducible.

To manage the enhancement, researchers engineered various SERS substrates. Figure 1.13c-e shows three examples of SERS substrates, including arrays of nanopillars, nanocavities and nanoholes. The first example is the gold capped silicon nanopillar array in Figure 1.13c, forming a gap-rich plasmonic nanostructure and providing a three-dimensional environment for molecular access. These sub-10 nm gaps and ultra-high density array can be fabricated on a 300 mm wafer level. Figure 1.13d illustrates the commercially available SERS substrate, Klarite^{TM} consisting of gold layer coated arrays of inverted pyramids etched in silicon. These gold micro pyramid pits with a lattice pitch of 2.5 μm focus light into the cavities. The structures were shown to yield reproducibe data with a relative standard deviation of less than 10%. The third case is the nanohole array shown in Figure 1.13e. Besides measuring normal Raman scattering, these nanoholes support the measurement of transmitted Raman spectroscopy, which could be very useful for some application when transmission is preferred.

To propose a process-feasible and highly SERS–enhanced nanopore, we have chosen nanocavities rather than nanoholes due to the controllable formation of hot spots of the former one. Figure 1.11d illustrates the Raman process of a molecule inside a gold nanocavity. A prior study in our group [84] has demonstrated that a width-of-10 nm and length-of-90 nm nanocavity can act as an extremely small but super-strong SERS hot spots with the enhancement factor of $\sim 10^8$ and the spatial resolution of 1-2 nm [84]. Benefiting from the understanding of the EM effect, the designed SERS substrate can highly increase the enhancement factor, enabling single-molecule SERS detection [85].

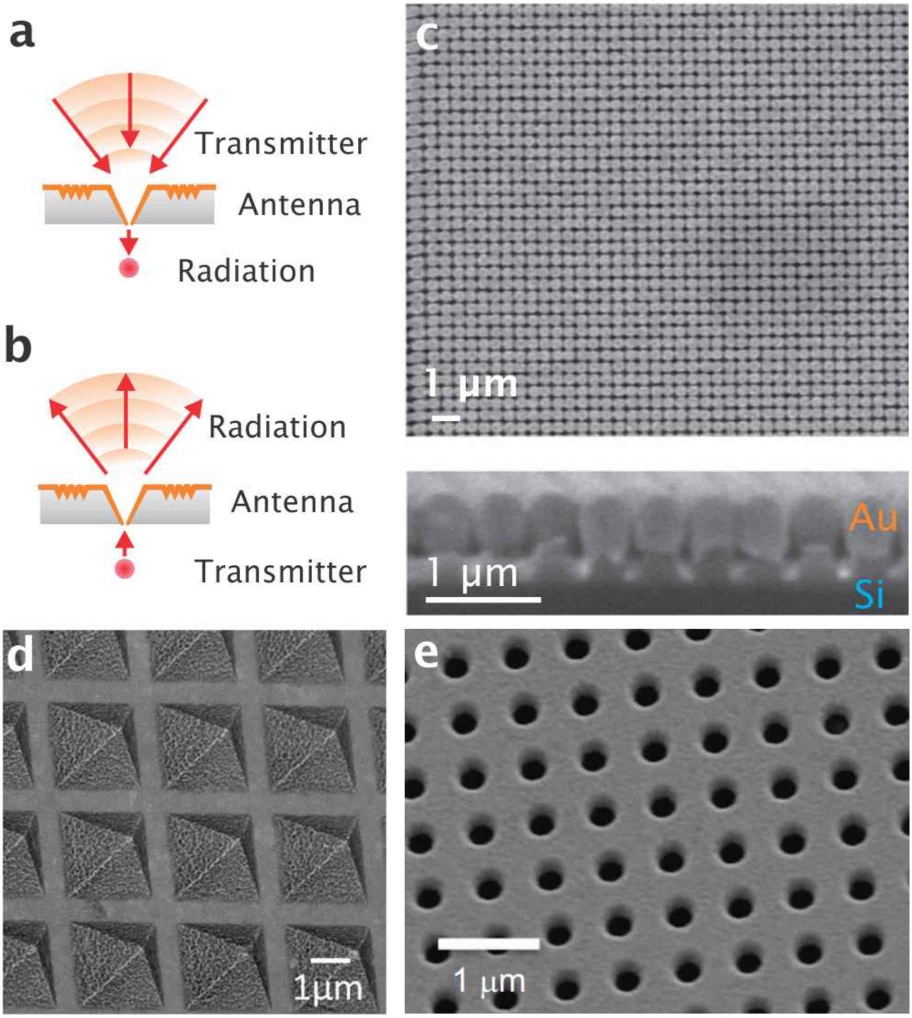

Figure 1.13: SERS substrates. Nanoantenna is illustrated in (a) Transmitting antenna and (b) Receiving antenna in a nanocavity [80]. Arrows indicate the direction of energy flow. The two configurations are related by the principle of reciprocity. In spectroscopy and microscopy, the two antenna concepts are combined; that is, the antenna is used both as a receiver and as a transmitter. (c)-(e) Examples of SERS substrates. (c) 300 mm Wafer-level, ultra-dense arrays of Au-capped nanopillars [81]. (d) The pyramidal pits of Klarite [82]. (e) The periodic nanohole arrays [83]. The bar in each panel stands for 1 μm.

1.2.5 Combination of SERS with nanopores

Integrating SERS substrates with fluidic designs can have several advantages. First, rather than measuring the molecules delivered by diffusion, a flow through nanostructures can efficiently direct the transport of analytes to the SERS hot spot(s) as shown in Figure 1.14a,b [86]. Second, applying a trans-membrane voltage can facilitate the transport of charged particles through the nanopores. Figure 1.14d gives an example of dynamic enhancement of SERS by manipulating the flow containing gold nanoparticles [87]. When no bias is applied(shown in blue), no translocation events occur. An increase in translocation events can be observed when the bias is increased from 500 mV to 750 mV. The result of increased the electric field is responsible for driving the nanoparticles through the nanopore. However, these two fluidic SERS substrates in Figure 1.14a,c were either weakly enhanced or randomly enhanced with aggregates which was not always reliable.

In our group, we have previously optimized gold nanocavity pores (shown in Figure 1.14e), which is also feasible for fluidic integration. First, this nanocavity pore has been designed and optimized to generate a strongly enhanced field A typical 10×90 nm^2 nanocavity pore acts as a super strong hot spot with a SERS enhancement factor of $\sim 10^8$ and a high spatial resolution of sub-2 nm in our simulation. Second, SERS performances have been characterized based on such nanocavity pores. The width-of-6 nm nanocavities exhibit 10^6 SERS enhancement factor based on a self-assembly monolayer of 4-aminothiophenol on the pore surface [89]. By precisely positioning carbonaceous nanoparticles of 20 nm at different locations in the nanocavity, further evidence for the high confinement of the SERS hot-spots has been demonstrated [90].

The combination of nanopores, for mechanical confinement, together with SERS, for optical interrogation, could provide new possibilities for single molecule detections and manipulations. Figure 1.15 shows our strategy for nanopore fluidics SERS and the electro-magnetic field enhancement inside the nanopore. Compared to the conventional nanopore sequencing method based on ionic current nanofluidics, we are combining surface enhanced Raman spectroscopy (SERS) with solid-state nanopores for real-time DNA detection or even sequencing (as a long-term goal). More specifically, recent advances in nano-optics will be utilized to strongly focus light into a nanometer-dimension spot with very high intensity where the ions flow through. Locally confined electro-magnetic fields accentuate the capabilities to generate an attractive force to small particles that become “trapped” in the beam of light. The use of near-field optical tweezers could manipulate DNA molecules being translocated in a controlled way. Moreover, the intense optical fields of the hot spots could enhance Raman scattering with many orders of magnitude, allowing the

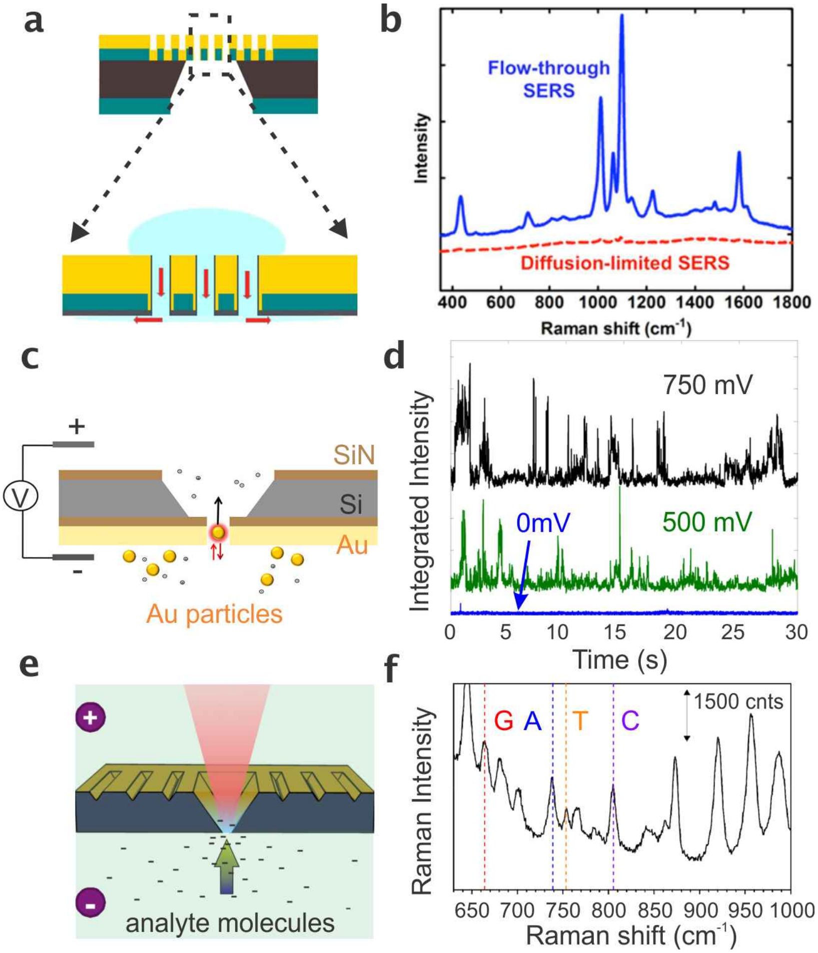

Figure 1.14: Combination of fluidics with SERS. (a) Flow faciliated SERS measurement of a suspended nanohole array chip. Hydrophilic sidewalls drive the flow toward the back of the chip (shown as red arrows) [86]. (b) Comparison of SERS spectra obtained from flow-through of 100 nM 4-mercaptopyridine (red) and diffusive transport (blue). (c) Gold nanoparticle enhanced SERS when a positive bias was applied to drive the nanoparticle through the pore. (d) Effect of applied bias on the nanoparticle translocations using the 1174 cm^{-1} *vibrational band. The blue, green and black curves represent the case with no bias, +500 mV and +750 mV [87]. (e) A gold nanocavity pore for SERS detection of nucleotides. A positive bias was applied to the side with gold nanocavity. (f) An example of SERS spectrum of 50 base pair DNA oligonucleotides [88]. The dominant peak positions for the four bases (G, A, T, C) were illustrated in dashed lines.*

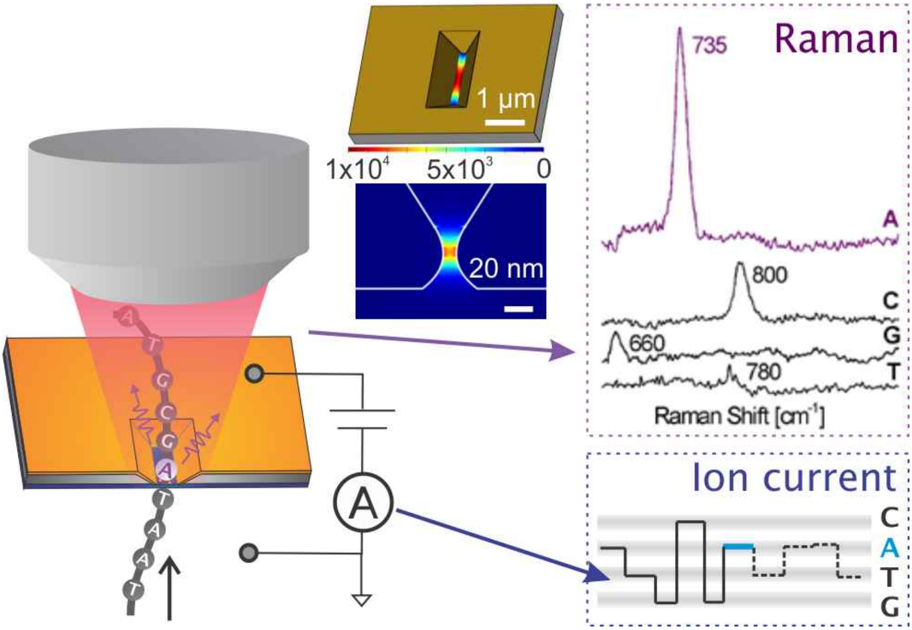

Figure 1.15: Schematic drawing of nanopore SERS sequencing approach. Upon resonnant plasmonic excitation by laser illumination, the gold nanopores hold great promise for the strong and highly localized electro-magnetic field enhancement. Insets show the top view and cross-section of the EM field enhancement of the gold nanopore device, which facilitates surface enhanced Raman spectroscopy (SERS) of DNA bases. The sequencing approach using this device is to simutaneously readout the electrical current levels and SERS spectra of the DNA bases in the sequential analysis.

detection of Raman spectra of DNA bases that are directly exposed to the SERS hot spot. Because of the direct relationship between the Raman spectra and the underlying molecular structures, our novel approach will enable us to read the sequence of DNA in a mediate speed without any labeling.

1.3 Challenges (Motivation)

Our nanopore SERS approach combines the advantages of SERS hot spot(s) inside the nanopore with molecular manipulation for the diffused analytes. However, it also exhibits some issues, these of which are amplified and may become challenges upon laser irradiation. According to the introduction of metallic structures, the challenges mainly originate from the intrinsic properties of metal itself and the induced effects upon the excitation of surface plasmons.

Metal induced ionic performance degradation

Along with the expansion of Coulter Counter to new possibilities, to achieve better temporal resolution, solid-state nanopores require large bandwidth, low-noise and high amplification of the measurements. The bandwidth in the nanopore sensing system is similar to voltage clamp electrophysiology recordings. Both of the above-mentioned systems generate weak ionic currents, and their useful signal bandwidths are generally constrained not by small-signal frequency response but by the signal-to-noise ratio (SNR) [74]. The noise characteristics are investigated as the sum of flicker noise at low frequency regime ($<$50 Hz), thermal noise and other sources of white noise at moderate frequency regime and the noise generated by energy dissipation in non-ideal dielectric materials along with the interaction of the amplifier's voltage noise with the total capacitance at the input at frequencies $>$1 kHz, which is the region of interest to observe translocation of DNA through nanopores.

The introduction of metal give rise to excess charges, high parallel capacitance and interfacial capacitance for the region of interest. Despite of the fixed surface charges on any dielectric material, the surface charges on metal can easily be regulated by the applied voltage or induced by a strong electric field (in the manner of floating electrode). Compared to the conventional nanopores, the nanopore constructed with metal may lead to a higher charge fluctuation, which could be related to the flicker noise.

We first build up an approach to investigate the ionic performance of metallic nanocavities. Based on the study of our devices, we characterize with different material stacks to fine tune the properties. This work is discussed in Chapter 3.

We further propose a novel type of device, comprising a conventional membrane layer beneath the gold nanocavity. Sculpturing nanosized pores with electron beam, we fabricate and benchmark the ionic performance of such devices. This work is discussed in Chapter 5.

In short conclusion of this section, the main challenge of this dissertation originates from the combination with the two emerging fields which are relative opposite: one requires high quality of dielectric materials and the other – plasmonics – needs as many coherent oscillations of free electrons as possible. We need to provide more understandings on how to better control of the dielectric layer and improve the optical performances.

Better mechanical confinement inside plasmonic nanocavities

Plasmonic cavities, owning a rectangular shape at the tip, usually have one dimension much larger than individual DNA molecules, allowing the motion of DNA in a folded (non-linear) fashion. Besides, large open area can lead to low signal-to-noise ratio on DNA events. In order to examine single DNA molecules simultaneously by ionic recording and SERS reading, we prefer to have a plasmonic nanostructure which can create an extremely huge electromagnetic field enhancement and can own a tiny ($d<10$ nm) confinement to mechanically regulate the linearization of DNA motion.

We propose to fill the plasmonic nanocavities with a dielectric layer (e.g. SiO_2, Si_3N_4 and etc) and selectively drill through the dielectric membrane using an electron beam. The solid-state nanopore should be precisely aligned to the above hot spot(s) of the plasmonic nanocavity. The fabrication, ionic characterization and DNA translocation experiments are discussed in Chapter 5 and 6.

Plasmonic induced effects

The hybrid nature of surface plasmon (SP) modes – propagating surface plasmon polaritons (SPPs) and localized surface plasmons (LSPs) – as collective photon-electron oscillations, is able to induce various physicochemical processes and energy transfer. A high density of optical states in the vicinity of plasmonic structures enhances light adsorption and emission, enables the localized heating and drives near-field heat exchange between hot and cold surfaces. SP modes can induce the energy of absorbed photon directly to the free electrons, and the generated hot electrons can be utilized in thermoelectric, photovoltaic and photo-catalytic platforms.

Optically excited surface plasmons on novel metal nanocavity pores not only can support SERS enhancement and localized trapping, but also give rise to the generation of local heating and hot electrons which may play a critical role in the interaction with the surrounding environment [91, 92, 93] (see Figure 1.16a). The above-mentioned processes may interfere into the ionic sensing system.

On one hand, metal nanostructures can efficiently generate heat in the presence of electromagnetic radiation. This process becomes strongly enhanced under plasmon resonance. We specifically shown the configuration of the heat transport system in Figure 1.16b. The illuminated part of the gold nanocavity structure can be treated as the heat source. The dimension of the entire environment needs to be much larger than that of the heat source, which can be assumed as a point

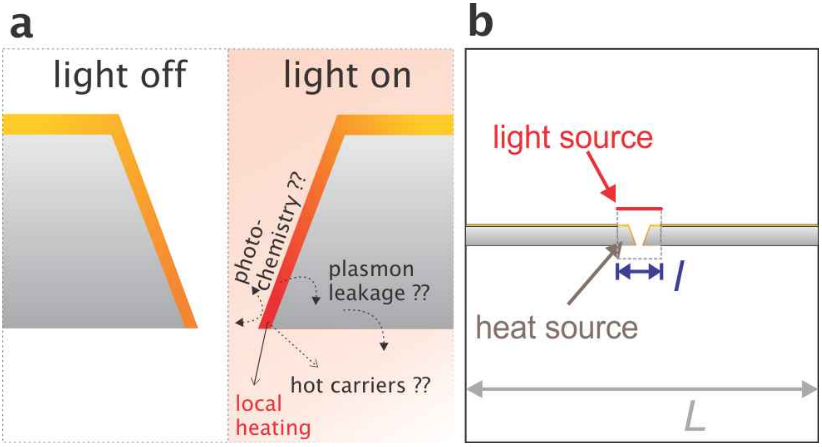

Figure 1.16: Known unknowns of plasmonic induced processes. (a) Schematic of various interacting processes that play a role in a plasmonic nanocavity and potentially interact with the ionic transport. (b) Illustration of plasmonic induced heating source. The red line presents the illuminated light source. The device in blue region which is cover by the light source is used to calculate the dissipated heat as the heat source. The dimension of the heat source l needs to be much smaller than that of the entire environment L so that we can assumed it as a point source.

source. Plasmonic induced Joule heating can increase the bulk conductivity of a given salt concentration, which may further lead to the elevation of ion current.

On the other hand, hot electrons non-radiatively decayed from surface plasmons can induce chemical reactions or the change of surface charges, which may also contribute to the current-voltage measurements or noise spectra. These effects probed by ionic recording as well as by translocating DNA through the nanopores are worth to be evaluated and well interpreted.

By characterizing of the ionic noise properties on plasmonic nanocavity pores upon laser irradiation, we propose two approaches to reduce the increased ionic noise. Both of the methods are discussed in Chapter 4.

We also investigate the ionic current profiles of nanopore-in-cavity device upon plasmonic excitation. The current deviations upon different laser powers provide us a new concept of the fluidic transport at the nanoscale. This photoresistance switching phenomena and the properties are discussed in Chapter 6.

1.4 Objectives

This research aims at these following objectives:

- **To develop a fabrication procedure for massively scaling up the production of metallic nanopores.** The metallic nanopore devices need to fulfill both optical and fluidic requirements. The first milestone of this thesis is to practically produce metallic nanocavity pores with the width of sub-20 nm. We have to restrict ourselves to such a small scale because DNA can only be detectable and provide high SNR at small pores. Fabricating various nanostructures is usually straightforward, while developing working nanodevices is not easy. The fabricated devices need to support the excitation of surface plasmons and allow the regular transport of ions simultaneously. These requirements highly motivate the fabrication of the metallic nanopores, and drive us to the second objective.
- **To build up an effective evaluating system on the ionic performance of metallic nanopores.** The contents of the ionic characterization system comprise three aspects: a) To correctly probe the device performance, one needs to have a reliable setup and appropriate protocols. b) To benchmark the device performance, the measured results should be comparable either to the state-of-the-art characteristics or different types of devices. c) To comprehensively interpret the characterizations, theoretical calculations or numerical simulations should contribute to the understanding of the metallic nanopores.
- **To launch the investigation of ionic effects upon surface plasmon excitation.** The transport of ions and biopolymers through a nanopore is the key element of the nanopore research and the bottleneck of the electric detection and manipulation. Without the introduction of plasmonics, ionic transport through conventional pores is likely independent of the optical illumination. However, plasmonics may play an important role to link the ions with photons and give rise to the dependence of the ionic transport on the power of incident light. We would like to understand plasmonic induced ionic effects and further take advantage of them, which potentially facilitate the detection and/or control performances in our long-term plan.

1.5 Contents of this work

The concept of this PhD is the accomplishment of a comprehensive study of the fundamental physicochemical properties of the transport of ions and molecules, by virtue of the combination of the two rapidly emerging fields (plasmonics and nanopores). More specifically, recent advances in nanoplasmonics such as localized heating, localized chemical reaction and localized spectroscopy will be investigated within nanopores.

The readers who are interested in optical design and optimization of the gold nanocavity pores are referred to the PhD thesis of Dr. Chang Chen, whose doctoral research was carried out at imec as well. His dissertation was focused on the development of nanopore SERS by optimizing the properties of surface plasmons in the gold nanocavities. In this PhD thesis, we solely concentrate on the ionic investigation of novel synthetic metallic nanocavity pores.

This thesis is organized as follows:

Chapter 2 introduces the fabrication processes, electrical characterization of nanopores and the basic physicochemical basis of nanopore fluidics and plasmonic induced effects. The numerical simulation approach, used in this thesis are discussed in details.

Chapter 3 describes the ionic characterization of gold nanocavities without laser illumination. We build up the characterization of the ionic performance, mainly focused on current-voltage linearity, device conductivity, noise spectrum and DNA translocation events. Taking metallic nanocavities as an instance, we evaluate their ionic performance and compare them with conventional dielectric nanopores.

Chapter 4 depicts the ionic characterization of plasmonic induced effects on gold nanocavities. We concentrate on the noise properties upon laser illumination and the local potential inside gold nanocavities probing by SERS with laser excitation.

Chapter 5 presents the simulation, fabrication and characterization of a solid-state nanopore inside a plasmonic nanocavity device (nanopore-in-cavity). Current-voltage linearity, device conductivity, noise spectrum and DNA translocation events are comprehensively discussed.

Chapter 6 elaborates the ionic characterization of plasmonic induced effects on the nanopore-in-cavity devices. Current deviation, noise performance and DNA transport are separately studied in each section of this chapter. Particularly, the photoresistance switching phenomena are highlighted.

Chapter 7 contains the conclusion and the perspective of this thesis. It summarizes the development of the plasmonic nanopores and plasmon-induced effects on the ionic and fluidic transport. The challenges and possibilities of detecting single-molecule using plasmonic nanopores are also discussed.

Chapter 2

Research Methodology

In this chapter, we describe different experimental and numerical methodologies that we develop and use in this PhD thesis.

First, we briefly overview how we practically fabricate the nanocavity pore devices in imec. The nanofabrication of nanosized open cavity/pore is challenging. It involves several optical and electron-beam (e-beam) lithography steps, through-wafer wet and/or dry etching processes, double-sided processing and the depositions of both plasmonic materials and nanopore membrane materials. The details of these fabrications will be described in section 2.1, as well as wafer-scale processing we use in 200 mm CMOS fab environment for mass production.

Then we outline how we can take use of the nanocavity/pore devices in an optical fluidic configuration in section 2.2. Since the nanocavity/pore devices are expected to deal with water-based liquids, we will first introduce the flowcell designs and the measurement setup. Second, we will present the state-of-the-art nanopore ionic performances so that we can benchmark our devices with the state-of-the-art reference.

In section 2.3, we describe the theories behind the electric characterizations as well as numerical simulations that can provide us better understanding of plasmonic nanopore devices. First, we will go through the principles of conventional nanopore fluidics and the feasibility of our model to study nanofluidic phenomena. Then we turn to the contents of the excitation of surface plasmons, including the electro-magnetic field enhancement and the resistive heating upon the resonant light illumination. Finally, we illustrate the modified model for nanopore fluidics, which may contribute to a thorough insight of the local heating inside the plasmonic nanopores.

2.1 Nanocavity Fabrication

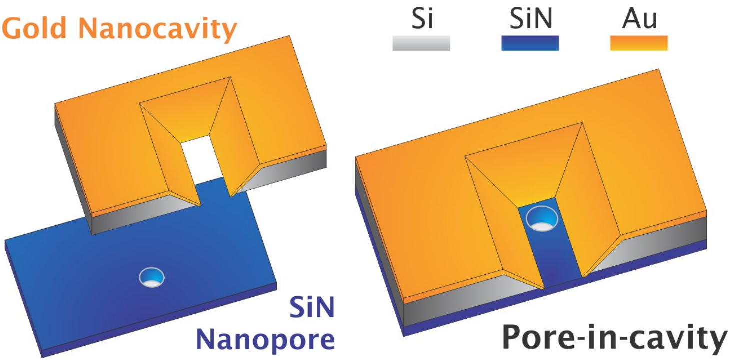

Figure 2.1: Schematic representations of (left) an individual gold nanocavity and an individual state-of-the-art SiN nanopore and (right) an ideal metallic device consisting of a gold cavity on top of a solid-state nanopore.

An ideal device consisting of a gold nanocavity on top of a conventional nanopore is presented in Figure 2.1. To achieve such kind of devices, we developed two different process flows: one in the lab, based on electron-beam lithography and the other in the pilot line, based on DUV lithography.

2.1.1 E-beam based processing

The protocol used in the lab is the continuation of the processing initially developed by R. Kox and C. Chen in their PhD thesis [94, 84] at imec. The general processes are summarized in Figure 2.2. Briefly, we fabricate the critical nanocavity structure and the through-wafer macrostructure, and then remove the passivation layer in between the two silicon layers. The details and critical steps are given as following.

Step 1: We started with a silicon-on-insulator (SOI) wafer, consisting of a 700 μm thick crystalline silicon substrate, a 1 μm buried oxide (BOX) and a 700 nm thin crystalline silicon top layer. The BOX layer acts as the stopping layer for the two anisotropic wet etches.

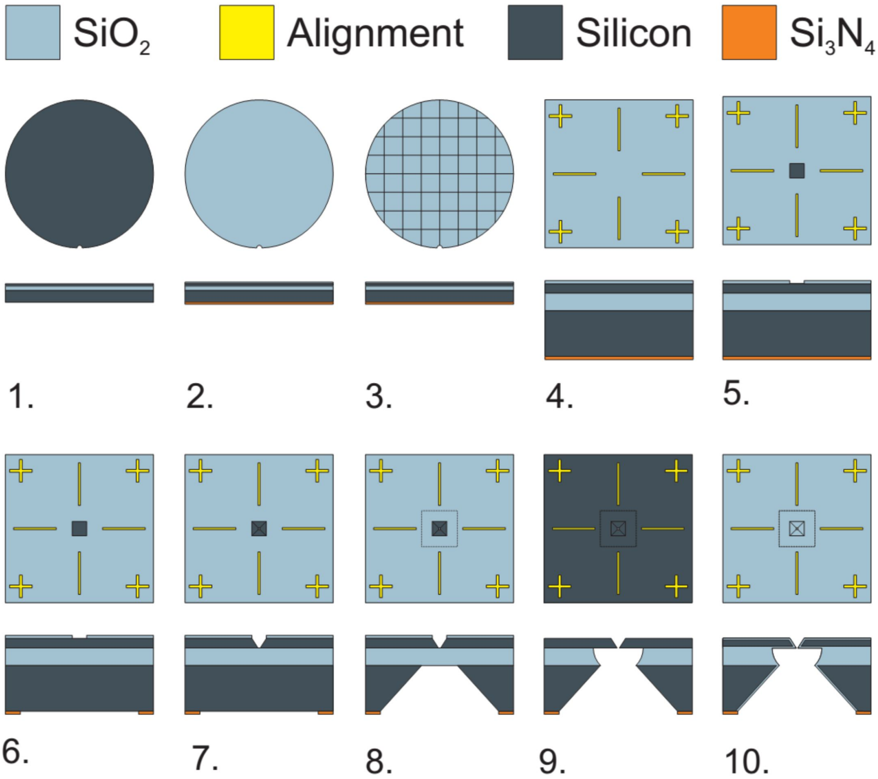

Figure 2.2: E-beam based processes in III/V cleanroom [94]. (1) Initial SOI wafer. (2) SiO_2/Si_3N_4 deposition as hard mask layers. (3) Wafer dicing. (4) Chip alignment, where the markers are transferred into the hard mask. (5) E-beam patterned active nanocavity. (6) Backside alignment and hard mask transfer. (7) Frontside nanocavity anisotropic etching. (8) Backside through-wafer etching. (9) Oxide (BOX) layer remove. (10) Optional thermal oxidation of the device.

Step 2: To avoid extra damage on both sides of the wafer and allow photoresist pattern transferable to a hard mask, 30 nm PECVD SiO_2 and 150 nm LPCVD Si_3N_4 were deposited on the frontside and backside as the masking layers.

Step 3: For the ease of the exposure and further fabrications in the lab, the wafer was diced into pieces of 18×18 mm^2 .

Step 4: To ensure the definition of the size and location of single nanocavity onto each die, positive photoresist AZ6612 was carefully used to pattern alignment markers on each die so that these markers could be well aligned to the edge of each die and thus to the crystal plane. The alignment is critical because we will further perform anisotropic KOH etch in the step 7, the process of which highly relies on the alignment between the pattern and the crystal plane. Any misalignment between them will lead to the rearrangement of the pattern to the crystal plane and therefore obtain an increasing pattern area [94].

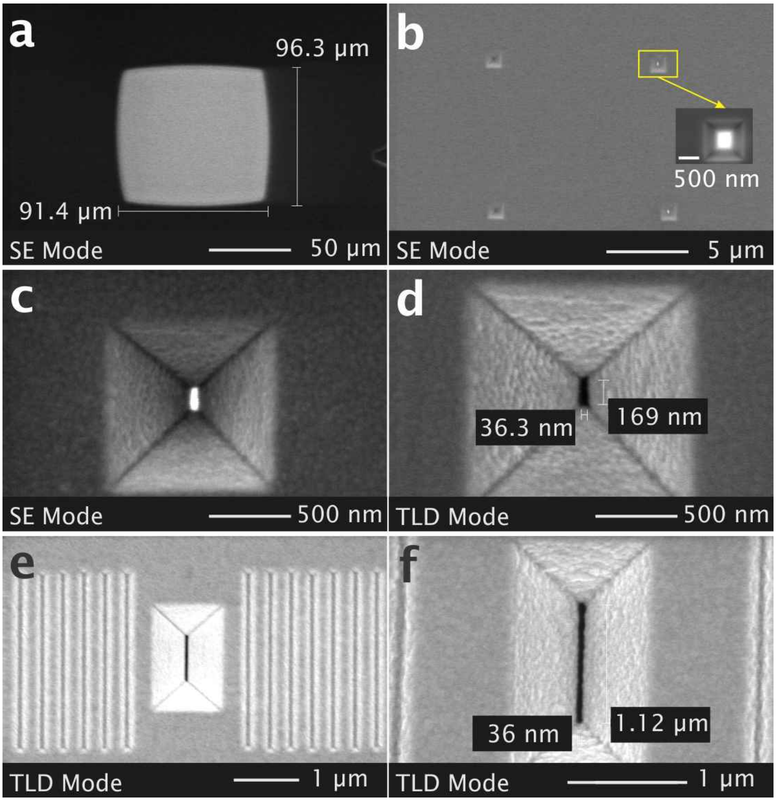

Figure 2.3: SEM images of fabricated nanocavities. (a) Silicon free-standing membrane at the accelerate voltage of 20 kV that more energetic electrons can be collected and Si membrane become bright. (b) Topview of a 2×2 nanocavity array. The left two cavities are dark at the secondary electron (SE) mode, while the right two ones are bright. The inset shows the bright case in high magnification, indicating the nanocavity has been fully opened. (c) A single nanocavity at the SE mode. (d) The through-lens-detector (TLD) mode SEM image of the device in panel (c). (e) The TLD mode of a long nanoslit cavity with Bragg mirror gratings. (f) The zoomed-in SEM image of the long nanoslit cavity. Panel b-f are taken at the accelerate voltage of 5 kV.

Step 5: To define the nanocavity, the front-side hard mask was patterned using e-beam lithography of the positive e-beam resist PMMA and a subsequent BHF selective wet etch.

Step 6: Backside mask patterning. The definition of through-wafer cavity was transferred into Si_3N_4 hard mask by dry etching.

Step 7: Pyramid shaped pits were ultimately formed in the top silicon layer using KOH etch.

Step 8: To perform the through-wafer etching, the second KOH etch was conducted for $\sim$12 hours and a large, pyramid shaped pit was formed from the backside and stopped at the BOX layer.

Step 9: To open the BOX layer, we performed 15 min BHF etching from both sides.

Step 10: For better isolation, thermal oxidation can be performed at 1200 °C for 2 h. We performed the thermal oxidation using the diffusion furnace at the department of electrical engineering, KU Leuven with the permission from Prof. Robert Puers.

The fabricated nanocavities with different geometries are illustrated in Figure 2.3 using scanning electron microscopy (SEM). We first characterize the free-standing silicon membrane, which becomes observable at the accelerate voltage of $>$15 kV. The bright area in Figure 2.3a is around 91.5×96.3 μm^2. Figure 2.3b shows a 2×2 nanocavity array in the secondary electron (SE) mode. The centers of the left two are dark, whereas that of the right two are bright. Only when the cavity is open, the spots can be bright in this SE mode, which can be explained by the fact that a lot of secondary electrons are generated when the electrons pass through the cavity/pore and hit on the metal surroundings in the SEM chamber [94]. Figure 2.3c,d illustrate a gold coated nanocavity in the SE mode and through-lens-detector (TLD) mode, respectively. The width and length of our devices are usually determined in the latter TLD mode with less scattering interference. The e-beam lithography based process flow provides us the flexibility to study various structures. For example, we also demonstrated the long-slit devices with Bragg mirror grating structures in Figure 2.3e,f. By means of this process flow, we performed the measurements in the Chapter 3, Chapter 4.2 and 4.3.

2.1.2 Wafer Scale Processing in 200 mm CMOS Fab Environment

In parallel, we developed a 200 mm wafer-level process, allowing us to massively scale up the production and the yield of the nanocavity devices. The whole process integration has been optimized at imec [95]. Figure 2.4a illustrates the frontside and backside processing steps, which use a similar flow as the above-mentioned e-beam process. Therefore we explain the different process steps with the purpose and implementation.

Wafer frontside processing

Step I: We used the same SOI wafer and deposited 50 nm CVD SiO_2 at 400 °C as the hard mask layer, which was optimized in the line. Moreover, wafer level processing allowed us to skip the dicing step.

Step II: To avoid etching the alignments into the top silicon layer, metal markers (TiN) were patterned onto the frontside surface.

Step III: The hard mask was patterned using a photoresist and 193 nm lithography followed by fluorine-based dry etching.

Step IV: To fulfill the requirement of the contamination level, the anisotropic etching behavior of tetramethylammonium hydroxide (TMAH) was used to create the nanocavities.

Wafer backside processing

Instead of long-time KOH etching of the step 8 in Figure 2.2, we utilized the deep reactive-ion dry etching (BOSCH process) [96], which can create high aspect ratio features of 200 μm thick. To avoid the risk of wafer breakage, a carrier wafer was temporarily bonded to the frontside to enable the necessary process steps on the backside using standard equipments.

Step I: Bonding glue HT10.10 from Brewer Science was spun-on the device wafer with a thickness of 16 μm and bonded to a standard 200 mm silicon wafer with 725 μm thickness as a carrier. The wafer was thinned down to 200 μm by mechanical grinding.

Step II: To withstand the BOSCH process, a 40 μm thick positive photoresist AZ 40XT from MicroChemicals was used.

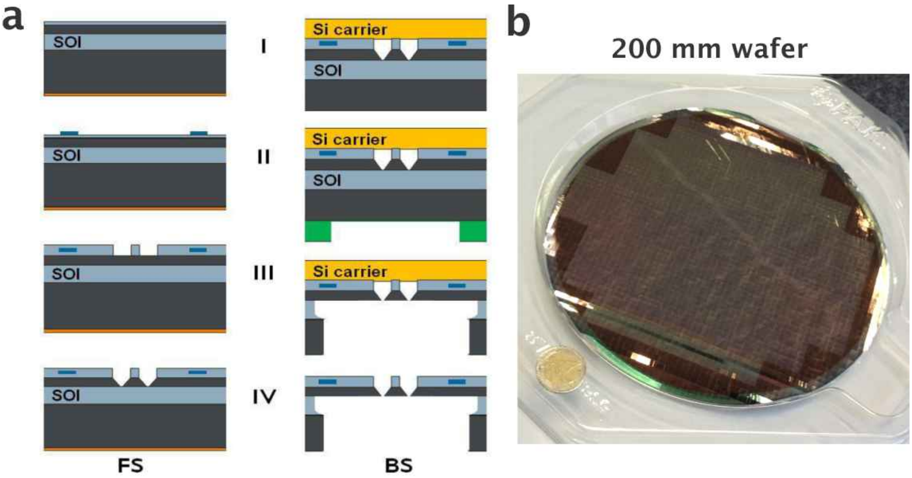

Figure 2.4: Deep UV-based process flow in 200 mm CMOS Fab environment. (a) The frontside and backside process flow for wafer-level fabrications. (b) The fabricated wafer. A coin of 2 euro is placed for the scale comparison.

Step III: The BOSCH process was conducted for 50 minutes to make the through-wafer hole of 70 μm in diameter followed by the removal of the BOX layer.

Step IV: The carrier and bonding glue were stripped.

Figure 2.4b shows the diced 200 mm wafer consisting of thousands of individual through-wafer nanocavities without the removal process of BOX layer and bonding glue.

Post processes for plasmonic nanocavities

To practically use these nanocavities, both the device wafer and the carrier one were together diced through into pieces around $21\times21\ mm^2$. Then the thinned devices were separated from the carrier substrate on a hot plate at 90 °C, leaving the bonding glue on top of the nanocavity devices. To remove the HT10.10 glue layer, NH_4OH:H_2O_2:H_2O mixture (also called as RCA-1 recipe) was preheated to 75 °C. Since the ammonia can slightly etch the silicon cavity, we used a diluted ratio of 1:3:10 until the bonding glue could be peeled off.

Then the devices after the removal of bonding glue were in a similar condition of the e-beam based devices after the step 8 (see Figure 2.2). A 15 min BHF followed by a 30 min VHF was used to facilitate the complete opening of the

BOX layer. Thermal oxidation was alternatively used to form a complete isolating layer as well. On top of the cavities, we sputtered with Ti and Au (typically 10 nm and 200 nm), which support the excitation of surface plasmons. Figure 2.5 illustrates the typical SEM images of the devices.

The regular routine to access the cross-section view is to cut through nanocavities by (focused) ion beam, which is feasible for any structures. In order to ease this procedure, we designed nanocavity arrays on the inactive area of the device with the same size as a single nanocavity. The arrays can be used for the cross-section SEM (X-SEM) after cleaving. Figure 2.5a,b show the X-SEM images of silicon nanocavities with sharp edges at the bottom of each cavity. The cavity has a depth of 700 nm and a vertex of 70.5 °. We confirmed that the BOX layer was not fully opened in 10 min BHF etching from the top side, the etch rate of which is 100 nm/min for bulk SiO_2. This can be explained by the fact that diffusion-limited chemical etching takes place in such tiny nanocavities. Figure 2.5c,d illustrate the thermally oxidized nanocavities after 15 min BHF, which is able to reach the bottom bulk silicon. The nanocavities surrounding thermal oxide exhibit smooth curvatures at the tip of each cavity in panel d. The thickness of this high-quality oxide was around 77 nm, which was confirmed by the film thickness measurement on the surfaces (not shown).

Figure 2.5e shows the frontside of a nanocavity in a large view. The nanocavities are centered at a round silicon membrane which is located at the center of the arrow markers. From the backside view in Figure 2.5f, the opened state of the nanocavity inside the deep hole can be defined when the center is bright in the SE mode. Figure 2.5g,h illustrate the two kinds of the nanocavity coated with gold layer: single short nanocavities and the identical nanocavity with Bragg-mirror gratings. Based on these two types of wafer-level devices, the systematic experiments were conducted in Chapter 3.2, 4.4 and in Chapter 5 and 6.

2.1.3 Sub-10 nm nanopore fabrication

Solid-state synthetic nanopores have been developed by means of various methods [97, 98, 99]. However, the state-of-the-art semiconductor fabrication techniques using photolithography nowadays are still limited to the feature sizes of the order of tens of nanometers [99], which is larger than the requirement for the detection of individual DNA molecules. To achieve much smaller feature sizes on the scale required for detection of biomolecules, specialized fabrication techniques have been demonstrated, such as Anisotropic wet etch with feedback [100], Ion track etching [101, 102], Metal-assisted chemical etching [103], plasma etching [104], ALD [105] or deposition induced shrinking [106, 107], Electron-

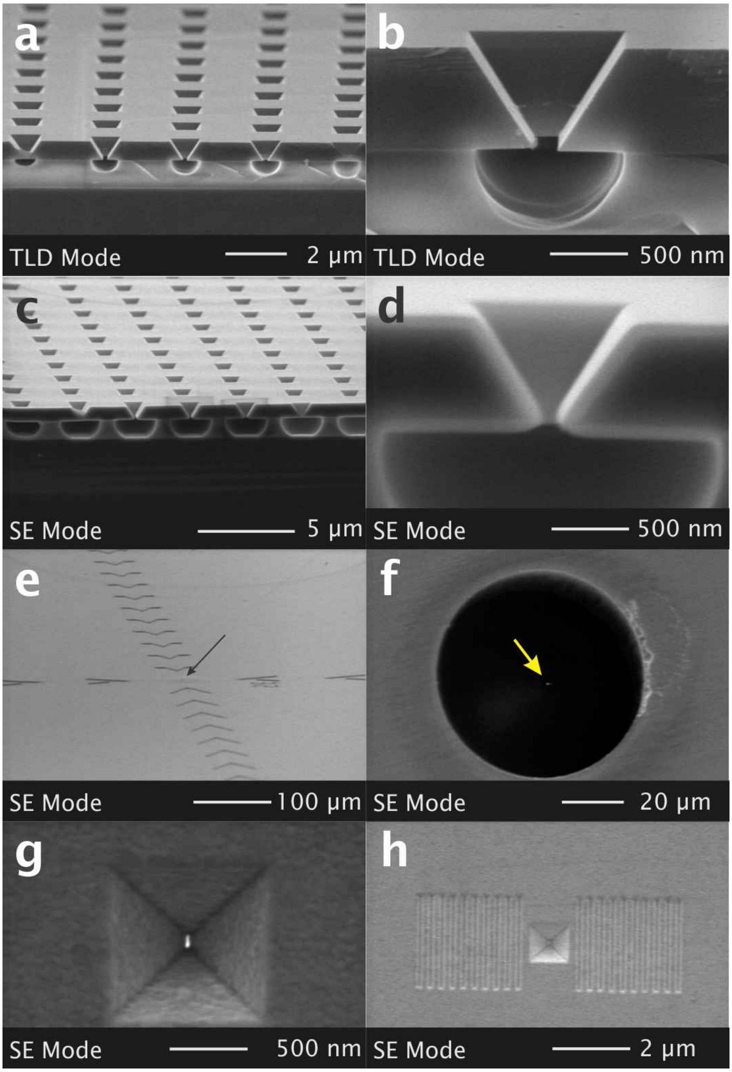

Figure 2.5: SEM images of processed nanocavity arrays. (a) Silicon nanocavity arrays after dipping into BHF for 10 min. The 1 μm buried oxide layer has not been fully opened. (b) The cross-section view of a silicon nanocavity. (c) Thermal oxidized nanocavity array. (d) The cross-section view of a thermal oxidized nanocavity. (e) The top surface with arrow markers pointing to the transmembrane nanostructure. (f) The backside view of the device with an opened nanocavity. (g) An opened gold nanocavity. (h) An opened nanocavity with Bragg-mirror gratings.

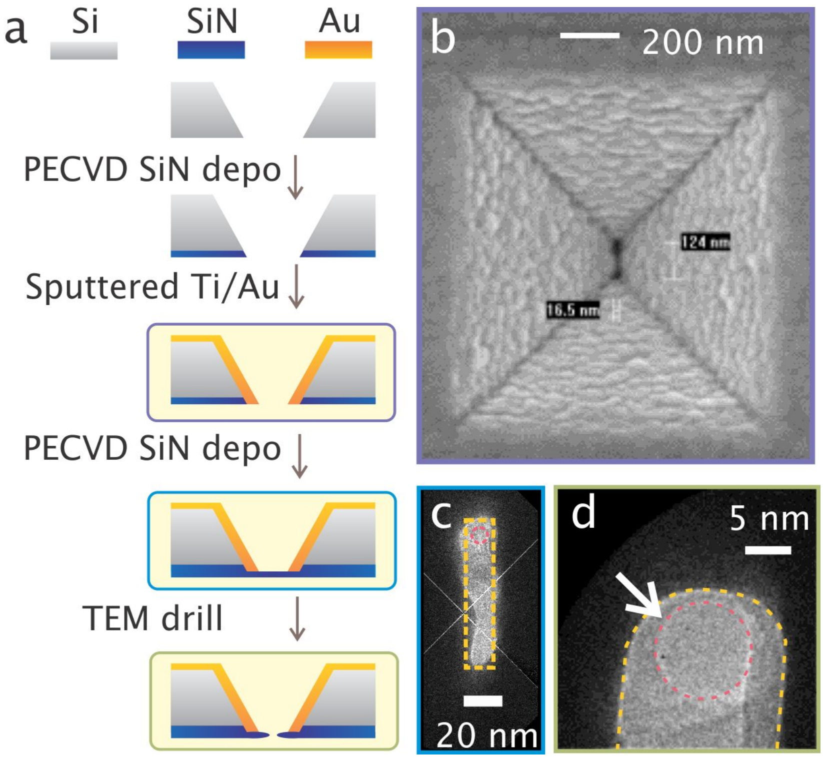

Figure 2.6: Process flow of solid-state nanopore integrated with a plasmonic nanoslit cavity. (a) The membrane formation process involves coating the silicon nitride membrane, followed by sputtering of Au and an additional layer of PECVD silicon nitride. Finally, a nanopore is drilled using a TEM. (b) SEM images of the plasmonic nanocavity. (c) TEM image of a silicon nitride membrane surrounded by the gold nanocavity. The yellow dashed line indicates the designed boundary of the gold cavity. (d) A zoomed TEM image of the top part of panel (e), showing a typical 10nm nanopore inside the gold nanocavity (marked by the arrow).

beam induced shrinking [108, 109, 110], Thermal oxidation induced shrinking [111], etc. However, most of them lack reproducibility.

To demonstrate the original device composing of a nanopore inside our nanocavities, we decided to use electron beam sculpturing. The use of e-beam can form a pore in a precise size, a delicate shape, and an exact location. We collaborated with Prof. Henny Zandbergen and Prof. Cees Dekker from TU Delft, enabling us to use the electron beam of a TEM (Philips CM300UT-

FEG operated at 200 kV, with a ~10 nA beam current and an ~10 nm beam diameter) to drill a single 10 nm-in-diameter pore through the membrane, which has been optimized for the drilling of different materials of solid-state nanopores [15, 112, 113].

Solid-state nanopore integrated with a plasmonic nanoslit cavity

To fabricate the nanopore-in-cavity devices, one may either build up gold nanocavities on top of a membrane layer, or fabricate gold nanocavities and then form a SiN membrane beneath. The latter option is more suitable for us to control the gold cavity tip and practical for our fabricated chips. Therefore we started from the silicon nanocavities processed in 200 mm CMOS Fab environment. Figure 2.6a shows the additional processing steps. First, a layer of 50 nm PECVD SiN was deposited on the backside to reduce the device capacitance. Next, gold was sputtered on top of the silicon membrane to support the excitation of surface plasmons. Another 50 nm SiN layer was then deposited from the backside to form a free-standing closed membrane at the bottom of the nanoslit. Finally, a transmission electron microscope (TEM) was used to open a single 10 nm pore in the closed membrane. Figure 2.6d shows TEM image of a final device with a SiN/Au cavity and a drilled nanopore. The characterization of such devices will be presented in Chapter 5 and 6.

2.2 Electrical measurements of nanopores

To make use of the fabricated nanocavity pore devices, as illustrated in Figure 2.7, one needs to have a flowcell containing electrolyte for both sides of the device. The flowcell should be feasible to electrically connect with a low-noise amplifier. Since we aim to combine the ionic recording with laser illumination, we will show the special designs of the optical flowcells and the configuration of the setup, which allow us to align and focus the laser on a nanopore.

Then we will discuss the electrical characterization of nanopores, including how to obtain a linear current-voltage response, how to interpret the nanopore noise and what the state-of-the-art DNA translocation events should be.

2.2.1 Flow cell and Setup

Nanopore experiments are usually performed only with electrical detection, measuring the ion transfer through the through-wafer devices. As shown in

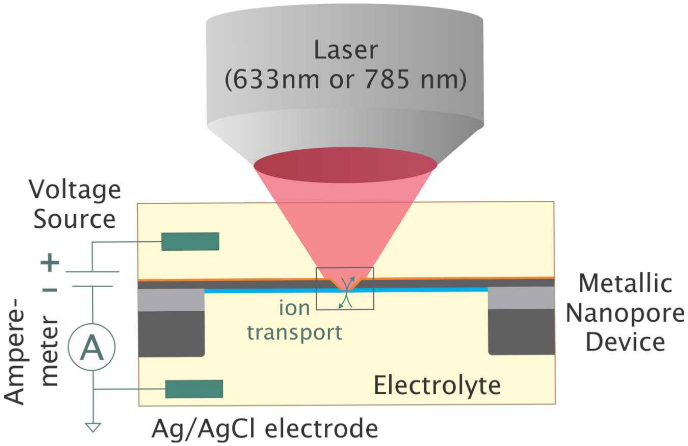

Figure 2.7: Schematic representation of an ideal flowcell for optical nanopore experiments. Metallic nanopore will seperate the electrolyte into top and bottom reservoirs. A pair of Ag/AgCl electrodes will be inserted into both reservoirs and connected to the voltage source and Amperemeter. The metallic nanopore will also be aligned with the focal spot of a laser to excite surface plasmon.

Figure 2.7, two compartments of reservoirs with voltage sourcing contacts are necessary in any flowcell design. Figure 2.8a shows a flowcell for standalone ionic characterization by pipetting very small amount of analytes. The two terminals of the flow channel in Figure 2.8a are both opened for electrolyte flushing and the placement of Ag/AgCl electrodes. The small openings at the channel terminals adapt for the tips of pipettes and effectively avoid liquid evaporation. Since our nanopore devices need to be compatible with TEM characterization and fabrication, they are often further diced into a size of 4×4 mm^2 or even smaller, which requires careful flowcell design to be handled. However, this design may not be feasible for the access of the optical objectives, which limits the usage in our applications.

To combine with optics, Figure 2.8b illustrates an optical flowcell compatible with an immersion objective lens so that it can get very close to and further focuses to nanocavity pores. In such design, we can focus light onto our designed nanocavity structure and perform ionic measurement in the two-reservoir system. In order to adapt to a potential transmission measurement or an inverted microscope, Figure 2.8c describes an improved optical flowcell, which supports light illumination from the bottom and long working-distance lens.

Our nanopore-SERS setup is depicted in Figure 2.8d: a Witec confocal Raman microscope is built on the air anti-vibration table; a Faraday cage is covered on

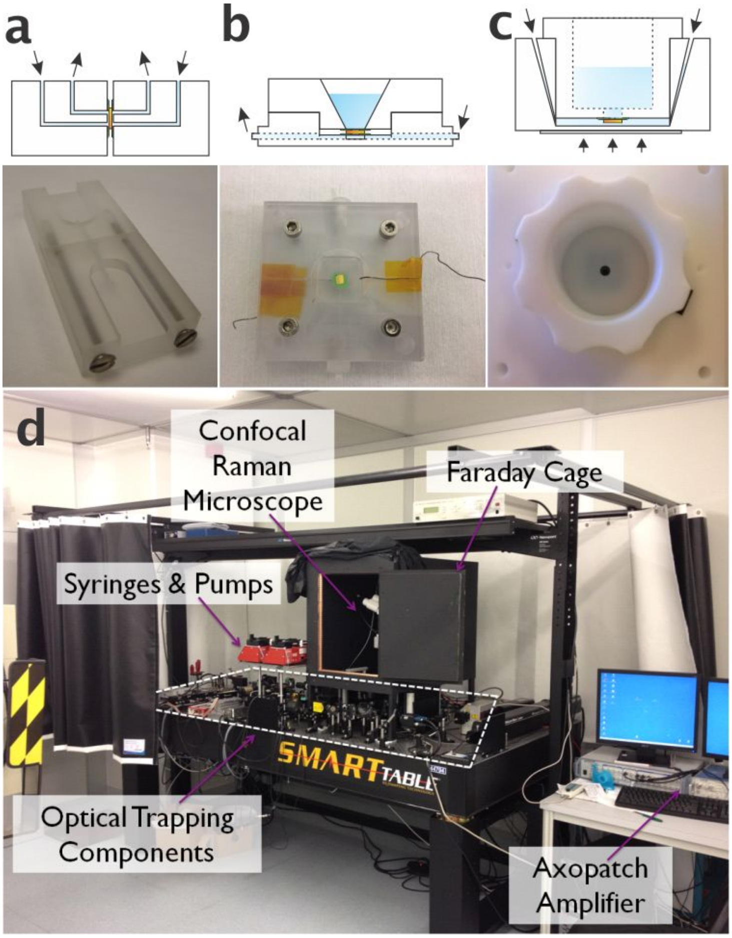

Figure 2.8: Nanopore flowcells and setup. (a) A typical flowcell only for ionic measurement of solid-state nanopores. (b) A basic version of optical nanopore flowcell. (c) An improved flowcell compatible with transmission measurement, which is derived from Dekker's group. (d) Commercial confocal Raman microscope with axon patch clamp setup.

top of the Raman microscope and used for shielding the light and the electrical interference; the optical components, syringes and pumps are arranged around; the axopatch amplifier and digitizer are connected for simultaneous recording. Here we list the experimental protocols used in this thesis.

Protocol 1: Electrical measurements for Nanocavity devices.

The chip containing a through-wafer nanocavity or a nanopore-in-cavity was rinsed with acetone, isopropanol and ethanol, and further dried with N_2 gas. For the chip fabricated in the lab, it was able to be directly exposed to the O_2 plasma treatment for 1 min on both sides, then loaded into the custom-made standalone flow cell (shown in Figure 2.8a). For the chip fabricated in the wafer scale processing, it was first glued with Kwik-Cast (World Precision Instrument) on polyacrylamide substrates, which contains a 3 mm diameter hole. To clean the chip-substrate, a 1 min O_2 plasma treatment was performed on each side. The chip-substrate was loaded into the standalone flow cell together.

Freshly prepared Ag/AgCl electrodes were placed at the openings of the flow channels. Current traces were recorded at 100 kHz bandwidth with 200 kHz sampling rate. The results will be shown and discussed in Chapter 3 and 5.

Protocol 2: Electrical noise measurements for Plasmonic Metallic Nanocavity with laser illumination.

For the electrical measurements, a chip with a nanocavity was mounted into the custom-made (PMMA) optical flow cell (shown in Figure 2.8b) to separate the electrolyte into two individual reservoirs. A buffer solution (1 M KNO_3, 10 mM Tris-acetate, and 1 mM EDTA; pH 8.0) was used during all measurements. Freshly prepared Ag/AgCl electrodes were placed at 1 cm away from the lens. Using a resistive feedback amplifier ($\beta = 0.1$, Axopatch 200B), ionic current traces were recorded at 100 kHz bandwidth with 250 kHz sampling rate. The optical properties of the nanocavity equipped with groove-gratings has been studied and optimized for 785 nm excitation in our previous works [89, 114]. For optical measurements of Figure 4.4a, a 60× water immersion lens (Olympus, NA 0.9) was dipped into the top reservoir. An incident laser (633 nm or 785 nm at 1 mW) was focused on the nanocavity with its polarization initially perpendicular to the longitudinal axis of the structure. The diameter of the laser spot was estimated as ~ 1 μm. A piezostage was used to scan a region of 20 μm by 10 μm surrounding the nanostructure in steps of 500 nm. The laser beam moved uniformly along the horizontal direction. The duration time for each point was 1 s for current signal recording with an additional 10 kHz 8-pole low-pass Bessel filtering. RMS current noises were calculated with 0.1 s traces. The results will be shown and discussed in Chapter 4.2.

Protocol 3: SERS measurements using Plasmonic Metallic Nanocavity.

Cyclic voltammetry was used to characterize the electrochemical activity of Nile Blue A on gold surfaces. We prepared the gold surfaces with 10 nm Ti and 100 nm Au to simulate the metal layer on top of our nanocavities. The gold surface as the working electrode, was mounted into a flowcell, filling with 10^{-3} M Nile Blue A either in 10 mM sodium phosphate buffer (pH = 6) or 1 M KNO_3 Tris-EDTA buffer (pH≈8). For three-electrode system, Pt foil was used as the counter electrode and saturated Ag/AgCl as the reference electrode. The cyclic voltammetry was recorded by Autolab potentiostat PGSTAT100 (Metrohm) at 0.2 V/s and shown in Figure 4.12.

For the experiments in Figure 4.13, the chip was diced into 3×3 mm^2 and rinsed by Acetone and IPA. After drying with N_2 gas, the chips were glued with Kwik-Cast (World Precision Instrument) on polyacrylamide substrates, containing a 3 mm diameter hole. Then 1 min O_2 plasma treatment was performed on each side to clean the chip. The chip was mounted in a custom-made optical flow(shown in Figure 2.8b) and filled with 10^{-5} M Nile Blue A, 1 M KNO_3, 10 mM Tris-Acetate and 1 mM EDTA buffer (pH = 8.0). A pair of Ag/AgCl electrodes were inserted into both of the reservoirs and connected with the headstage of the Axopatch 200B patch clamp amplifier (Molecular Devices Co.). The amplifier was connected to 1440A digitizer (Molecular Devices Co.) and the transmembrane voltage was applied using this instrument. For optical measurements, a 60× water immersion lens (Olympus LUMPlanFl/IR 60×/0.90W) was dipped into the top reservoir. An incident 785 nm laser (Toptica Photonics AG, Germany), with a 100 μm IRVIS fiber (QMMJ-3A3A-IRVIS-100/140-3AS-3) was focused on the nanocavity pore with its polarization initially perpendicular to the longitudinal axis of the structure. The diameter of the laser spot was estimated as 1 μm and the laser intensity was 8 mW. The Raman spectra were taken from a WITec α300 Raman setup (Wissenschaftliche Instrumente und Technologie GmbH, Germany), with the integration time of 0.1 ms.

Measurements of Figure 4.14 were performed with pre-treated chips. Double-sided gold nanopore chip was clean by O_2 plasma for 1 min. Then the chip as immersed into ethanol solution with 1 mM 4-ATP overnight. Before mounting into the optical flowcell, the chip was rinsed with excess ethanol and dry with N_2 gas. 0.1 M KNO_3 and 1 mM dAMP was used as the bulk electrolyte. The results will be illustrated and interpreted in Chapter 4.3.

Protocol 4: Experimental measurements of Nanopore-in-cavity chips with laser illumination.

To clean the surface, the chip was rinsed with acetone, isopropanol and ethanol. Then a 30 s O_2 plasma treatment was performed on each side of the chip to remove any trace of organic materials and to aid the surface wettability. The chip was immediately mounted onto a custom-made optical flow cell(shown in Figure 2.8c) with Kwik-Cast (World Precision Instrument). Then the chip was placed between the two flow cell's independent chambers which were filled with 1 M KCl, 10 mM Tris and 1 mM EDTA buffer (pH = 8.0). The solutions were previously degassed in a vacuum chamber for 0.5 h. A pair of Ag/AgCl electrodes were inserted into both reservoirs and connected to the headstage of the Axopatch. We used an Axopatch 200B patch clamp amplifier (Molecular Devices Cooperation) at 100 kHz and NI USB-6251 (National instruments) at 500 kHz sampling rate for ionic current recording. The results will be investigated in Chapter 6.

2.2.2 IV Linearity

For practical nanopore experiments, the electrical characterization can be sophisticated. Ion current through the nanopores is recorded by means of electron transfer through electrodes which are connected to the amplifier and digitizer. Besides ion transport and electron transport, two reversible electrochemical reactions take place at the interfaces [8]. Typically, non-polarizable electrodes [8, 115] with fast kinetics such as Ag/AgCl are performed under biases lower than 1 V. At larger bias values, water and other species could likely become electrochemically active, resulting in nonlinear electrochemical processes and significant pH instability in weakly buffered solutions (less prevalent in smaller pores due to their high resistance). Solid AgCl can be synthesized at the anode electrode (+), whereas at the cathode electrode (-) the AgCl on the surface can be dissociated to silver element and chloride ions. In the bias window of ±1 V vs. Ag/AgCl for aq. KCl [8, 116], a nanopore without overlapping electrical double layer (EDL) can thus offer a linear (Ohmic) current–voltage response. Only in this case, the analytical equation for baseline ion current I_0 has been given by Wanunu [8] as

$$I_0 = V \cdot (c_+\mu_+ + c_-\mu_-)N_A e \cdot (\frac{4h}{\pi d^2} + \frac{1}{d})^{-1} + \frac{V\mu_0\pi d\sigma}{h} \tag{2.1}$$

where c_+ and μ_+ are the concentration and solution mobility of positively charged ions (here is K^+), c_- and μ_- for the negatively charged ions (especially for Cl^-), h and d are the height and diameter of a nanopore, and μ_0 is the solution mobility for electroosmosis. The baseline current can be jointly determined by the solution conductivity term of $(c_+\mu_+ + c_-\mu_-)N_Ae$, the geometric term $\frac{4h}{\pi d^2}$, the access resistance $\frac{1}{d}$ and the electroosmotic term $\frac{V\mu_0\pi d\sigma}{h}$ [8].

In the protocols used in this thesis, KCl is sometimes replaced with KNO_3, which is mainly due to the corrosion of gold nanostructures at high bias potential or upon high-powered laser illumination. The experiments using KNO_3 are similar to the ones with KCl, while the reactions at the Ag/AgCl electrodes may slightly different. On one hand, at the cathode electrode (-) the AgCl on the surface can be dissociated to silver element and chloride ions. This can be confirmed by the evidents that the SERS peak for chloride ion can come out in the experiment using KNO_3. On the other hand, due to the lack of chloride ions, the silver element can only be oxidized to silver ions. Other electrochemical process such as the electron transfer of protons can facilitate the reactions on the electrodes.

2.2.3 Device Noise

A nanopore sensing system that produces weak ionic currents is generally constrained not by small-amplitude of response but by the signal-to-noise ratio (SNR) [74]. To heavily suppress the noise, one need to analyze the noise components and their noise sources.

Figure 2.9a,b show the noise components on the noise spectrum. In the low-frequency regime (<100 Hz), nanopore noise power spectral density (PSD) is dominated by flicker noise, which follows Hooge's relation [117]

$$S_{-1}(f) = \frac{\alpha I^2}{c_0 N_A f} \tag{2.2}$$

where α denotes the Hooge parameter, I is the current, and c_0N_A stands for the number of charge carriers. At moderate frequencies (100–10k Hz), the sources of thermal noise $S_T(f)$ and shot noise $S_{shot}(f)$ can become dominant, the equations of which are defined as

$$S_T(f) = 4kT/R \tag{2.3}$$

$$S_{shot}(f) = 2eI \tag{2.4}$$

Noise generated by energy dissipation in non-ideal dielectric materials also appears in this middle frequency region. The dielectric loss $S_1(f)$ can be expressed as [118]

$$S_1(f) = 8\pi k_B TDCf \tag{2.5}$$

where D is the dielectric loss factor and C is the device capacitance [119, 118]. Finally, at frequencies >10 kHz, the dominant noise source is the interaction of the amplifier's voltage noise with the total capacitance at the input. The trans-impedance noise $S_2(f)$ is denoted by

$$S_2(f) = 4\pi^2 S_v C^2 f^2 \tag{2.6}$$

where S_v is the spectral density of the voltage noise. The overall noise can be considered as the sum of all kinds of noise, followed by

$$S(f) = Af^{-1} + B + Cf + Df^2. \tag{2.7}$$

where $A - D$ are the fitting parameters. The measured noise spectrum in Figure 2.9b can be well fitted and explained by all the known noise sources. Besides all the conventional noise sources, in this thesis we will also investigate another type of noise which can be fitted by Lorentzian components. A single Lorentzian function, as the simplest case of current fluctuation or step-like transitions, represents the statistical process of only two states. The parameter of a single Lorentzian model is the corner frequency $f_{c,i}$, which is related to the relaxation time constant $\tau_{on,i}$ and $\tau_{off,i}$.

$$f_{c,i} = \frac{1}{2\pi\tau_i} = \frac{1}{2\pi}(\frac{1}{\tau_{on,i}} + \frac{1}{\tau_{off,i}}) \tag{2.8}$$

Therefore the noise power density generated by burst signals is considered as the sum of single Lorentzian-shaped model with fast and slow frequencies. The presentation of this noise source will be given in Chapter 4.2.

2.2.4 DNA translocations as typical events

Given a diameter-of-10 nm SiN nanopore with 20 nm thin membrane, the statistical information of 48.5 kilo base-pairs (bp) DNA (from Phage lambda DNA) can be scattered to the event amplitude and event time. In Figure 2.9c, yielding a mean amplitude of 1.25 nS and a mean translocation time at 1.72±0.29 ms [120]. Since the scatter plot is very sensitive to the pore diameter, membrane thickness, pore material, electrolyte species and DNA length, the DNA experiments in the thesis are designed with all the same parameters. An exception is the membrane thickness, which we have to adjust in our own processes.

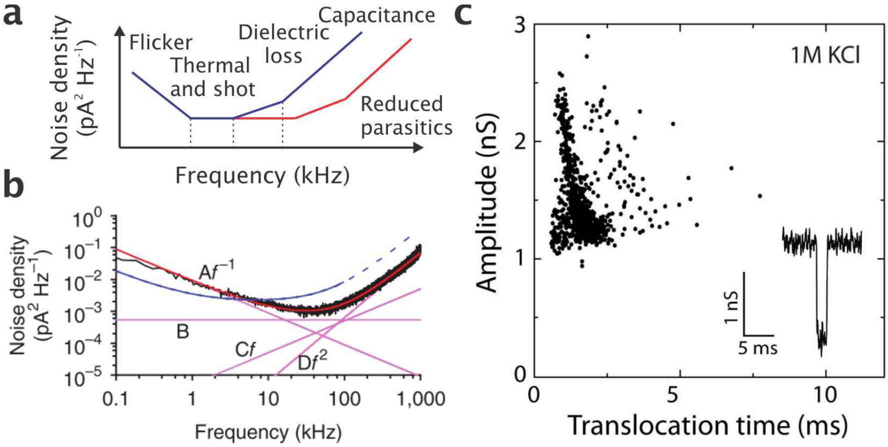

Figure 2.9: The state-of-the-art of nanopore noise and DNA events. (a) Dominant sources of noise power spectral density, illustrated as a function of frequency [74]. (b) The noise spectrum of a typical nanopore device [74]. (c) The scatter plot of blockage amplitude and translocation time of lambda DNA events at 1M KCl [120].

2.3 Numerical simulation

Electrical characterizations of solid-state nanopores in the section 2.2 have shown the capability to reflect many of important information, including the device performance and the interaction between DNA and a pore device. We are motivated to understand the theoretical background of the nanopore fluidics. In this section, we start with the basis of nanopore fluidics, such as the build-up of electoral potential profile, ion concentration profile and velocity profile. Next, we give a fundamental introduction on the excitation of surface plasmon and plasmonic induced Joule heating. Then we discuss the heat transport, the temperature sensitive properties and their influence in the simulation.

2.3.1 Electrical and fluidic simulation

Nanopore fluidic system is composed of the electrophoresis of ions and molecules through a nanopore, which is based on the build-up of electric field. The electric field can be efficient when scaling down to nanoscale. Therefore, we start with the Electrostatics simulation in the system.

Poisson equation (Electrostatics)

To build up such electric field, external voltage V_0 is applied between the two compartments. The electric field $\vec{E}$ is determined by the distribution of volume charges ρ_v in the electrolyte. This relationship can be expressed by Poisson equation,

$$\nabla\vec{E} = -\frac{\rho_v}{\varepsilon_0\varepsilon_r} \tag{2.9}$$

where ε_0 and ε_r are the dielectric constant and relative permittivity. The volume charge ρ_v (also called space charge density) can be expressed as

$$\rho_v = qN_A\sum_i z_i c_i \tag{2.10}$$

where q is the element charge, N_A is the Avogadro constant, and $z_i$and c_i are the valence and concentration of species in the electrolyte. Surface charge density and floating potential can be derived from the following equations

$$\vec{n}\cdot(\vec{E}_1 - \vec{E}_2) = -\frac{\rho_s}{\varepsilon_0\varepsilon_r} \tag{2.11}$$

where $\vec{n}$ is the unit normal vector directed from the boundary surface to the fluid, $\vec{E}_1$,$\vec{E}_2$ describe the electrostatic fields at the two sides of the boundary surface, and ρ_s is the surface charge density. The floating potential can be given by

$$\int_{\partial\Omega}\vec{E}\cdot\vec{n}dS = Q_0 \qquad in \qquad \Omega, \tag{2.12}$$

where Ω is the overall surface (in most of the cases are metals) with a total charge Q_0 deposited on it or connected to an external circuit. Electrical field distribution can be calculated by the charges on the interfaces and the concentration profiles of species. Therefore, we next go to the principles of ion transport.

Nernst-Planck equation (Ion transport)

In the absence of chemical reactions, the transport of species inward or outward a nanopore features three means of transports: diffusion, convection and migration. Fick's law defines a flux density of species proportional to the gradient of the species concentration and the diffusivity of the species in the solvent, the flux density of a diffusive specie is given as:

$$\vec{J}_{diff,i} = -D_i\nabla c_i \tag{2.13}$$

where D_i is the diffusivity of species i in the electrolyte. This equation can be applied in the diluted solution limit with negligible thermodiffusion effects. In addition to the random fluctuations of ions due to thermal motion, the deterministic motion of ions due to fluid flow also leads to a species flux density, which is the convective flux density of the species as follows,

$$\vec{J}_{conv,i} = c_i\vec{u} \tag{2.14}$$

where $\vec{u}$ is the velocity of all species. Moreover, the ion species can drift due to the electric field, resulting in the drift flux density.

$$\vec{J}_{drift,i} = -z_i c_i \mu_i \nabla V \tag{2.15}$$

where μ_i is the solution mobility (the migration in electric field), $z_i$and c_i are the valence and concentration of species described in Equation 2.10 and V is the external potential drop. In general, the transport of a species i can be described by means of the Nernst-Planck equations:

$$\frac{\partial c_i}{\partial t} + \nabla \cdot (-D_i \nabla c_i - z_i c_i \mu_i \nabla V + c_i \vec{u}) = 0 \tag{2.16}$$

$$\nabla(c_i\vec{u}) = c_i \nabla \vec{u} + \vec{u} \nabla c_i \tag{2.17}$$

For incompressible fluid flows, the divergence of the fluid velocity $c_i\nabla\vec{u}$ is zero owing to conservation of mass. The local conductivity σ can be derived from

$$\sigma = F \sum_i c_i |z_i| \mu_i \tag{2.18}$$

where F is the Faraday constant. For the univalent species of potassiumn chloride $i = K^+, Cl^-$, we can collect ion current flow I by integrating the overall flux,

$$I = -F \int_S (\vec{J}_{K^+} - \vec{J}_{Cl^-}) \cdot \vec{n} dS \tag{2.19}$$

where $\vec{J}_{K^+}$ and $\vec{J}_{Cl^-}$ are the total flux of the two species K^+ and Cl^-. The ion transport is governed both by electrical potential profile and hydrodynamic velocity profile. When $\vec{u}$ is neglectable, the ion concentration and electric field distribution can be solved by coupling the equations 2.9 and 2.16. However, the existence of $\vec{u}$ drives us to look into the theory of the hydrodynamics.

Navier-Stokes equation (Hydrodynamics)

The motion of viscous fluid substances obeys Navier-Stokes momentum equation. For water in nanochannels, it can be assumed that the material density is constant within an infinitesimal volume that moves with the flow velocity [121]. This incompressible laminar flow gives an equation in the form of

$$\rho\frac{\partial\vec{u}}{\partial t}+\rho(\vec{u}\cdot\nabla)\vec{u}=\nabla\cdot[-\rho\vec{I}+\eta(\nabla\vec{u}+(\nabla\vec{u})^T)]+\vec{F} \tag{2.20}$$

where ρ is the fluid density, η is the dynamic viscosity, $\vec{I}$ is the identity matrix and $\vec{F}$ is the volume force. For the electrophoretic driven flow, the volume force can be expressed as $\vec{F}=\rho_v\vec{E}$. Coupling the above-mentioned three equations of 2.9, 2.16 and 2.20, we can obtain a complete model for nanofluidic study. We have found out that the results using the numerical simulation was in agreement with the experimental results on the current rectification effects [122] and the salt dependent conductance changes of translocated DNA [123]. This confirms the feasibility of our model in interpreting the characterizations, and may pave the way to understand the ionic transport and translocation process in our fabricated nanocavities and further upon light illuminations.

2.3.2 Plasmonic simulation

The excitation of surface plasmons obeys the Maxwell's equations by means of electromagnetic waves. The analysis of surface plasmon on a macroscopic level is the core element in solving Maxwell's equations subject to certain boundary conditions, which can be implemented in Radio Frequency (RF) module of Comsol Multiphysics. Comsol uses the finite element method (FEM) to find an approximate solution of partial differential equations (PDE) and integral equations, whereas the competitive finite-difference time domain (FDTD) solves the equations in a cyclic manner based on the grid differential time-domain methods. Moreover, we can couple the plasmonic simulation not only with heat transfer module in the comsol, but also with the three modules in section 2.3.1 to interpret the fluidic cases. First, we will describe the simulations for the plasmonics and the heat transfer in the system. Then we will show the modified model when the temperature changes is taken into consideration.

The interaction of metals with electro-magnetic fields can be completely described in the framework of classic Maxwell equations:

$$\begin{gathered}\nabla\cdot D=\rho,\qquad \nabla\cdot B=0\\ \nabla\times E=-\frac{\partial B}{\partial t},\qquad \nabla\times H=J+\frac{\partial D}{\partial t}\end{gathered} \tag{2.21}$$

where the dielectric displacement D, electric field E, magnetic field H and magnetic induction B interact with an external charge density ρ and current density J. When we limit ourselves in the linear, isotropic and non-magnetic media, we can apply the following material-dependent relations:

$$D = \varepsilon_0 \varepsilon E, \qquad B = \mu_0 H \tag{2.22}$$

where ε_0 is the absolute dielectric constant, and relative dielectric constant ε is frequency dependent, expressed as $\varepsilon(\omega)$. In a more general complex function, $\varepsilon = \varepsilon^{'} + i\varepsilon^{"} = n^2 - \kappa^2$. The real part of the refractive index $n(\omega)$ is responsible for the dispersion in the medium, while the imaginary part $\kappa(\omega)$ determines the absorption (extinction coefficient).

Electromagnetic heating

Heat generation is one of the characteristics of plasmonic structures. The electric field strongly drives mobile carriers, and the energy gained by carriers turns into heat. The heat source density Q can be described as

$$Q = \vec{E} \cdot \vec{J} = \varepsilon_0 \omega Im(\varepsilon_m)|\vec{E}|^2 \tag{2.23}$$

where $\vec{E}$ is the electric field, $\vec{J}$ is the current density and ω is the angular frequency. The heat density can be commonly expressed as a function of the incident electric field and imaginary part of the metal permittivity ε_m. Therefore we can input the plasmonic heat density into a heat transfer system to calculate the temperature distribution.

Heat transfer equation

Thermal energy can be physically transferred from a hot object to a cold one and vice versa. The fundamental of heat transfer is the convection–diffusion equation. On one side, advection (or Convection) is the transport mechanism of a fluid substance or conserved property from one location to another, depending on motion and momentum, which can be described by the formula

$$Q_a = \rho C_p \vec{u} \cdot \nabla T \tag{2.24}$$

where Q_a is heat advective flux, ρ is the density, C_p is the heat capacity at constant pressure and $\vec{u}$ is the fluid velocity. On the other side, heat conduction (diffusion) occurs between objects in physical contact, which is evaluated primarily in terms of Fourier's Law

$$Q_c = -\kappa \nabla^2 T \tag{2.25}$$

where κ is the thermal conductivity. Heat conduction flux Q_c is typically proportional to the temperature gradient.The fundamental law governing all heat transfer is the first law of thermodynamics, referred to the conservation of energy. For a fluid system, the resulting equation is

$$\rho C_p \frac{\partial T}{\partial t} + \rho C_p \vec{u} \cdot \nabla T = \kappa \nabla^2 T + Q_{ext} \tag{2.26}$$

where Q_{ext} contains external heat sources other than convection and conduction, such as heat radiation. In the above-mentioned equation, four terms represent transient, convection, diffusion and source term, respectively.

Here we note that the boundaries in any heat simulations are distance-dependent because of the analytical solutions of line heat source in two-dimension and point heat source in three-dimension cases, as follows

$$T_{2D}(r) = -\frac{Q}{2\pi\kappa} \ln r, \qquad T_{3D}(r) = \frac{Q}{4\pi\kappa r} \tag{2.27}$$

Both of the boundary conditions are strongly related with locations r, which means one cannot simply assign a constant value at any boundaries. To converge our simulation, we suggest to use large geometry (usually $>10^3$ time larger than the heat source). Thus, the boundary conditions for two-dimensional and three-dimensional cases need to be carefully configured with the above-mentioned equation to obtain accurate results.

Modified equations within variant thermal conditions

To integrate heat transfer equations into the coupled system in section 2.3.1, we also need to rearrange the Nernst-Planck equation (Equation 2.16) with thermal diffusion of specific ions. The formula has been modified by He et al [43] as

$$\frac{\partial c_i}{\partial t} + \nabla \cdot (-D_i \nabla c_i - z_i c_i \mu_i \nabla V + c_i \vec{u} - c_i D_{T,i} \nabla T) = 0 \tag{2.28}$$

where $D_{T,i}$ is the thermo-diffusion coefficient. The quotient between thermo-diffusion and regular diffusion coefficient is defined as Soret coefficient $S_{T,i} = D_{T,i}/D_i$. For the volume force of the Navier-Stokes equation, one has to consider the variation of water density due to temperature changes [43]. The Buoyancy force can be described by Boussinesq approximation $\vec{F} = \rho_v \vec{E} + \vec{g} \Delta \rho$. We can conduct numerical simulations by coupling all the five modules for the characterization of our plasmofluidic nanopores.

2.4 Conclusions

We have introduced the fabrication and characterization approaches used in this thesis. Two fabrication flows of nanocavities have been discussed: the former one is feasible for can be flexible for research purposes and the later one could be interesting for the industrial purposes. The described setup and flowcells for simultaneous electrical and optical detections ensure the reproducibility of the practical experiments.

We have also outlined the principles behind our electrical characterization, including the numerical simulations of I-V responses, plasmonic excitations and heating effects. The comparison between theoretical calculations and experimental results will be given in the coming Chapter 3-6, which could provide us a better understanding of our plasmonic nanopore system.

Chapter 3

Characterization of metallic nanocavities without laser irradiation

In this chapter, we will show the experimental use of metallic nanocavities for ionic fluidic recording and how we benchmark the ionic performance of the devices without laser illumination. Rather than using dielectric materials as the conventional membrane materials, our designed nanopores introduce a gold layer to support surface plasmons, the performance of which has not been widely studied. The degradation of ionic performance has been found in different types of metallic nanopores. One example is the introduction of a continuous metal layer, which has been reported to give rise to an increased noise level [106] of ionic recording. Moreover, some fluidic issues have been reported on metallic micro-/nanochannels, such as a large preconcentration in fluidic transport [124, 125, 126, 127], the increase of voltage charging governed conductivity [128] and DNA translocation events with long passage time [129, 130]. The potential risks of using metals drive us to investigate and optimize the ionic properties of our metallic nanocavities.

3.1 Introduction

Ionic transport phenomena are highly regulated by the interfaces that form the pore/cavity channel. This becomes more critical in nanometer scale due to the reduction of the electrolyte volume and the effective government of the ion flow by the interfaces. Based on silicon nanocavities, we designed and fabricated several types of nanocavities. These cavities with different material stacks allow us to validate the change of the critical interfaces. We therefore systematically investigated the ionic properties of metallic nanocavities from different aspects such as current-voltage curves, device conductivity, noise spectra and DNA translocation events.

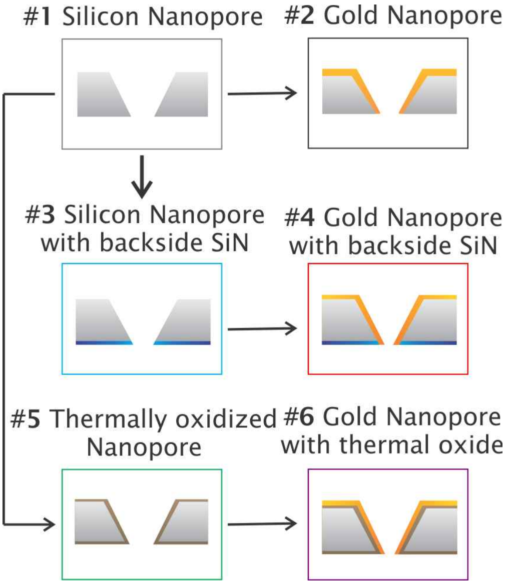

Figure 3.1: Schematic cross-section of six types of nanocavities: #1 - Silicon cavity, #2 - Gold cavity, #3 - Silicon cavity with backside SiN, #4 - gold cavity with backside SiN, #5 – Thermally oxidized silicon cavity, and #6 – gold nanocavity with thermally oxide. Only the nanocavities on the membrane have been shown here.

Figure 3.1 describes the six types of nanocavity devices. Briefly, silicon nanocavities (#1) were fabricated based on standard micromachining procedures in Chapter 2.1 [131, 95]. At the backside of device #1, a layer of 50 nm PECVD SiN was deposited to form device #3. Thermal oxide enables us to passivate the entire silicon cavity, which becomes important not only for backside passivation but also for capacitance considerations. A thermal oxide of 77 nm was used for device #5. To metallize the device #1, #3 and #5, 10 nm Ti and 200 nm Au were sputtered on top of them, deriving gold nanocavities (#2), gold nanocavities with backside SiN (#4) and gold nanocavities with thermal oxide (#6). The fabrication details of these six kinds of devices have been introduced in section 2.1. For all the experiments in this chapter, we used protocol 1 which has been described in section 2.2.

3.2 IV Linearity and Device Conductivity

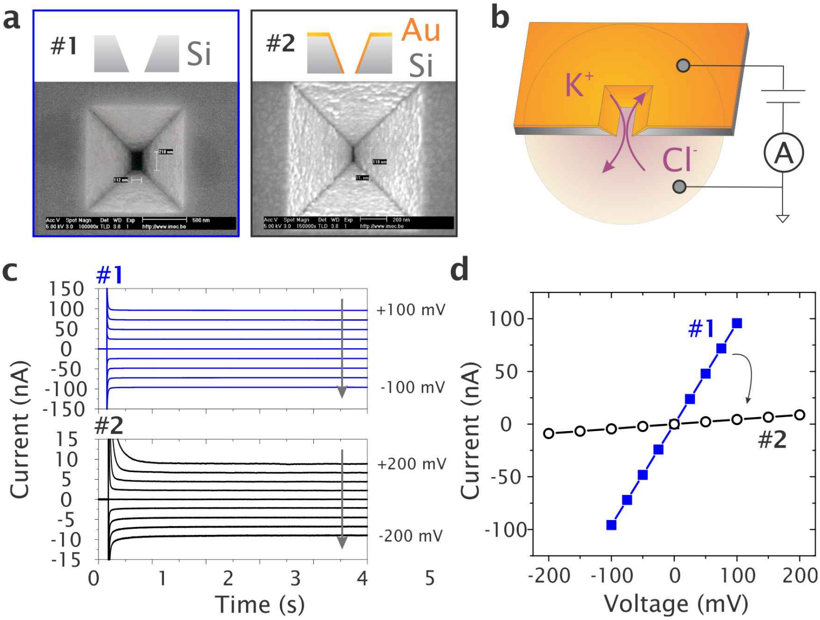

Figure 3.2: (a) SEM images of device #1 and #2 nanocavities. (b) Schematic representation of the experimental geometry. Ion transport (Typically Potassium and Chloride ions) through a nanocavity is monitored by means of ionic current. We used 1 M KCl, 10 mM Tris and 1 mM EDTA (pH=8.0) as the electrolyte. (c) Ionic current trace as a function of time. The bias voltages for silicon nanocavity (#1) are applied at 0.2 s from +100 mV to -100 mV with a step of -25 mV, while the applied voltages across the gold nanocavity (#2) go from +200 mV to -200 mV with the stepsize of -50 mV. (d) The average current-voltage (I-V) plot of the data from panel (c).

We start from the comparison between the silicon and gold nanocavities (#1 and #2). Figure 3.2a shows top-view SEM images of these two nanocavities. The initial size of the silicon nanocavity is 110×218 nm^2. Due to the sputtering of gold layer on top, the size of device #2 goes down to 11.5×95 nm^2. The scheme of ionic measurement is illustrated in in Figure 3.2b. In short, the nanocavity chip was mounted into a custom-made flow cell, separating the electrolyte into two compartments. The buffer compartments were externally connected using Ag/AgCl electrodes. The electrical potential was applied to the side with the gold cavity, and the other side facing to the dielectrics was connected to ground. The ion current through a cavity was monitored using an external amplifier.

Figure 3.2c depicts the ionic current traces at different bias voltages triggered at 0.2 s. The current responses become stable after about 1 s. We calculate the mean values for the traces at 2-4 s and plot them as a function of the applied voltages in Figure 3.2d. Compared to the I-V slope of the silicon nanocavity, we can observe a dramatic decrease in that of the gold one. The strong current drop shows that the shrunken cavity volume can lead to the reduction of ion transport through the gold cavity.

From the prior reports [109, 132], we know that salt dependence of ion transport through silicon and SiN nanopores can be well explained by a model that accounts for the pore geometry and sidewall charges [109]. To understand the role of the gold layer on the nanopores, we characterize the conductance properties of the devices from 0.1 mM KCl to 1 M KCl (pH = 8.0). Figure 3.3 shows the device conductivity as a function of salt concentration for these six kinds of nanocavities in Figure 3.1. The conductivity of silicon nanocavity (#1) with the size of 110×218 nm^2 exhibits a salt concentration dependency, which becomes linear to the concentration larger than 10 mM and goes to a plateau when the molarity is lower than 1 mM. This is typical in agreement with the cavity nanopore model [109]. At high salts, the conductivity of KCl governs the device conductivity, whereas the device conductivity is dominated by surface charges at low salts. For our rectangular nanocavity, the nanopore conductance can be expressed as the following equation

$$G = \frac{WL}{H}\frac{F^2}{RT}\sum_i z_i c_i D_i \tag{3.1}$$

where G is the nanopore conductance, W and L are the width and length of bottom rectangle vertex inside the nanocavity, H is the height of the membrane thickness, F is the Faraday constant, R is the gas constant, T is the temperature, z_i is the ion valence and D_i is the diffusion constant for each specie i. The concentration for each specie is described by Kox et al [109] as

$$c_i = -z_i X + \sqrt{X^2 + 4c_0^2}. \tag{3.2}$$

Here c_0 presents the bulk concentration and X is the parameter introduced to account for the fixed surface charges, which can be written as

$$X = \frac{2\sigma(W+L)}{FWL}, \tag{3.3}$$

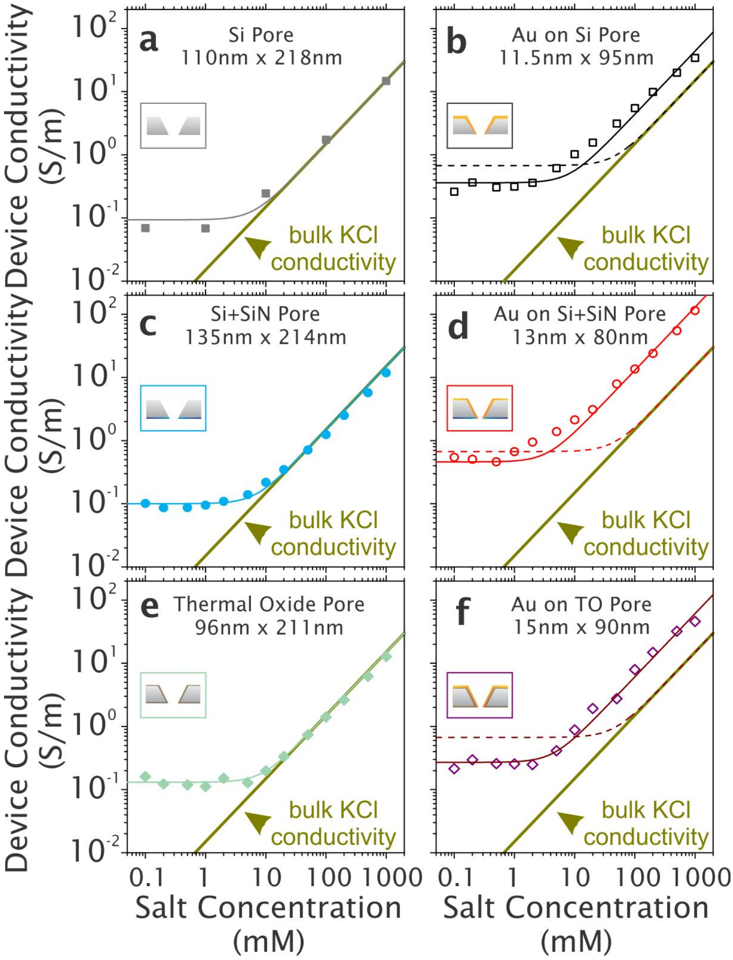

Figure 3.3: Device conductivity versus KCl concentration. (a) #1: Silicon nanocavity. The grey curve shows the analytical model (Equation 3.1-3.3) with σ*=-45.5 mC/m*^{2}*.(b) #2: Gold nanocavity. The black dashed curve indicates the expected result for shrunken one with the same surface charge, while the solid black line presents the best fit of the experimental data with enlarged width and length and reduced surface charges. (c) #3: Silicon nanocavity with backside SiN. The light blue curve shows the same fitting as in panel (a) with* σ*=-49.4 mC/m*^{2}*. (d) #4: Gold nanocavity with backside SiN passivation. The red dashed and solid curves indicate the same fittings as in panel (b). (e) #5: Thermally oxidized silicon nanocavity. The green curve shows the same fitting as in panel (a) with* σ*=-46.8 mC/m*^{2}*. (f) #6: Gold nanocavity with thermal oxide. The purple dashed and solid curves indicate the same fittings as in panel (b). The bulk conductivity of KCl is marked in yellow line.*

where σ is the surface charge density of a given pore material. Here we define the device conductivity as the conductance normalized by the nanopore geometry, which can be expressed as

$$\sigma_d = \frac{F^2}{RT} \sum_i z_i D_i(-z_i X + \sqrt{X^2 + 4c_0^2}). \tag{3.4}$$

When the salt concentration c_0 is dominant, the parameter X can be neglected and lead σ_d to $\frac{F^2}{RT} \sum_i z_i D_i c_0$. However, in the surface charge governed regime, the device conductivity becomes geometry-dependent. Our measured result in Figure 3.3a is well fitted using this model (grey line), yielding surface charge density σ = -45.5 mC/m^2. Since the silicon surface always contains a layer of native oxide, the estimated value of σ is consistent with the reports for SiO_2 [133].

Figure 3.3b shows the measured data (hollow squares) of gold nanocavities (#2). In order to validate the analytical model for metallic nanocavities, we plot the dashed black curve with the shrunken size and the same value of σ. In the geometry controlled regime (high salts), the device conductivity is expected to have the same conductivity as KCl using the fixed charged model. However, the measured device conductivity is higher than the predicted one (the dashed curve in Figure 3.3b).

We also characterize the conductivity for the devices #3 (solid circles) and #4 (hollow circles) with SiN on the backside, and the devices #5 (solid diamonds) and #6 (hollow diamonds) using thermal oxide on both sides.

In Figure 3.3c,e, the device conductivities of the two devices overlap with KCl conductivity at high salts, and reach a plateau at low salts, which are similar to the behavior of device #1 in Figure 3.3a. The result of device #3 with an area of 135×214 nm^2 can be well fitted with the model using the surface charge density σ = -49.4 mC/m^2. This surface charge density is found to be reasonable for SiN interfaces [133]. In Figure 3.3e, the result of device #5 with an area of 96×211 nm^2 yields to σ = -46.8 mC/m^2, which is also in line with the literature [133].

In Figure 3.3d,f, the measured device conductivities are both higher than that of KCl, but not fitted with our predictions based on the Equation 3.1-3.3. The results are similar to that of device #2. The high conductivity at high salts for the gold coated devices (#2 ,#4 and #6) can be attributed to the following hypotheses. One could be the high surface charge density on gold surfaces. The surface charge density of gold surface has been characterized up to -320 mC/m^2 [134, 135], in which the assumption of electrical double layer at low surface charge density could be not feasible. When configuring the surface charged density at -320 mC/m^2 in numerical simulations, we can obtain a much larger conductance with the same geometry. The second one could be the induced-charge depletion [136, 137] and enhanced ionic conductivity by voltage charging [128], which have been reported on gold nanochannels. Due to the access of free electrons or the electron transfer at the gold interfaces, the measured current could be enhanced rather than the conventional transport in dielectric nanopores. They may all contribute to our observations of the gold nanocavities and still need further investigations.

3.3 Noise Performance

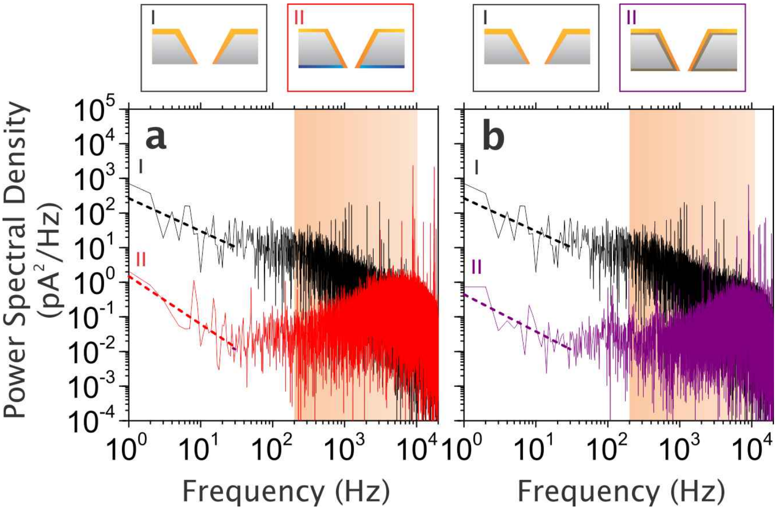

Figure 3.4: Noise performances of gold nanocavity devices. (a) Noise spectra of ***#2*** *and* ***#4****. (b)Noise spectra of* ***#2*** *and* ***#6****. Black curve indicates gold nanocavity (****#2****), red one for* ***#4*** *(gold nanocavity with backside SiN in red) and purple one for* ***#6*** *(gold nanocavity with thermal oxides). We use 1 M KCl, 10 mM Tris and 1 mM EDTA (pH = 8.0) as the electrolyte. All the traces are measured at +100 mV and filtered at 10k Hz. The orange window from 100 Hz to 10k Hz represents the region of interest for the detection of 48.5 kbp lambda DNA translocations (0.1 ms∼10 ms).*

Then we turn to the study of the ionic noise properties in nanocavities, which is of particular importance to the signal-to-noise ratio (SNR) of resistive pulse sensing. Current flow through solid-state nanopores often exhibits a noise characteristic as a sum of flicker noise, thermal noise, dielectric noise and capacitive noise arising from dissipation of energy in non-ideal capacitance in the system.

Here we conduct noise measurements of all the three gold nanocavities (#2, #4 and #6) in Figure 3.1. The noise spectra of devices #2 and #4 are illustrated in Figure 3.4a. The power spectral density of gold nanocavity (#2 in black) exhibits very high flicker noise, which is due to the lack of dielectric noise [106, 131]. Since we use a 10 kHz low-pass filter, the power density above 10k Hz dramatically drops. The spectrum of gold nancavity with backside SiN (#4) is illustrated in red. The low frequency noise is much suppressed (>100 folds). We can also observe a pronounced dielectric noise component in the frequency region above 100 Hz, which is consistent with the noise spectra of metallized SiN nanopores [106]. This spectrum can be well explained as the sum of flicker noise, thermal noise and dielectric noise, showing that the noise properties match the state-of-the-art. For the thermal oxide as the passivation layer of device #6 in Figure 3.4b, we obtain a similar result to that of device #4. The dielectric noise component slightly shifts to higher frequencies, which may be attributed to the thicker dielectric layer (∼154 nm on device #4) than that of device #2 of 50 nm. Strictly speaking, compared to the state-of-the-art of SiN solid-state nanopores [118, 74], our devices #2 and #4 still have 2-10 folds higher flicker noise. However, we will show later that we are able to detect DNA events at our present noise level.

3.4 DNA translocations

Finally, we focus on the test of the feasibility for stochastic sensing of single molecules. The concept of translocating DNA through solid-state nanopore has been widely used to investigate charged biopolymers [28], intramolecular interactions [138] and molecule-nanopore interactions [139]. The DNA-nanopore interactions, containing pore properties such as surface charges [140], hydrophilicity [34, 35], and specific absorptions [32], can be reflected in the duration time of each event. For example, double-stranded lambda-DNA (48.5 kbp) has been characterized with the translocation time of 1.72±0.29 ms at 1M KCl in Figure 2.9c [120], which typically benchmarks the performance of DNA events through SiN nanopores.

Figure 3.5 conducts the ionic current of long-strand DNA translocations through metallic nanocavities #2. As illustrated in the inset, the chip separates the electrolyte into two chambers during the measurements. The negatively charged 48.5 kbp DNA were added to the chamber facing the narrower side of the the nanocavity. We applied positive bias to enable the transport of molecules from

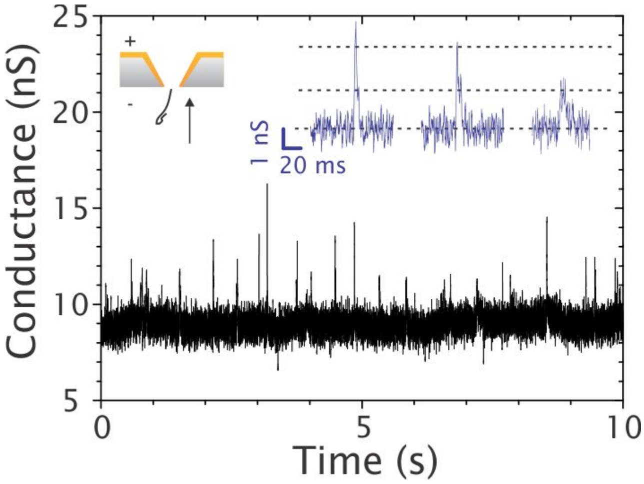

Figure 3.5: 48.5 kbp DNA translocation through a gold nanocavity. The time trace was recorded at +600 mV, 1 M KCl, 10 mM Tris-HCl and 1 mM EDTA buffer. The inset present the typical events through this device with 20 ms duration time. The traces are filtered at 2 kHz.

the bottom reservoir to the top one. The gold layer was floating during the experiment. Figure 3.5 shows the example of DNA events at +600 mV.

For translocation events, we observe increased pulses from the baseline. The behavior of conductance increase differs from that of the resistive blockades for the DNA transport at 1 M KCl which has been well studied for the state-of-the-art SiN nanopores. Although the conductance increase also exists on SiN pores due to the competition between DNA resistive blockade of the pore volume and the surface conductivity of DNA molecules, it only occurs at low salts (i.e. 0.1 M KCl) for SiN pores. However, these explanations cannot simply be applied to our observations of the conductance increase at 1 M KCl on gold nanocavities. This phenomenon of conductance increase at 1 M KCl is further confirmed on the titanium coated nanocavities as well. There are currently several hypotheses for the current elevation. One scheme could be based on the highly charged gold surface. The surface charge density of DNA can be treated as -75 mC/m_2 for pH=8.0, the value of which is much higher than that of SiN (-49 mC/m_2) but much lower than that of gold (-350 mC/m_2). This could lead to low ion concentration inside the gold nanocavity. DNA molecules when entering into the cavity, may have a smaller current blockade than their surface conductivity, therefore lead to current increase in this case. The second likely reasoning the depletion of local salt concentration inside the metal cavity [136] due to the free electron inside the gold layer, and then in a localized relative low salt region, the translocation of DNA becomes much more conductive [141]. The third hypothesis could be a collaborative process between DNA transport and a reaction (charge transfer). Although we can get a stable baseline without adding the DNA and the reactions at the gold interface themselves could not account for the effects, we need further studies to verify the mechanisms.

The inset shows the examples of DNA events at one or two levels which are approximately the same current increase level. This can be explained by the fact of the folds of DNA molecules [106, 142] and both of the unfolded and folded events can lead to current increase.

The typical duration time for “up” events is around 20 ms, which becomes much slower than the state-of-the-art 1.72±0.29 ms. Long dwelling time has also been found on metal-dielectric hybrid nanopores [106, 130], which was attributed to the absorption of DNA molecules onto the metallic surfaces. To validate this phenomenon in our experimental conditions, we confirm that the unspecific bindings of the DNA molecules exist on planar gold surface, measured by the shift of surface plasmon resonance (SPR). The device #4 and #6 cannot improve the translocation time since the gold layer still can interact with DNA molecule inside the nanocavity.

The study of DNA translocations paves the way to electrically record DNA events through gold nanocavities. However, different from the performance of the conventional SiN nanopores, the introduction of gold layer inside the nanocavity leads to conductance increases and long passage-times of the events. The plausible reasons could be the depletion of ion concentration and the strong absorption of DNA onto the gold surfaces, which increase the complexity of the ionic detection.

3.5 Conclusions

Our benchmarking of metallic nanocavities reveals the nature of variant device performances. First, nanocavity devices all showed linear I-V responses. Without coating the gold layer, the conductivity behavior of the nanocavity can be described by conventional fixed charged model. However, we found higher conductivity on all gold nanocavities and showed that the conventional fixed surface charge model did not apply. This is likely attributed to excess free charges, induced surface charges and related electron transfer on the gold-electrolyte interfaces. Second, the reduction of flicker noise and the appearance of dielectric noise have been found to be dependent on the introduction of SiN layer beneath a nanocavity or thermal oxidization of a silicon nanocavity. Third, the demonstrated DNA translocation experiments show distinguished current deviation and long passage time at high salts, which could be attributed to the ion depletion and strong interactions between DNA and gold interfaces. Nanocavities with a gold layer on top are difficult to become ideal devices, such as the state-of-the-art dielectric nanopores. Although we can successfully reduce the noise to a level which is close to the state-of-the-art by adding more dielectric materials, there are still bushes on the path towards regular salt-dependent conductivity and smooth DNA translocations.

Chapter 4

Characterization of metallic nanocavities with plasmonic excitation

In this chapter, we investigate the ionic properties changes of gold nanocavities upon laser illumination. Based on the non-ideal ionic performance of gold nanocavities shown in Chapter 3, we expect that the ionic study upon the excitation of surface plasmon in the following sections could provide more information towards a better understanding of the ionic behaviors.

4.1 Introduction

On one hand, a profound understanding of the noise sources within the nanopore systems is of paramount importance. The noise properties of ion transport through nano-sized pores or channels have been thoroughly investigated before [143, 117, 144, 145, 146, 147, 148, 149, 118]. However, not all reports point in the same direction. For instance, the origin of the flicker noise measured on a single dielectric nanopore is attributed either to cooperative effect on ions motion [147] or to the fluctuation of pore wall charges [117, 145, 149]. Knowing the exact noise sources also allows us to minimize the noise in experimental conditions. For instance, the experience with polydimethylsiloxane (PDMS) coated pipettes in single channel patch clamp has been transferred to the nanopore field, where the use of passivation layers is now a widespread technique to achieve low noise characteristics [143]. Similarly, the use of a SiO_2 protection layer or spacer can further eliminate the ionic noise and improve the dynamic performance by means of capacitance reduction [150, 74]. To further interpret our metallic nanocavity system, we will present the current noise changes upon laser illumination in section 4.2.

On the other hand, in nanofluidic systems containing solid-state nanopores, it is important to understand well the local potential distribution. However, it is challenging to verify the local potential experimentally. Solid-state nanopores integrated with metallic elements have been extensively applied to investigate localized physical or chemical processes [151, 152]. For example, tunneling current through electrode pairs [64, 153] and biasing a gate electrode [154, 155, 156] for molecular sensing and control have drawn considerable attentions. In contrary to electrode-like applications, optical nanostructures based on transmission [152], fluorescence [157] or surface enhanced Raman spectroscopies [87] have been demonstrated to provide additional detection and/or control capabilities. For these optical sensing techniques, metal layers are usually featured as unbiased (so-called floating electrode mode). But metals may also induce some issues as a consequence of high resistance of the nanopores. The applied potential can efficiently drop across the metallized membranes. For macroscale fluidics, sufficient potential difference between the floating metal layer and the solution is able to drive both oxidation and reduction reactions [158, 159], which probably also applies at the nanoscale. However, the local potential and electrochemical effects on the floating metal nanopores remain unknown. We will show how to probe the local potential and electrochemical reaction at the tip of a gold nanocavity in section 4.3, which could not be easily observed by means of the conventional ionic current.

4.2 Plasmonic induced ionic noise

Recently, we have been developing a strategy that combines SERS with conventional nanopore ionic fluidics (see Figure 4.1). This strategy makes use of the localized field enhancement in metallic nanopores or nanoslits, upon resonant surface plasmon excitation, which lead to additional nanoscale optical interrogation and manipulation of mechanically confined molecules and/or nano-objects. This strong and highly localized field enhancement enables the generation of SERS from the mechanically confined analytes inside the gap. In these cavities, the incident light can resonantly generate surface plasmons (SPP), which, depending on the length of the cavity sidewalls and the wavelength of the light, lead to strong field enhancements [89]. In Dr. Chen's PhD thesis [89], we also showed that these strong field enhancements are even further increased by

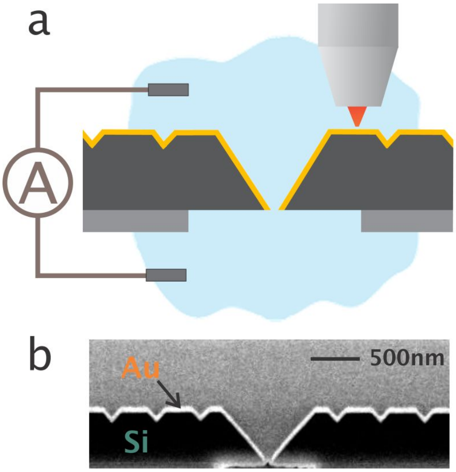

Figure 4.1: (a) Schematic drawing of the mapping of the root-means-square (RMS) current inside a nanoslit-cavity equipped with Bragg mirror gratings. The ionic current is measured during laser illumination in a scanning mode. (b) Cross-section SEM image of nanoslit cavity equipped with Bragg mirror antenna coated with a 100 nm Au layer.

adding an additional Bragg mirror at either side of the cavity. In this section, we examine the ionic currents through such a nanoslit upon light irradiation and we show that resonant excitation of surface plasmons in this nanostructure induces a strong additional noise component. We used the experimental protocol 2, which has been described in section 2.2.

Harnessing plasmon induced ionic noise in metallic nanopores

The results of this section were published in Nano Letters in the paper "Harnessing plasmon induced ionic noise in metallic nanopores" [131].

We measured the ionic current in function of time (plotted in Figure 4.2) and monitored both the mean current and the root-mean-square (RMS) value of the noise with and without laser excitation (1 mW focused on the nanocavity, with a wavelength of 633 nm). It is clear from Figure 4.2a, that the amplitude of the current noise immediately increased upon laser irradiation. The sudden laser irradiation change was accompanied by an initial current spike. The mean current increased with 0.15 nA, while the RMS of the current went up from 0.64 nA to 12 nA (shown in Figure 4.2b and c). When turning off the laser,

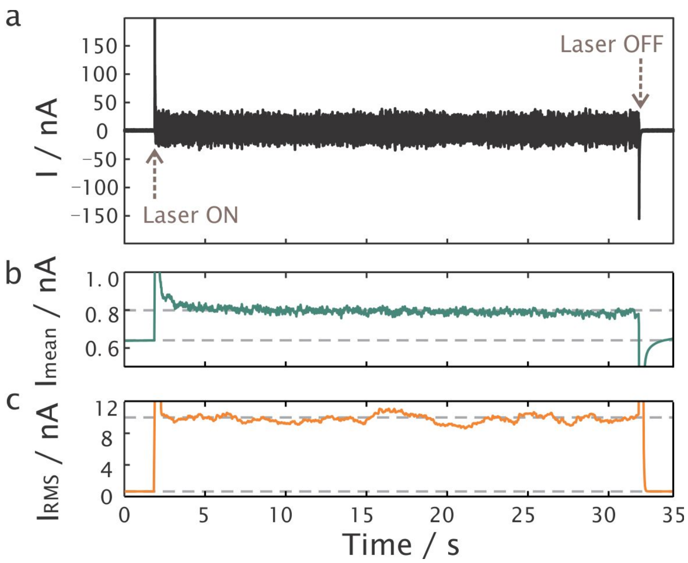

Figure 4.2: The ionic current profile in function of time with (a) the current signal upon 1 mW of 633 nm laser irradiation; (b) the mean current and (c) the root mean square of the ionic current.

both mean current and RMS current noise fell back to their original levels after discharging.

To study this effect in more detail, the ionic noise power spectral densities (PSD) before, during and after 1 mW of 633 nm laser illumination are plotted in Figure 4.3. Indeed, comparing Figure 4.3a,c, the noise spectrum returned to its former level after the laser is turned off. The noise spectrum without laser can be well explained as the sum of flicker noise, thermal noise, shot noise, dielectric noise and output voltage-noise caused by capacitance [74]. Upon irradiation with 1 mW 633 nm laser light, a completely different PSD was observed (shown in Figure 4.3b). The morphology of the PSD with a laser radiation at 633 nm was in fact only comparable to the reported PSD of ionic current oscillations through a single conical nanopore upon the formation of $CaHPO_4$ nanoprecipitates [160]. The observed unknown type of noise could be coarsely fitted with Lorentzian components,

$$S_L(f) = \sum_i \frac{S_i}{1 + (\frac{f}{f_{c,i}})^2} \tag{4.1}$$

where $S_L(f)$ is the power spectral density, S_i is the plateau power density (at 0 Hz) and $f_{c,i}$ is the corner frequency for the i_{th} single Lorentzian model.

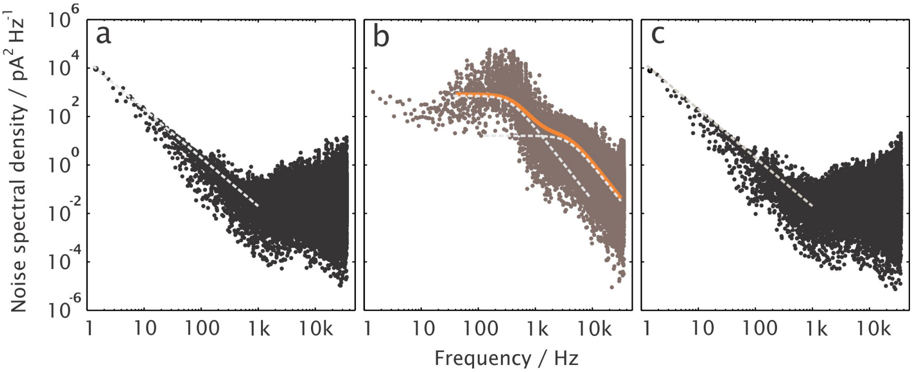

Figure 4.3: Noise power density spectra at 1 s, 15 s and 33 s of Figure 4.2a. (a) Before 633 nm laser illumination; (b) Illumination at 633 nm at the steady state; (c) After switching off the laser. The dashed lines in a and c indicate the flicker or 1/f^α noise, where α=2. The orange curve in b is the sum of two Lorentzian components (sum of the two dashed lines).

Two components are configured in Figure 4.3b. The corner frequencies are located at 400 Hz and 4 kHz, and the Lorentzian plateau at 800 and 20 pA^2/Hz, respectively.

Because the noise can be triggered by laser illumination, and the metal-coated nanopore structures support surface plasmon resonances, we investigated whether the increased noise was related to the excitation of surface plasmons by spatial and spectral mapping experiments. The combination of the weakly wavelength-independent nanoslit-cavity and the highly wavelength-dependent gratings [89] allow to understand the relationship between the SPPs excitation and noise generation by studying the wavelength-dependency and the polarization.

As can be seen from Figure 4.4b-d, the RMS current noise highly depended on the location, the polarization and the wavelength of the excitation. When the laser polarization was aligned parallel to the long axis of the nanoslit, an I_{RMS} of only around 2 nA was observed in Figure 4.4b. For the transverse polarization, however, the I_{RMS} was as high as 14 nA upon excitation at the center of the structure (see Figure 4.4c). The observation of the polarization dependence is consistent with our previous work and strongly supports the role of surface plasmons in enhancing the noise [89, 161]. The limited increase in for both the gratings and the flat gold surface (see Figure 4.4b) confirmed that the gold layer was thick enough to block the incident laser penetration into the silicon.

To shed some extra light on the origin of the effect, we also performed the spatial mapping of the noise for two different wavelengths, that is, 633 and 785 nm. These spatial maps are shown in Figure 4.4c,d. While the highest noise was observed for 633 nm (Figure 4.4c), the observed spatial distribution was clearly diverse for the two wavelengths. At an excitation of 633 nm, the induced noise was exclusively observed at the location of the nanoslit, while for 785 nm (Figure 4.4d) the gratings exhibit a significant contribution as well. Interestingly, when focusing on the grating area in Figure 4.4d, the PSD was the same as that of Figure 4.3b. This likely means that the SPPs propagating into the nanoslit cavity and the cavity plasmon generate the same type noise. Also these results are consistent with the role of surface plasmons as the cavity is relatively broadband, while the gratings are only resonantly excited in a narrow spectral range around 785 nm.

The strong dependency of ionic noise on the plasmonic properties of both the structure and incident light suggests that the noise is strongly related to the SPPs leakage into the silicon supporting layer at the electrolyte interface. The origin of the noise can be related to local physical and/or chemical processes occurring near the metal nanoslit. To further explain the additional noise induced by the plasmons, different potential causes, namely heating or photocatalysis, were examined in more details.

In order to examine the light-induced heat generation further, the thermal response of our nanoslit cavity was simulated using the method described in section 2.3 [162, 163]. On the basis of these simulations, focusing a 1 mW laser with a wavelength of 633 nm laser onto our nanoslit cavity, a maximum temperature increase of 1.5 K is to be expected. Besides as noted before, plasmonic induced heating is expected as being relatively homogeneous over the entire structure [164, 165] and should rise linearly with the power. The latter was also observed for the simulation data for both 633 nm and 785 nm wavelength as shown in Figure 4.5, with the slope of a 633 nm laser almost triple as high as for a 785 nm laser with a similar power.

Although theoretically possible, plasmonic heating is unlikely to be the predominant source of the enhanced noise as this should become clear from the noise power spectral density. From the conventional noise sources, Johnson (thermal) noise and dielectric noise are the only two sources that are temperature dependent. Johnson noise linearly depends on the temperature.$S_{thermal} = 4kT/R$, where k is the Boltzmann's constant, T is the temperature (here T=300 K), R is the resistance of the nanopore. The resistance in our case was 11.6 MΩ, leading to a rise of 7.14×10^{-6} $\mathrm{pA}^2/\mathrm{Hz}$ at 1 mW 633 nm wavelength. Furthermore, Johnson noise is white noise, which density is equally distributed in the entire frequency domain. It also means that Johnson noise can be eliminated as the source of the observed RMS noise current increase since the

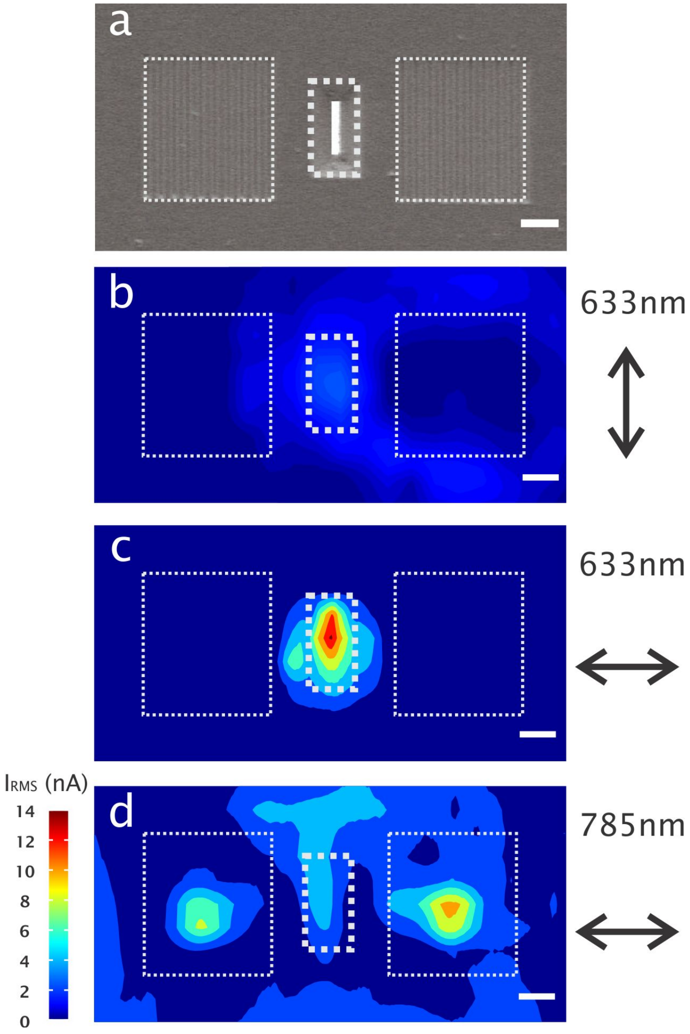

Figure 4.4: The ionic RMS current noise based mapping. (a) Top view scanning electron microscope image of the plasmonic nanostructure. The dashed rectangular at the center indicates the position of the nanoslit cavity, while the two dashed squares represent the grating couplers, optimized for 785 nm wavelength. (b) 633 nm laser illumination with polarization perpendicular to the transverse axis, (c) 633 nm laser illumination with polarization perpendicular to the longitudinal axis, (d) 785 nm laser with polarization perpendicular to the longitudinal axis. 1 mW laser power is used. Double-sided arrows indicate the polarization direction. The scale bar is 1 μm.

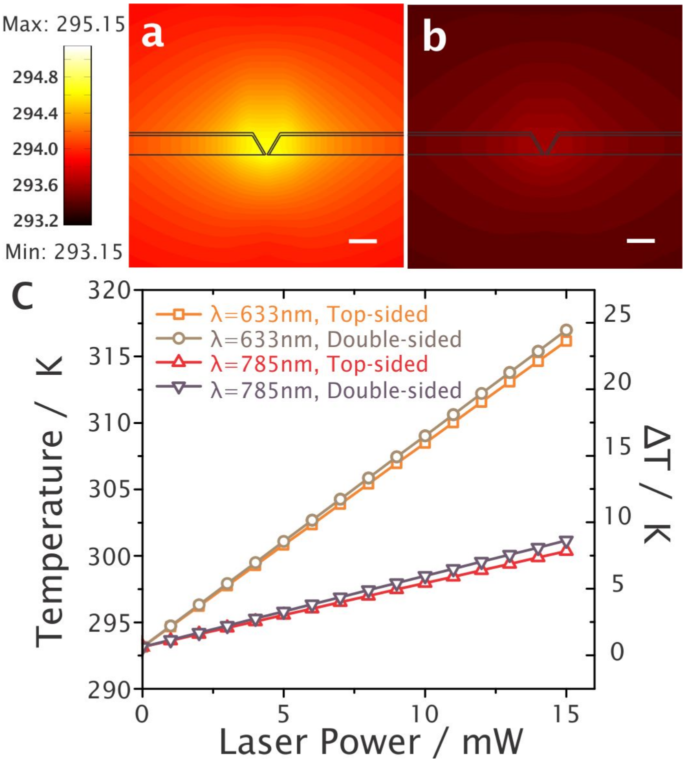

Figure 4.5: Numerical simulation of plasmonic heating induced by laser irradiation. (a,b) The cross-section view of nanoslit thermal profiles, respectively at 633 nm and 785 nm. The black lines define the top-sided gold nanoslit. The scale bar is 1 µm. (c) The temperature increase versus laser power. The ambient temperature is set as 293.15 K.

intensity and morphology do not correspond to the measured PSD. Secondly, dielectric noise generated by means of energy dissipation, giving an expression $S_{dielectric} = 8\pi k_B T D C f$, where D is the dissipation factor and C is the capacitance of the membrane, is linearly dependent on both frequency and temperature, resulting in a slope of 1 in the PSD. Therefore, dielectric noise can be canceled due to the differences on the noise morphology. Plasmonic heating cannot directly contribute to the conventional sources. Such a low increase in temperature can indeed not explain the large noise increase observed. Therefore, all of the conventional noise sources can be excluded due to their morphology of noise spectral density.

Besides light-induced heating, it is known that surface plasmons can also

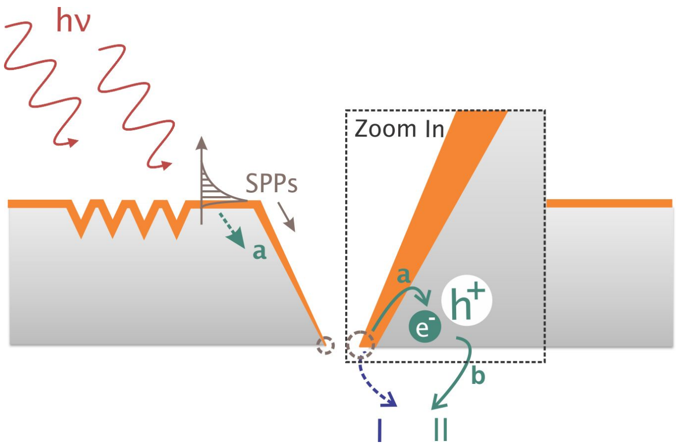

Figure 4.6: Two possible contributions of plasmonic induced ionic noises: (I) Direct plasmon induced photocatalysis on the metal surface (purple dashed curve); (II) Two-step plasmon induced semiconductor photocatalysis (green curves). The SPPs leakage generates electron hole pairs into the silicon (a), allowing for the electrochemical reactions at the interface (b).

accelerate catalytic effects (plasmon enhanced photocatalysis), which can play a role here. For a plasmonic photocatalyst system, the four major energy-transfer mechanisms [166, 167] are (1) plasmonic heating, (2) hot electron transfer, (3) near-field electromagnetic enhancement, and (4) resonant photon scattering. On one hand, the excitation of surface plasmons may induce the formation of hot electrons, which have energies that are sufficient to initiate electrochemical reactions at the Au/electrolyte interface. For example, transient ions can rapidly react as an electron-scatter process, and induce a subsequently reaction on the metal surface [168].

On the other hand, the Au film that supports the surface plasmons is deposited on a silicon substrate for which it is known that electron-hole pairs can be generated upon illumination with visible light. Although the silicon substrate is shielded by the 100 nm thick Au film, light can leak into the silicon substrate in two ways (shown in Figure 4.6). First, as the silicon substrate has a much higher index than the water on top of the metal film, the plasmons can leak directly to modes in the silicon substrate. Second, at the bottom of the nanoslit, near the hot spot, the top of the metal film is in direct contact with the silicon, giving a direct leakage path. The excited electron-hole pairs in the silicon can generate electrochemical reactions at the silicon/electrolyte surface. Although this pathway has more barriers to overcome, the result from noise measurement of polysilicon emitter bipolar transistors supports that a Lorentzian feature exists from 8 Hz to 10 kHz [169].

In order to prove which of these two pathways of plasmon induced photocatalysis is responsible for the RMS current noise increase under laser illumination, a 10 nm/20 nm layer of titanium/gold was deposited on the backside of the nanocavity. This removed a direct interaction between silicon and the electrolyte solution, while the optical properties, hence SPPs properties, of the structures were quite comparable. The effect of the near field EM enhancement can be excluded out both from simulation and experimental results [84]. The ionic current noise as a function of 633 nm laser power is shown in Figure 4.7.

In Figure 4.7, it is clear that coating the backside strongly inhibits the noise generation (with the slope of -3 pA/mW). I_{RMS} after backside passivation stays more or less constant with optical power at 138 pA. The current noise of topside coated device goes saturated at 52.96 nA. As the simulations show that the local field enhancement and the plasmon induced heating do not change significantly upon coating of the backside, we can attribute the additional noise to the plasmon-induced catalysis at the silicon/electrolyte interface. The intrinsic property of silicon matches the requirement of two electrochemical reactions, hydrogen production [170] and oxygen decomposition [171] in an aqueous environment.

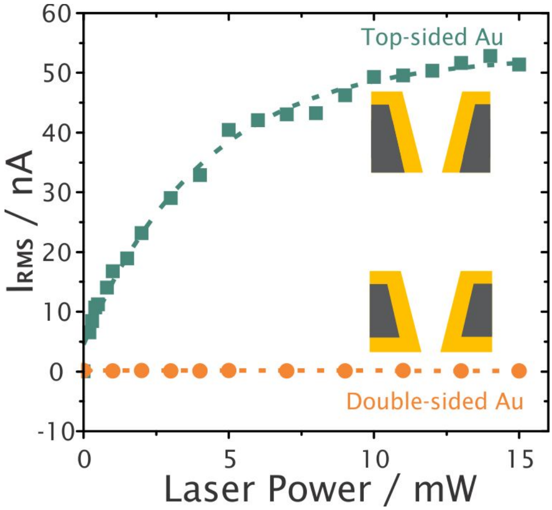

Figure 4.7: Ionic RMS current properties as a function of 633 nm laser power for both devices. Top-sided gold device are labeled in green square and double-sided gold device in orange circle.

Voltage-dependent plasmonic induced ionic noise in metallic nanopores

In this section, we will show another denoising method upon laser illumination. Since the noise source upon plasmonic excitation has pointed toward the presence of silicon, it would be a crucial step to block the noise generation at the interface. Instead of coating all the boundaries with gold, we characterize the devices with dielectric materials on the backside of silicon nanocavities: device #4 - gold nanocavitiy with backside SiN and device #6 - gold coated thermally oxidized nanocavity (illustrated in Figure 4.8a,b).

The scheme of the experiment is shown in Figure 4.8c. To avoid the overflow of current amplifier, 10 mM KNO_3 was used instead of 1 M KNO_3 in the voltage window between -1000 mV and +1000 mV. The values of RMS current noise are processed with a band-pass filter from 50 Hz to 1k Hz to get rid of the interference from 1/f noise and high frequency noise. In Figure 4.8a, we obtain relatively stable ionic currents at different bias voltages without laser illumination. The noise becomes evident at the voltage lower than -600 mV using 785 nm wavelength laser at 0.5 mW. While the RMS noise monotonically

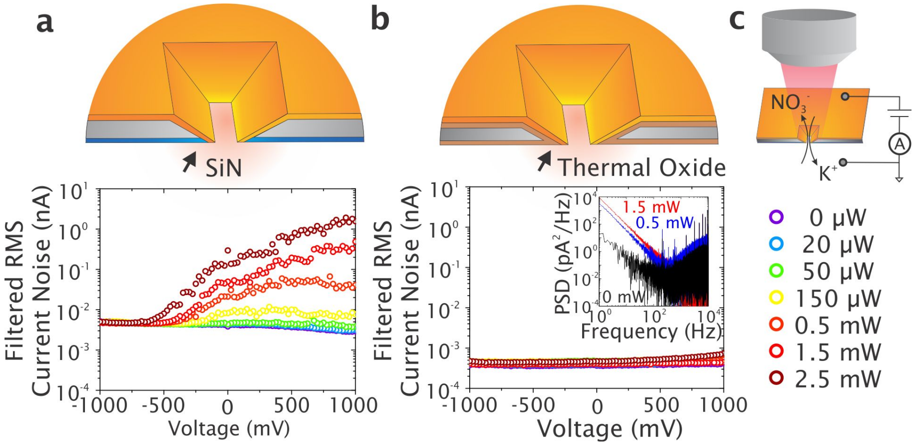

Figure 4.8: RMS current noise of gold nanocavities with backside passivation. (a) Ionic noise versus bias voltage on device #4 - gold nanocavity with 50 nm PECVD Si_3N_4 on the backside. (b) Ionic noise versus bias voltage on device #6 - gold coated thermally oxidized nanocavity (Thermal SiO_2 is about 77 nm thick). The inset shows the noise spectra at 0 mW (black), 0.5 mW (red) and 1.5 mW (blue). The band-pass filter was set from 50 Hz to 1k Hz. (c) Schematic representation of the experimental geometry upon laser illumination.

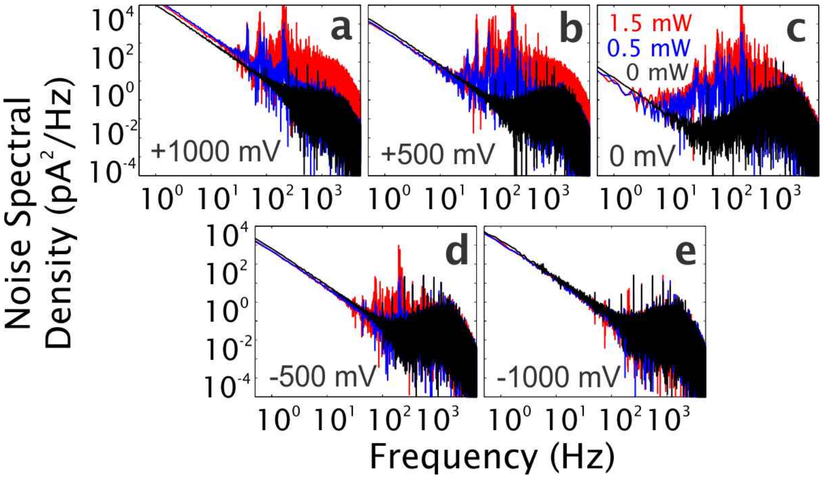

Figure 4.9: Noise power spectral density at 0 mW (black), 0.5 mW (blue) and 1.5 mW (red) for (a) +1000 mV; (b) +500 mV; (c) 0 mW; (d) -500 mV and (e) -1000 mV. The low-pass filter is set at 2k Hz.

depends on bias voltage, the threshold of noise increase shifts to more negative bias when the laser power increases. In contrast, the RMS noise of thermally oxidized chip in Figure 4.8b is almost constant with the bias voltages and is at a relatively low noise level. Although the inset of noise spectra exhibits a 1/f noise increase upon laser illumination, the Lorentzian component clearly disappears.

To understand the voltage-dependent ionic noise in Figure 4.8a, we plot the noise power spectral densities of the device #4 at 5 different biases, which are shown in Figure 4.9. First, Lorentzian components in this figure are still observable and share similar morphology with that in Figure 4.3b. However, there is still a slight frequency difference, which could be attributed to the existence of Si_3N_4 layer and a much lower salt concentration (from 1 M to 10 mM KNO_3) used in this case. Second, the Lorentzian components upon 0.5 mW and 1.5 mW of laser power gradually decrease when the bias goes to the negative and completely disappear at -1000 mV. We note that the 1/f noise is modulated with bias voltage, which is in a good agreement with on SiN nanopores [117, 147] and ultra-thin graphene pores [172].

Comparing these two types of devices #4 and #6, we are able to reduce the plasmonic induced ionic noise in two different manners. On one hand, coating the backside of the nanocavity with SiN can largely diminish the noise. The voltage dependent characteristics of PECVD allow us to operate at some negative bias, which is already a step closer aiming for a perfect device. However, the noise increase can still be observed upon laser illumination at positive bias due to the defects, dangling bonds or pinholes through the Si_3N_4 layer. On the other hand, we show that thermally oxidized nanocavity can not only provide a lower noise level without laser illumination, but also totally prevent the generation of Lorentzian components. This provides us a practical solution to use a single-step CMOS-compatible process to improve our device performance.

Moreover, the strong noise modulation as a function of bias voltage suggests a voltage-threshold for the interfacial reactions. Although hydrogen gas can indeed be produced from Si in water when illuminated [173, 174], the photocatalysis of water on a silicon surface has recently been found not to be a complete water-splitting process [175], since the formation of Si-OH bonds results in the low probability of generating oxygen gas [175]. Both Si-H and Si-OH dangling bonds extract photoexcited electrons, greatly increasing the ionic noise into our ion flow. In addition, the negative shift with increased laser power indicates a co-operational process between the external potential and the generated photovoltaic potential. The optical transparency and photon energy (2.54 eV) of the Si_3N_4 can facilitate the generation of electron-hole pair in the Si substrate (band gap $\sim$1.1 eV), which has been reported to promote photoreduction of H^+ at p-type Si interfaces [176]. The noise measurements enable us to come up with a much more sensitive method to characterize the photoelectrochemical process.

4.3 Probing local potential inside metallic nanocavities with SERS

In this section, we use SERS to probe the local potential inside the metallic nanopores. First, we provide the results of numerical simulation which indicate the bipolar electrochemical effects on both double-sided gold (MM) nanopores and top-sided gold nanopores with backside Si_3N_4 (MD nanopores). Distinct local potential distributions are illustrated between the two types of metallic nanopores. Then, we utilize the bipolar electrochemistry and electrochemical active surface enhanced Raman spectroscopy (EC-SERS) to show the potential-dependent SERS processes inside the metallic nanopores.

The concept of bipolar electrochemistry and SERS. Since the 1970s [159], electrochemical reactivity at *floating metal extremities* (named “bipolar electrochemistry”) [177] has been reported on a number of fundamental studies and applications [177]. Rather than directly applying potential difference between two metal electrodes, bipolar electrochemistry builds a very strong

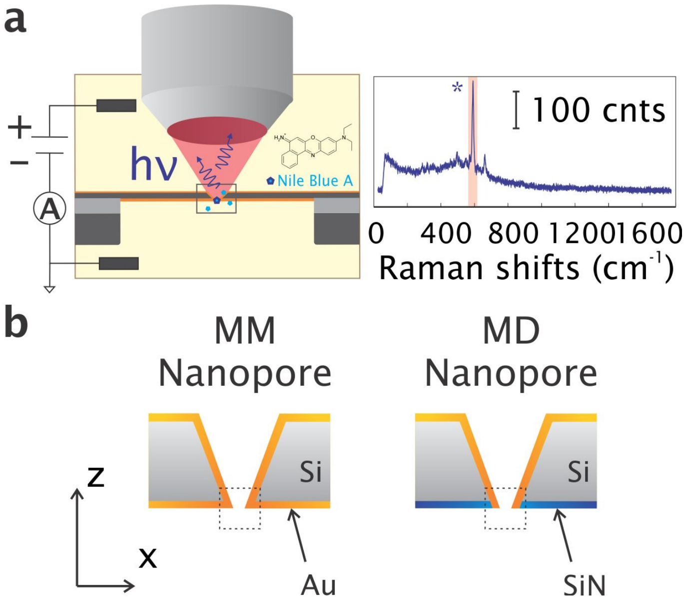

Figure 4.10: Surface enhanced Raman spectroscopy in single gold nanopores. (a) The schematic drawing of nanopore bipolar electrochemistry experiments: Ag/AgCl electrodes are placed at top and bottom reservoirs to build a potential difference, while excitation and Raman scattering photons are collected by the same 60× water immersion objective in a confocal microscope. 10^{-5} M Nile Blue A molecules (in blue) are dispersed in the electrolyte, acting as electrochemical active Raman probes. The fingerprint peaks at 594.8 cm^{-1} mode are labeled with an asterisk. (b) double-sided gold (MM) nanopores and top-sided gold nanopores with backside Si_3N_4 (MD) nanopores.

electric field and keeps the metal floating, the mechanism of which is based on the polarization of conducting objects in the electric field. To characterize bipolar electrochemical effects, optical readouts including electrochemiluminescence (ECL) [178], electrochemical corrosion microscopy [179], epifluoresence [180] and surface plasmon resonance spectroscopy [181] have been investigated to probe anodic and/or cathodic behaviors at metal/solution interface. However, restricted by optical resolutions, the two polarities of a floating electrode need to be placed far enough from each other. This requirement becomes more challenging for metallic nanopores. The two polarities are vertically located across the membrane, the distance of which can be 1∼2 micrometers [182] or as close as several nanometers [183].

Here, we suggest to use surface-enhanced Raman spectroscopy (SERS) to study localized bipolar effects. As an approach to support high spatial resolution [184] and high sensitivity for molecule identification, SERS has been widely used to probe the changing of molecules and ions for the interfacial reactions during electrochemical processes [185, 186, 187, 188, 189]. In principle, one should carefully select a SERS probe, the intensity of which can be modulated by electrochemistry: the oxidized/reduced form of the SERS probe produces extremely stronger SERS signals than the other reduced/oxidized form [190]. With localized SERS hot spots [184] aligning with fluidic focus, we are capable to be the first to probe the local potential and to characterize the nanoscaled bipolar electrochemical effects on the metallic nanopores.

Figure 4.10a depicts the scheme of the experiments with the metallic nanopores. These pores consist of a gold layer on top of a three-dimensional nanoslit cavity. The main device feature is the overlapping of a SERS detection region (called hot spot) with the electrochemical sensitive region in fluids [184]. To maximize the plasmonic response and subsequent SERS signal in our metallic nanopores, a gap size of 10 nm requires a nanocavity length of ∼100 nm. The processing details were described in section 2.1. We used the experimental protocol 3, which has been described in section 2.2. The nanopore chip was mounted into a custom-made flowcell and separated the electrolyte into two reservoirs. Next, the flow cell was placed onto our confocal Raman microscope and the metallic pore was aligned with the focal spot of our 785 nm excitation laser source. The electrical potential was applied to the side with the gold cavity, and the other side was connected to ground, which defines the applied bias direction for positive and negative values in the experiments. Since an appropriate electrochemical active Raman probe is extremely important for this experiment, we screened Nile Blue A (NBA) rather than molecules that form self-assembled monolayers (e.g. 4-aminothiophenol, 4-ATP). By monitoring hot spots through a 60× water immersion objective lens, we are able to obtain typical SERS spectra of NBA with a fingerprint peak at 594.8 cm^{-1}, corresponding to an electrochemical-active vibration mode.

Numerical simulation of the local electric field. To determine the local potential with SERS, we investigate the two types of metalized devices (shown in Figure 4.10b) with distinct polarity properties: doubled-sided gold nanopores (MM nanopores) and single-sided gold nanopores with a dielectric (e.g. silicon nitride, Si_3N_4) passivation layer on the backside (MD nanopores). As the applied electric field along the gold/electrolyte interfaces drives the bipolar electrochemical effects, we plot in Figure 4.11 the simulated profiles of electric field component in z direction E_z. A strong electric field locates at the center of MD nanopore channels, whereas the electric field intensity becomes much weaker for MM nanopores. For MM nanopores, the sign of E_z at +1 V (applied voltage) is negative, indicating that the gold holds a lower potential than the electrolyte near the hot spots, while the positive sign of E_z at -1 V results in a higher potential on the gold than the electrolyte. For MD nanopores, the two cases are just the opposite.

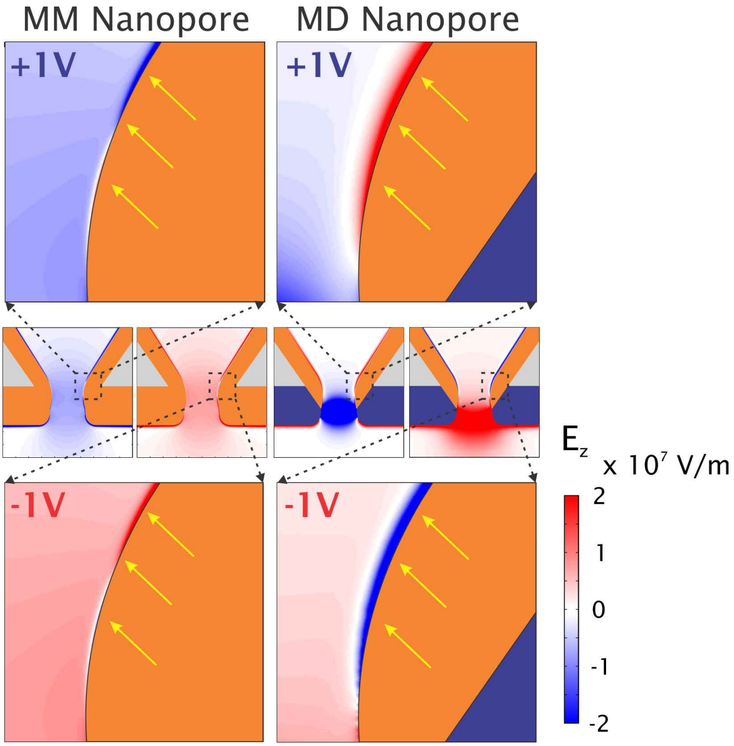

Figure 4.11: Simulated electric field profiles of X-Z plane. The inset shows the zoomed-in of 20×20 nm^2 area. Yellow arrows point toward to the surfaces of SERS hot spots on which the redox reactions of monitored NBA take place. The max and min values are limited to ±2×10^7 V/m for the visual convenience.

Electrochemical activity of the SERS probe. The sign of the electric field ought to be consistent with the modulation of SERS of NBA. Ni et al [190] studied the electrochemical SERS behavior based on NBA. The oxidized form of NBA produces much stronger SERS signals than the reduced form due to a proton-electron transfer reaction [190]. Our NBA molecules are verified in terms of Cyclic Voltammetry (CV). Figure 4.12a,b show the typical CV curves with the reduction and oxidation peaks. The redox potential at 10 mM Na_3PO_4, pH = 5.95) is around -0.35 V which is consistent with the reported value [185, 186]. Since we use 1 M KNO_3 at pH = 8.0 for the consistency of most nanopore experiments, the redox potential shifts to around -0.48 V (see Figure 4.12b). As

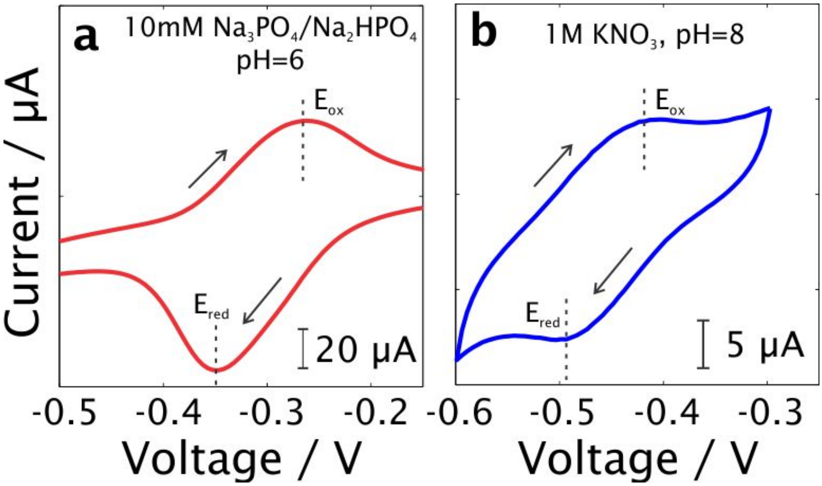

Figure 4.12: Cyclic voltammetry of Nile Blue A absorbed on gold surface in sodium phosphate buffer (pH≈6) in (a) and 1 M KNO_3, Tris-EDTA buffer (pH≈8) in (b). The arrows indicate the direction of the voltammetry. The reduction (E_{red}) and oxidation peak (E_{ox}) are marked with dashed lines.

a result, we would expect to observe a strong SERS when the applied voltage is above -0.48 V on MM nanopores, and the same phenomenon happens when the voltage is below +0.48 V on MD nanopores.

Probing local potential by EC-SERS. Figure 4.13 displays the integrated SERS intensities of the 594.8 cm^{-1} band at different bipolar driving voltages. First, the SERS intensity in the MM nanopore is enhanced with the increasing of voltage, while the intensity in the MD nanopore goes down. This voltage-dependent SERS behaviors confirm that bipolar electrochemical effects occur in our metallic nanopores. The distinguished SERS responses between the two devices are consistent with the numerical simulations in Figure 4.11. For MM nanopores, the increase of SERS intensity can be attributed to the bipolar electrochemical induced oxidation of the SERS probe (NBA), while the intensity decrease on MD nanopore implies the generation of reduced form. Bouchet et al demonstrated bipolar electrochemistry on dielectric interfaces, where the high intensity of the electric field can lead to the polarization of bulk dielectrics [191, 192, 193]. Their work opens up the possibility to utilize dielectric materials in bipolar electrochemistry. Our observations of the SERS reduction on MD nanopores can be explained by the polarization of both gold and Si_3N_4. Moreover, the results in Figure 4.13 are in agreement with our simulation in Figure 4.11. Second, the intensity changes of these two types of nanocavities are found to be axisymmetric at 0 V. The (absolute) voltage threshold locates

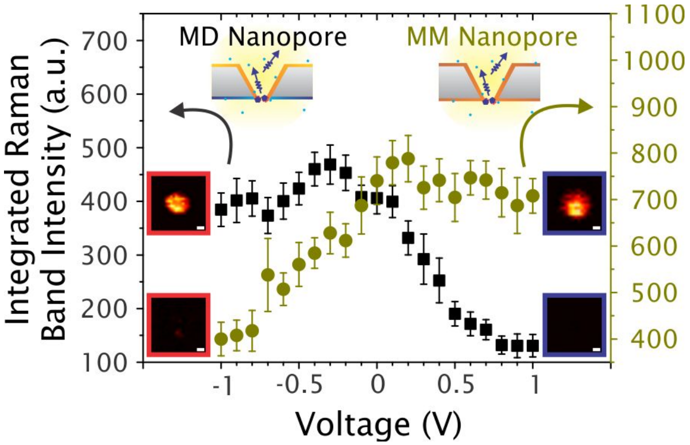

Figure 4.13: Integrated Raman band intensities at 594.8 cm^{-1} band are plotted as a function of applied voltage. Yellow dots illustrate the SERS intensities of double-sided gold nanopores, while black squares represent gold nanopores with backside Si_3N_4. The mean value and the error bar are derived from 50 spectra at each potential level. The blue and red inset are the X-Y plane SERS maps at +1 V and -1 V, respectively. The white scale bar is 1 μm.

at 0.7~0.8 V, higher than our prior expectation. The threshold of the bipolar driving potential is around 1.46-folds of the local redox potential, which is much lower than the value (usually >10 folds) in microfluidic channels with bipolar electrodes [179, 194].

SERS mappings at ±1 V show good performances on spatial distribution for bipolar electrochemical characterization. First, in line with the average SERS intensities, oxidized form NBA gives rise to high intensities at 594.8 cm^{-1}, locating in a spot with FWHM of 2~3 μm in Figure 4.13. The size is mainly due to the convolution of the beam size of the laser and the geometry of our nanocavity pore. Second, the SERS intensity can be diminished when the reduction of NBA occurs inside the nanopore. While the reduced forms yield little to no SERS signal inside the nanopore, the oxidized forms cannot contribute to a readable SERS due to the localization of oxidized forms out of the detection region (on the top of the cavity). Since the SERS modulation represents the bipolar electrochemical reactivity in one extreme of the two, the spatial resolution is highly localized at one pole but not two of the metallic nanopores.

An example of fluidic SERS manipulated by the local potential changes. Benefiting from the understanding of the local potential (bipolar

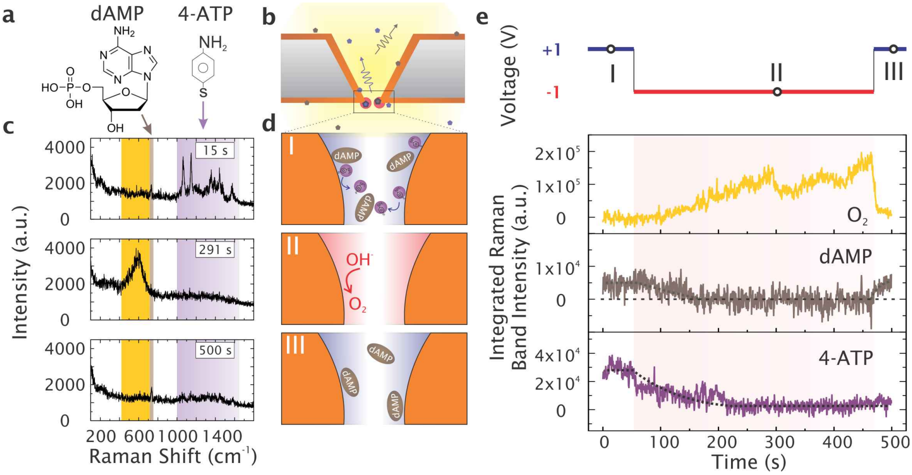

Figure 4.14: Bipolar electrochemical study of chemical replacements inside a single gold nanopore. (a) Molecular structures of 2'-Deoxyadenosine 5'-monophosphate (dAMP) and 4-Aminobenzenethiol (4-ATP). The arrows point from the molecule to the corresponding wavenumbers of SERS bands. (b) The schematics of MM nanopore. (c) SERS spectra at 15 s, 291 s and 500 s. The yellow window shows the Au-O stretching, the narrow brown window for dAMP and the purple window for 4-ATP. (d) Schematics of three stages (I, II and III) corresponding to panel c. Stage I represents that 4-ATP is coated on the gold surface and dAMP can get close to the interface. Stage II indicates the generation of Au-O stretch and the repelling of dAMP away from the interface. Stage III illustrates that the termination of Au-O stretch and dAMP can get back close to the interface. (e) The temporal applied voltage and integrated Raman band intensities. Yellow, brown and purple trances are the integrated band intensity of Au-O, dAMP and 4-ATP, of which the integrated area are defined in panel c. The dots on the voltage relate to the corresponding time stamps. The above three stages correspond to +1 V, -1 V and +1 V again.

electrochemical effects) inside our gold nanopores, we can further utilize it for fluidic SERS applications. Figure 4.14 shows an application of three-step electrochemical processes inside a gold nanopore channel. An MM nanopore was previously incubated with a self-assembled monolayer of 4-Aminobenzenethiol (4-ATP) and filled with 1 mM 2'-Deoxyadenosine 5'-monophosphate (dAMP) in 0.1 M KNO_3. The experimental details were refered to Protocol 3 in section 2.2. We switched the transmembrane voltage from +1 V to -1 V and later back to +1 V, dividing the whole process into three stages. The three SERS spectra corresponding to each stage are shown in Figure 4.14c and the related temporal traces are plotted in Figure 4.14e. At stage I at +1 V, the SERS spectrum at 15 s shows the peaks both for the dAMP and 4-ATP. The non-resonant dAMP only contributes to a weak peak at 731 cm^{-1} (in brown window), while the SERS peaks from 1000 cm^{-1} to 1700 cm^{-1} are mainly assigned to 4-ATP (in purple window). In this stage (scheme illustrated as stage I in Figure 4.14d), 4-ATPs are attached and dAMP can still get close (or even absorbed) to the gold surface.

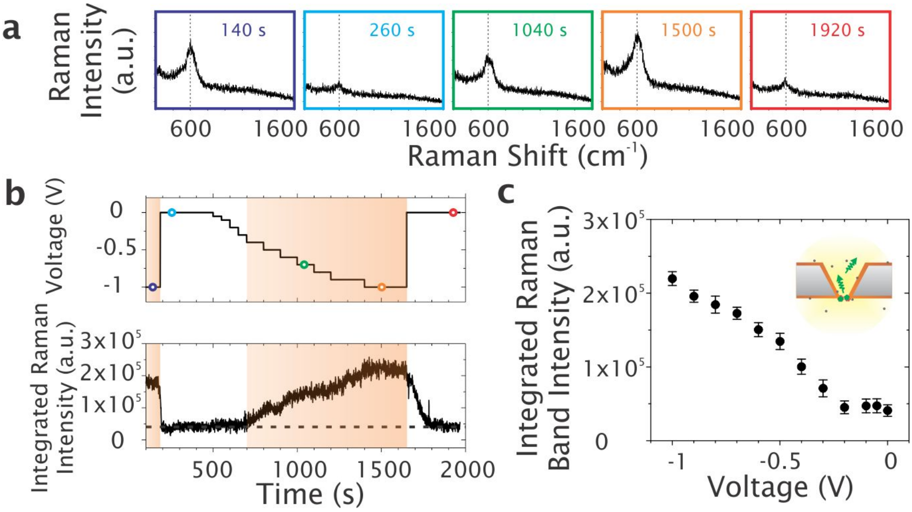

Figure 4.15: Oxygen evolution on nanopore SERS due to bipolar electrochemistry. (a) Five represented Raman spectra on 140 s, 260 s, 1040 s, 1500 s and 1920 s, respectively. The dashed lines show the 580 cm^{-1} Raman shift. (b) Temporal applied voltage and integrated Raman band intensity of 580 cm^{-1} peak. The dashed line presents the baseline of the Raman signal. The orange window indicates when the reaction occurs. Five colored dots are in corresponding to the spectra in (a). 0.1 M KNO_3 at pH 8 is used in this experiment. (c)The integrated intensity as a function of applied voltage.

When the trans-membrane voltage switches to -1 V at stage II, the local potential should be around -0.68 V. At 291 s, we observe the disappearance of the peaks of both 4-ATP and dAMP on the spectrum. Their intensities gradually decrease (shown in Figure 4.14e). This can be attributed to the electrochemical removal of the molecules: Thiol-functionalized molecules exhibit an electrochemical desorption at around -0.7 V [181, 195] where 4-ATP enables the release from the detect region. Besides, negatively charged dAMP molecules can be repelled from the gold surface at negative bias due to the electrostatic interactions. The peak of dAMP in Raman spectrum turns to be undetectable. Moreover, we also observe an unstable increase of 580 cm^{-1} band, which corresponds to the Au-O vibration mode [196, 197]. We further confirm the reaction potential of this peak mode at -0.3~0.4 V, which is quite close to the standard potential +0.4 V for the O_2 evolution. Figure 4.15 shows an example of the O_2 evolution.

Then we come to stage III, when the trans-membrane voltage turns back to +1 V. The intensity of Au-O band drops back to the original resting state. The 731 cm^{-1} mode for dAMP appears again, indicating that dAMP can freely reach onto the gold-electrolyte interfaces in this condition. However, the released monolayer of 4-ATP does not contribute peaks into the spectrum. It may diffuse far away out of the nanopore channel due to the extreme low bulk concentration of 4-ATP.

In summary, a bipolar electrochemical modulation of SERS has been investigated on single gold nanopores for the first time. Aligning electrochemical sensitive region with the fluid focus, SERS hot spots enable us to probe the local electrical potential of metallic nanopores. Moreover, we show the voltage dependencies both on MM nanopores and MD nanopores, which is supported by the numerical simulations. Benefiting from the tight confinement in the nanofluidic pore channel with surrounding metal, our devices also exhibit much lower driving voltage than microfluidic bipolar devices. The demonstrated SERS results of complex bipolar electrochemical activities can guide the design of nanofluidic chip and contribute to the applications on (bio-)chemical sensing [198], concentration and separation [199, 141], and wall functionalization [193] in the wireless and remote manners.

4.4 Conclusions

In this chapter, we have investigated the noise performances of plasmonic nanocavities upon laser illumination. Starting from gold sputtered silicon nanocavities, we reported ionic noise increase upon laser illumination, the noise source of which points toward the silicon-electrolyte interface but not the gold-electrolyte one. We proposed two distinct methods for noise reduction - to coat the backside of Si nanocavity with either metal or dielectric materials. On one hand, sputtering gold onto the backside of nanocavities can provide homogenous Au/H_2O interfaces and the similar electromagnetic field enhancement with top-coated gold nanocavities. The optical-excited charge carriers that reach the Si/H_2O interface can be blocked. On the other hand, for the passivation with thermal oxide, the high-quality SiO_2 can effectively block the generated electron-hole pairs from arriving at the electrolyte interfaces. Although the high-temperature oxidation process causes a morphology change of the sharp tip (see Figure 2.5d), we would like to highlight the importance of this process as one of necessary approaches towards simultaneous optical and ionic detection. Our work has aroused the attentions not only from the research groups on plasmonic nanopores [87, 200, 201, 202], but also from the semiconductor photocatalysis community [203, 204].

We have also reported the bipolar electrochemical reaction using SERS, which serves as a probe for the local potential inside individual metallic nanopores. We numerically and experimentally demonstrate two kinds of devices (double-sided gold nanopores and top-sided gold nanopores with backside Si_3N_4), showing the distinct local potential distributions between them. In the design of nanopore devices, different local potential behaviors should be taken into careful considerations. Our results also show the use of the electrochemical cleaning at the interfaces inside the metallic nanopores. Recently, dynamic metal growth [205] and the biosensing detection of insulin [206] extend the usage of the bipolar electrochemical mechanism inside the nanopores or nanochannels to various applications. Our method enables us to optically probe the local electrical potential, which not only provides valuable understandings on the design of the metallic nanopores, but also paves the way to wireless metalized nanofluidic devices [179, 194, 141, 207].

Chapter 5

Characterization of nanopore-in-cavity device without laser irradiation

In this chapter, we modify metallic nanocavities and try to establish a link between our nanocavities and the state-of-the art nanopores. Integrating a nanopore beneath a nanocavity as a novel device can provide the following advantages: first, electron beam can precisely control the pore location inside the gold nanocavity, and sculptured solid-state nanopores can heavily confine the fluidic transport. Second, the nanopore-in-cavity with the introduction of a SiN nanopore can provide a research platform which is comparable to that for conventional solid-state nanopores. Third, the nanopore-in-cavity platform with a dielectric membrane embracing the gold nanocavity can potentially avoid the strong DNA-gold interactions during DNA transport and provide great backside isolation for noise reduction.

An introduction to the concept of a novel device comprising of a solid-state nanopore inside a metallic nanocavity is first presented in section 5.1. Along with the process flow derived from section 2.1 and numerical simulation method in section 2.3, we illustrate how the devices will operate. In section 5.2-5.4, the link between gold nanocavities and nanopore-in-cavity are experimentally examined from the three aspects (already discussed in Chapter 3). Finally in the conclusion of section 5.5, we believe that a nanopore beneath gold nanocavities can pave the way for single molecule detections with high ionic performances.

5.1 Introduction

Solid-state nanopore integrated with a plasmonic nanoslit cavity

Ionic transport phenomena, especially at the nanoscale, are highly dominated by the interfaces that form the pore/cavity channels. Figure 5.1a illustrates the interface differences between a gold nanocavity and a solid-state nanopore inside a gold nanocavity. The interfaces interacting with ions and DNA changes from gold (red dashed line) to SiN (blue solid line). The fabrication of such pore-in-cavity devices has been discussed in section 2.1. Based on the development of nanocavities in Chapter 3, here we propose two kinds of devices: solid-state nanopore inside a SiN backside coated gold cavity, and solid-state nanopore inside gold-coated thermally-oxidized cavity. For the former one, we perform SiN depositions twice, once before and once after the gold sputtering. For the latter type of devices, a Si_3N_4 layer is deposited on the backside of the gold-coated thermally-oxidized nanocavities.

Figure 5.1b shows an example of the pore-in-cavity device with a double Si_3N_4 depositions. We drill single pores with a diameter of 10 nm, which is the typical dimension for DNA study.

Numerical simulation of nanopore-in-cavity devices.

To thoroughly understand the behavior differences among the conventional SiN pores, gold nanocavities and the pore-in-cavity devices, we perform the numerical simulations of electric field distributions for three different configurations using Comsol Multiphysics 4.3a. Figure 5.2 shows the results of the profiles. Here we compare among a conventional SiN nanopore (Figure 5.2a-c), a gold nanocavity (Figure 5.2d-f) and a SiN nanopore in a gold nanocavity (Figure 5.2g-i). We use the same diameter (d=10 nm) and membrane thickness (l=30 nm) of a SiN pore in Figure 5.2 a and g. The gold nanocavity with a width of 30 nm is identically configured in Figure 5.2 d and g.

The electric fields on lateral and vertical directions are shown in Figure 5.2 b,c. When a negative bias is applied to drive the negatively charged DNA through the pore, the lateral electric field is able to compel the DNA molecule away from the surface and the vertical electric field drags it toward the top reservoir. The highly concentrated electrostatic field suggests a smooth translocation process through the pore.

However, the electric field profiles for the gold nanocavity in Figure 5.2e,f are different from the previous ones. Due to the presence of metal, the redistribution

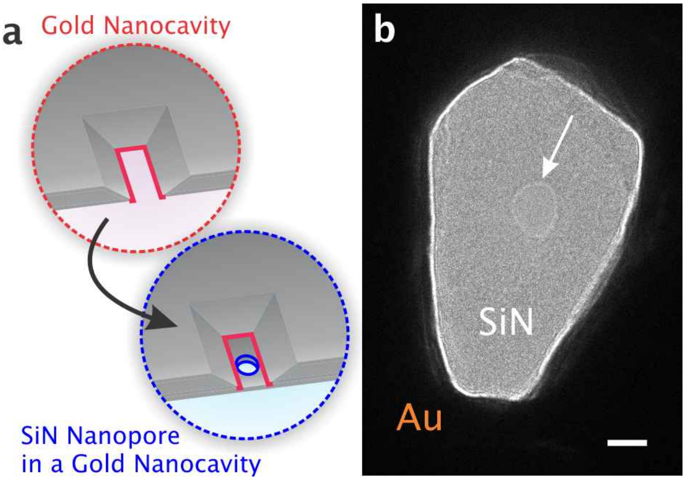

Figure 5.1: Different critical interfaces between a gold nanocavity and a solid-state nanopore inside a gold nanocavity. (a) Schematic presentation of the critical interfaces of the two devices. Red curves indicate the gold boundaries in contact with fluids, while the blue curves describe the SiN boundaries with fluids. (b) A TEM image of a non-ideal pore-in-cavity device. The geometry of the gold nanocavity does not form a rectangular shape. The arrow points to the position where the pore locates. The white bar is 10 nm.

of free charges occurs when the electric potential is biased. Although the total charges of a metal pore should be conserved, the charges with one sign (in Figure 5.2d are positive charges) could be induced and accumulated inside the pore following the electric field, while the opposite charges could be induced near the top surface of a gold cavity [136]. The induced charges can shield the metal region. Since induced positive charges can be accumulated inside the cavity, they attract the negatively charged DNA molecules both in lateral and vertical directions (see Figure 5.2e and f), which forms an electrostatic trap at the narrowest confinement of the nanocavity.

Figure 5.2h,i presents the electric field distributions of a pore-in-cavity device. Due to the introduction of the bottom Si_3N_4 pore, the electric fields both in lateral and vertical directions become similar to the standalone Si_3N_4 ones. Considering the transport of DNA from bottom to the top reservoir, the electrostatic field suggests a lateral repulsive force and a vertical drag force on DNA molecules. We note that the forces near the gold cavity surfaces maintain attractive.

The fabrication of these two kinds of pore-in-cavity devices (SiN deposition

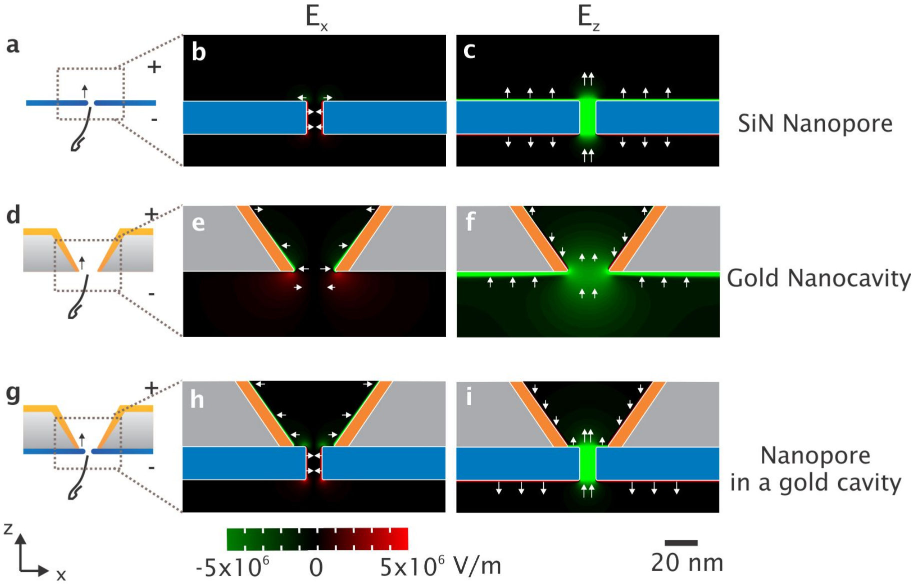

Figure 5.2: Numerical simulations of electric field (E_x and E_z) of three configurations at 1 M KCl. (a-c) The nanopore through conventional SiN membrane. (d-f) The gold nanocavity device. (g-i) The pore-in-cavity device. The materials of gold, silicon and SiN are marked in blue, orange and grey. The arrows indicate the force direction when a negatively charged DNA is present.

twice and thermally oxidation) has been introduced in section 2.1. For all the experiments in this chapter, we used protocol 1 which has been described in section 2.2.

5.2 IV Linearity and Device Conductivity

We first benchmark the IV linearity and salt-concentration dependency on the two types of pore-in-cavity devices, which can be compared with those of the nanocavities in section 3.2.

Figure 5.3a displays a typical linear I-V curve of a diameter-of-10 nm pore at 1 M KCl. Then we perform the I-V measurement for different salt concentrations. Figure 5.3b shows the derived conductance at different KCl salt concentrations. The conductance increases monotonically with the increasing of the concentration. Since TEM-drilled nanopores are almost not affected by the above cavity, we are able to adopt the equation (1) from Smeets et al

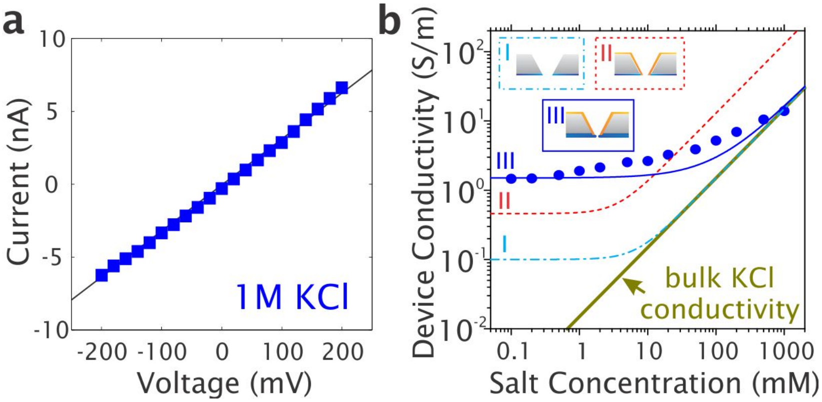

Figure 5.3: Ionic conductance measurements of a solid-state nanopore inside a SiN-backside coated gold nanocavity. (a) Current-Voltage (I-V) plot (b) The conductance measurements are performed at different salt concentrations from 0.1 mM to 1 M. The fitting curves are also imported from Figure 3.3. The light blue curve (I) represents the silicon nanopore with backside SiN (device #3 in Chapter 3), while the red dashed one (II) for the gold nanopore with backside SiN (device #4 in Chapter 3). The fitting curve for the pore-in-cavity device (III) is in blue. The arrow indicates the conductivity of bulk KCl.

[123], which describes a nanopore with diameter d and membrane thickness l as follows

$$G = \frac{\pi d^2}{4l}[(u_+ + u_-)N_A c_{KCl} e + u_+ \frac{4\sigma}{d}] \tag{5.1}$$

where d is the pore diameter, l is the membrane thickness, u_+ and u_- are the electrophoretic mobilities of potassium and chloride ions, $N_A c_{KCl}$ is the number density of potassium or chloride ions, and e is the elementary charge. The device conductivity σ_d can be written as

$$\sigma_d = (u_+ + u_-)N_A c_{KCl} e + u_+ \frac{4\sigma}{d}. \tag{5.2}$$

At high salts, the device conductivity is dominated by the ion transport, which highly depends the concentration of KCl. In the surface charge dominated regime, the device conductivity σ_d is related with the nanopore diamater d. We derive the effective thickness l as 28.8 nm and the surface charge density σ as -49.4 mC/m^2. On one hand, the effective thickness is significantly thinner than the deposited SiN (50 nm). However, we note that the SiN membrane thickness is not perfectly uniform (as measured by TEM) and the thinnest area is used to drill the nanopore. On the other hand, the estimated surface charge density is reasonable and comparable with the reported SiO_2/Si_3N_4 of -49 mC/m^2 [208].

For the ease of interpretation, the fitted conductivity curve of the silicon nanocavity backside coated with Si_3N_4 (device #3 in Chapter 3) is plotted in Figure 5.3b as well as that of the gold nanocavity backside coated with Si_3N_4 (device #4 in Chapter 3). All the device conductivities monotonically increase with the increasing of salt concentration. At high salts, in contrary to the high conductivity of gold nanocavities, the conductivity of the pore-in-cavity (device III) becomes close to that of bulk KCl. Besides the surface charge density at low salts, the conductivity at high salts becomes normal, which shows an improved performance compared with that of the gold nanocavities (device II).

Since the thermal oxidation has been shown to be a critical process in Chapter 4, here we characterize the pore-in-oxidized-cavity in Figure 5.4 as well as the oxidized cavities in Chapter 3.

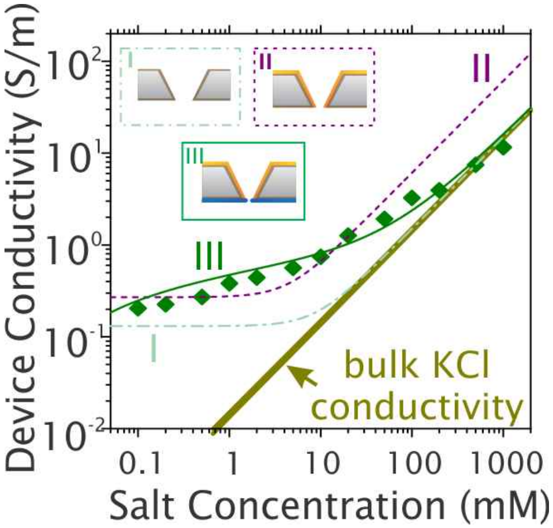

Figure 5.4: Ionic conductance measurement of a solid-state nanopore inside a thermally oxidized gold nanocavity. The conductance measurement are performed at different salt concentrations from 0.1 mM to 1 M KCl. The fitting curves are also imported from Figure 3.3. The light green curve (I) represents the thermally oxidized silicon nanocavity (device #5 in Chapter 3), the purple dashed one (II) for the gold nanocavity with thermal oxide (device #6 in Chapter 3), and the green one (III) for the nanopore-in-cavity with thermal oxide. The arrow indicates the conductivity of bulk KCl.

Basically, the conductance of nanopore-in-thermal-oxide-cavity increases with the increasing of salt concentration in Figure 5.4. However, at low salts, instead of a plateau, we observe a slope which can be described by the following equations [123]

$$G = \frac{\pi d^2}{4l}[(u_+ + u_-)N_A c_{KCl} e + u_+ \frac{4\sigma(c_{KCl})}{d}] \tag{5.3}$$

$$\sigma(c_{KCl}) = \sigma_0 + A \cdot \ln(c_{KCl}) \tag{5.4}$$

$$\sigma_d = (u_+ + u_-)N_A c_{KCl} e + u_+ \frac{4[\sigma_0 + A \cdot \ln(c_{KCl})]}{d} \tag{5.5}$$

where A is the coefficient constant for the salt-dependent surface charge density with a value of -13.0 mC/($m^2 \cdot$ ln[KCl]), and the surface charge density σ_0 here at 1 mM goes to -15.6 mC/m^2. The varied surface charge of nanopore in thermal oxide nanocavity could be explained as the local chemical equilibrium at different ionic strengths [123, 209]. The argument on the surface charge models needs more investigations on different batches of the chips, and we cannot draw a conclusion due to the time-line of finishing this thesis.

We present the fitted curves of thermally oxidized silicon nanocavity (device #5 in Chapter 3) and the gold nanocavity with thermal oxide (device #6 in Chapter 3) in Figure 5.4 as well. Different from the high conductivity at high salts of the gold-coated thermally-oxidized nanocavity, we observe that the conductivity of the nanopore-in-thermal oxide nanocavity becomes close to that of bulk KCl, demonstrating the improved ionic performance as well as the surface charge densities of the pore-in-cavity devices.

5.3 Noise Performance

In this section, we compare the two kinds of nanopore-in-cavity devices and link them with the previous measurements in section 3.3. For metallic nanopores, the backside coating is particularly of importance to avoid the plasmonic induced noise increase. Figure 5.5 summarizes the noise spectra of nanopores in Si_3N_4-coated (panel a) and thermal-oxide coated (panel b) gold nanocavities.

We compare the gold nanocavity without backside passivation (device #2 in Chapter 3.3), the backside SiN coated gold nanocavity (device #4 in Chapter 3.3) and the pore-in-cavity with backside SiN in Figure 5.5a. For the flicker noise at low frequency region, we observe the lowest spectral density of the pore-in-cavity device among these three devices in Figure 5.5a. For the dielectric noise component at high frequency, the behavior of pore-in-cavity device is similar to that of device II. These can be attributed to the thickness increasing of the dielectrics.

Figure 5.5b shows the comparison of the noise spectra, using thermal oxidation as the passivation approach. At low frequencies, the pore-in-thermal oxide

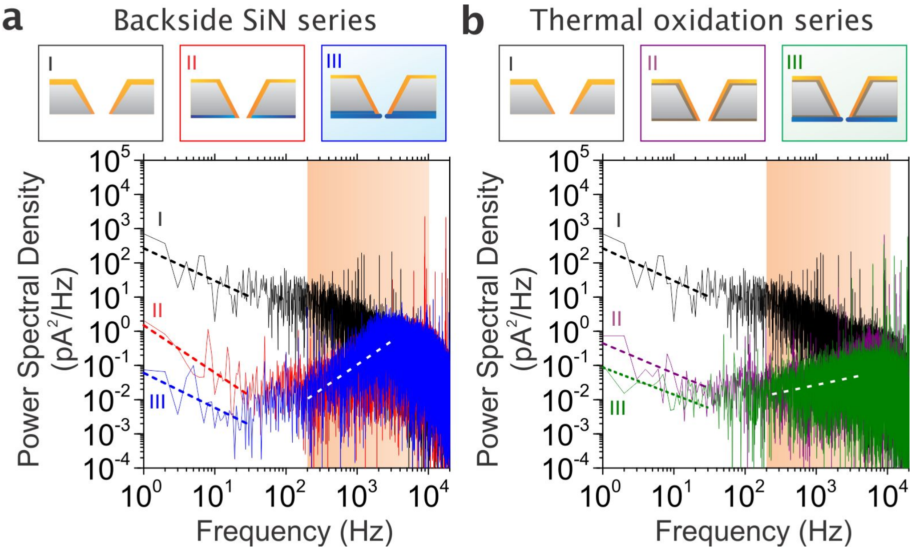

Figure 5.5: Noise spectra of solid-state nanopores inside gold nanocavity. (a) Noise spectra of original gold nanocavity (I, device#2, black), gold nanocavity with backside SiN (II, device#4, red) and SiN nanopore-in-cavity (III, blue). (b) Noise spectra of original gold nanocavity (I, device#2, black), gold nanocavity with thermal oxide (II, device#6, purple) and SiN nanopore in thermal oxide nanocavity (III, green). We use 1 M KCl, 10 mM Tris and 1 mM EDTA (pH = 8.0) as the electrolyte. All the traces are measured at +100 mV and filtered at 10 kHz.The orange window from 100 Hz to 10k Hz. The white dashed lines indicate the slope of dielectric noise components.

cavity (device III) provides the lowest flicker noise among the three devices in Figure 5.5b. At high frequencies, we observe that a low value of dielectric noise occurs on gold coated thermal oxide nanocavity and pore-in-cavity devices. This high-frequency noise is even lower than device II and III in Figure 5.5a. We can attribute this phenomenon to the change of the device capacitance. For thermal oxide devices, we have 77 nm thick oxide on both sides of the device, which is much thicker than only 50 nm SiN on the backsides for the device II and III in Figure 5.5a. Considering the dielectric constant of material, the capacitor area and the thickness, thermal oxidized devices have much smaller capacitances than the backside SiN ones. Since dielectric noise is mainly dependent on the device capacitance, thermal oxide chips have less dielectric noise compared to the Si_3N_4 passivated chips.

5.4 DNA translocations

In this section, we conduct DNA measurements using the described conditions in section 3.4. The experiments have been demonstrated on both the ionic flowcell and the optical flowcell mentioned in Chapter 2.2. The results using these two flowcells (not shown) are consistent and reproducible.

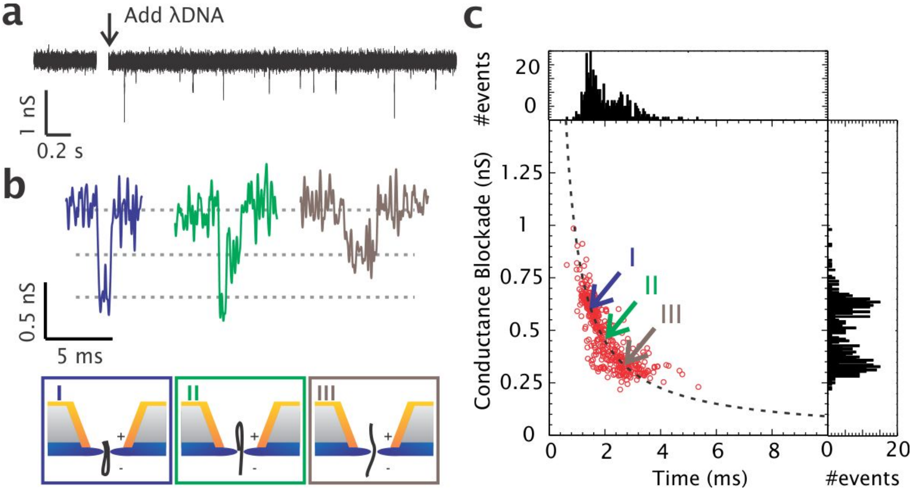

Figure 5.6: DNA translocation through a solid-state nanopore inside a SiN-backside coated gold nanocavity. (a) Translocation of 48.5 kbp double-strand Lambda phage DNA at 150 mV, showing the baseline conductance (left) and blockade events upon addition of 26.1 ng/μL DNA (right). (b) Examples of translocation events of fully folded (blue), partially folded (green) and non folded (brown). (c) Scatter diagram of the amplitude of the conductance blockade versus translocation time. Conductance and translocation time histograms collected from 422 events. The dashed line represents the constant event charge deficit of 0.18 nA·ms. Three arrows point to the locations of the events in panel (b). 1 M KCl, 10 mM Tris and 1 mM EDTA buffer (pH = 8.0) was used as the electrolyte.

Figure 5.6 shows the ionic current recording of long-strand DNA translocations. Comparing with the baseline current shown in Figure 3.5, we obtain a stable baseline with a well-reduced noise level. The noise reduction has just been discussed in section 5.3. The conductance of hybrid nanopore is 25.0 nS, indicating the existence of a diameter-of-10 nm pore on the membrane of the thickness of 33 nm.

Instead of unexpected current increases in Figure 3.5, we observe current decreases on every single event in Figure 5.6, which are not only in agreement with the events occurred on the state-of-the-art SiN pores at 1 M KCl [136, 210, 130]. Three types of events: unfolded, partially folded and fully folded events are illustrated in Figure 5.6b, slightly noisy compared to the literature [30, 211]. The dwelling time of unfolded events is likely twice longer than that of fully folded ones, while the amplitude of unfolded events becomes about half of that of the fully folded ones. Figure 5.6c shows the the amplitude-scatter plot of translocated DNA events. We observe two populations of the duration time at 1.6 ms (fully-folded events) and 2.9 ms (unfolded events), where the second value is in reasonable agreement with the translocation time of 1.7 ms for non-folded DNA molecules of the same type, in 1M KCl at +120 mV bias voltage [120], for a conventional SiN nanopore of similar dimensions as our cavity. Another two populations appear on the histogram of the conductance blockade with the amplitudes of 0.34 nS and 0.67 nS.

Most of the events are located surrounding a curve of constant event charge deficit (ECD) of 0.18 nA·ms [37]. ECD is defined by integrating the change in ionic current over the duration time of an event, which is a useful measure of the events. For unfolded, partially or fully folded events, the scatter of event amplitude and dwelling time should be statistically concentrated along an ECD curve. Our scattered result suggests that DNA molecules can smoothly transport through the pore-in-cavity device with folded and unfolded configurations [37, 212, 213].

The fact that some DNA events locate far away from the ECD curve, can be attributed to the temporary docking onto the walls of the nanopore during the translocation process. Although serious DNA cloggings on gold surface can be almost solved by replacing gold with SiN, DNA cloggings are still sometimes observable in our devices using SiN as the pore material. These cloggings can be attributed to the interactions between DNA and SiN, which has been also measured on conventional SiN pores [214]. By sending high voltage pulses, we also show the ability to rescue from some DNA clogging cases through our devices in Figure 5.7. These clogging events are discarded in data processing [214].

The pore-in-cavity devices show different performances from the performances of the gold nanocavities, especially on the ion transport and DNA translocations. The hybrid nanopore system maintaining gold only several nanometer away from the nanopore (verified by TEM), provides smooth translocations as well as conventional SiN pores.

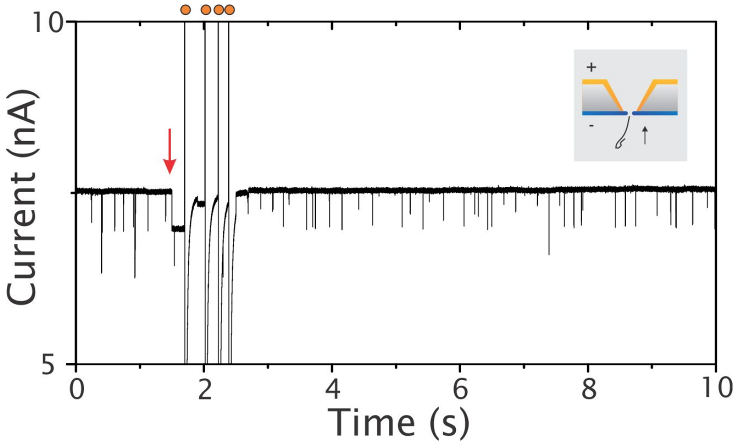

Figure 5.7: DNA clogging events in the translocation experiment and unclogging processes using pulsed high voltages. The experimental details are the same as Figure 5.6 except the bias voltage is set at +300 mV. Orange dots indicate the high voltage pulses.

5.5 Conclusions

Regulating critical interfaces of gold nanocavities by an additional dielectric layer can substantially improve the ionic performances of nanopores, particularly on the I-V characteristics and the DNA transport which are supported by numerical simulations of the electric field distributions. The introduction of a backside dielectric layer further decreases the 1/f noise. The proof-of-principle experiments on nanopore-in-cavity devices show good ionic performances and huge potential to be integrated with surface enhanced Raman spectroscopy. For nanopore fluidics, our device will provide an alternative and feasible detection towards DNA sequencing.

Our solid-state nanopore-in-cavity approach by tuning the critical nanopore interfaces, provides a solution to improve ionic performances on hybrid metallic devices such as metallized SiN pores [106, 129, 87], pores with tunneling electrodes [64, 215], gate electrode [216, 206] and zero-mode waveguide integrated pores [157, 217].

Chapter 6

Characterization of nanopore-in-cavity device with plasmonic excitation

In this chapter, we intend to perform a comparison of nanopore-in-cavity devices in different light illumination conditions. Based on the demonstrated ionic performance in Chapter 5, we study the devices upon plasmonic excitations. The investigation of plasmonic induced ionic effects will benefit us into two aspects. First, we could quantify the physical and/or chemical effects induced from the plasmonic excitation. Second, the noise effects in Chapter 4 could be examined on the nanopore-in-cavity with a better physical confinement.

In section 6.1, we first introduce the concept of the characterization upon light illumination, including the light-induced temperature profiles of the device and the calibration process for both the laser power and the ionic current. Then we will compare the ionic performances on nanopore-in-cavity devices under the dark and light conditions, which is mainly built on experimental results in section 6.2-6.4. We will examine the current deviation and noise spectral changes upon laser illumination in details. Besides, the DNA experiments will be performed with different laser power levels.

6.1 Introduction

Numerical Calculation upon laser illumination.

To have an idea on the details of the temperature distribution, we perform a numerical simulation of our nanopore-in-cavity device using the RF module and heat-transfer module in Comsol Multiphysics v4.3b, which has been described in Chapter 2.3. The simulated temperature distributions are shown in Figure 6.1. Since gold is more thermal-conductive than SiN, on X-Y plane in Figure 6.1b, we observe a higher temperature concentrated inside the cavity. Figure 6.1c shows X-Z plane profile where the local temperature can reach 60 °C at the orifice of the cavity using the 785 nm laser illumination of 15 mW. The localized temperature increase upon laser illumination would help us to understand the thermal effects on the ionic characterization.

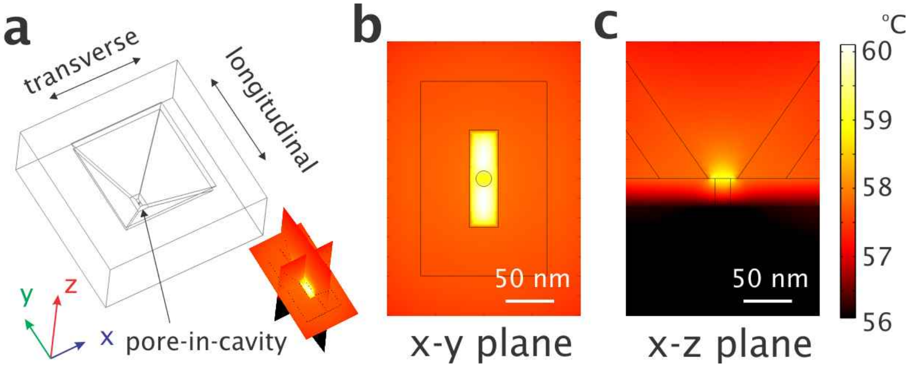

Figure 6.1: Numerical simulation of heat transfer in a gold nanopore-in-cavity. The power input is set as 15 mW at the wavelength of 785 nm. (a) 3D schematics of the nanopore-incavity and the temperture profile. (b) The temperature profile on xy plane. (c) The temperature profile on xz plane. The boundary conditions are the same as Figure 4.5. The temperature distribution in the large scale matches the results in Figure 4.5 as well.

For the estimation of I-V response, we used three modules in the COMSOL v4.3b environment: electrostatics (AC/DC Module), transport of diluted species (Chemical Species Transport Module) for the calculation of K^+ ions and Cl^- ions and laminar flow (Fluidic Flow Module). The resulting ionic current was obtained by integrating the flux density over the boundary of the reservoir. The physical parameters [218] used in the calculation are relative permittivity $\varepsilon_r = 80$, K^+ ion mobility $\mu_K = 7.8\times10^{-8}$ m^2/s·V, Cl^- ion mobility $\mu_{Cl} = 7.909 \times10^{-8}$ m^2/s·V, diffusion constant of K^+ ions $D_K = 1.957\times10^{-9}$ m^2/s, diffusion constant of Cl^- ions D_{Cl} = 2.032×10^{-9} m^2/s, fluidic density ρ = 1000 kg/m^3, dynamic viscosity μ = 8.91×10^{-4} Pa·S, and the surface charge density of SiN wall σ_{wall} = -49 mC/m^2. We validate our model by comparing analytical solutions of the Poisson-Nernst-Planck system with our numerical results as described in previous papers [219, 122, 220]. The result will be shown in Figure 6.9b.

Calibration of the motorized power sweeps

In the following experiments, we use the experimental protocol 4, which has been described in section 2.2. The laser illumination power was controlled using a motorized rotatable lambda half wave plate that controlled the polarization of the beam before it traveled through a polarization beam splitter. A second wave plate after the beam splitter enabled control of the polarization of the final excitation beam (longitudinal or transverse). The power after the second wave plate was further reduced by a neutral density (ND) filter and recorded with a power meter for different angles of the wave plate (Figure 6.2a). The resulting calibration curves enabled conversion of wave plate angle to power.

For power sweeps during ionic recording, we first set the angle of the motorized rotatable wave plate at a certain degree (0 degree), then switched on the laser so that we could observe the laser induced response (i). Next, we rotated the wave plate at different angular velocities back and forth (ii, typically between 0 and 120 degrees), after which the laser was switched off (iii). An example of such measurement is presented in Figure 6.2. Using the calibration curve, the time traces could be converted to I/I_0 versus laser power (Figure 6.2c).

6.2 IV Linearity

Ionic current increase upon laser illumination

In an optical flow cell, we first conduct ion transport experiments of the nanopore-in-cavity devices. Figure 6.3 shows the current-voltage response upon laser illumination. The I-V curve is linear in the laser power up to 6 mW as well as the curve in Figure 5.3. Therefore, the current increases at +100 mV can be normalized with the current value without laser illumination, shown in Figure 6.3a. We obtain stronger current enhancement on the transverse excitations than that on the longitudinal excitations. The slopes of current increase are 2.72×10^{-2} mW^{-1} for transverse excitation and 1.73×10^{-2} mW^{-1} for longitudinal one. In Figure 6.3b, numerical simulations of current increase

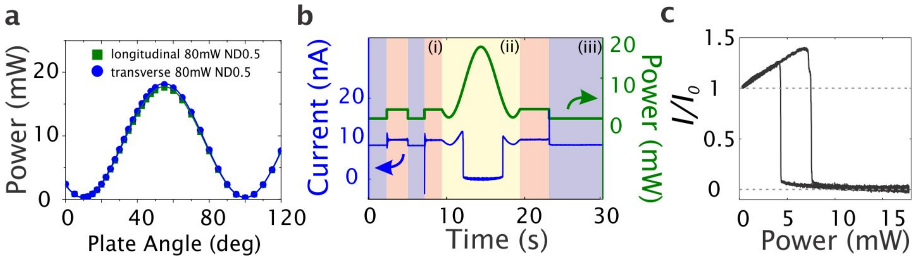

Figure 6.2: The procedure of power sweep measurement. (a) Output laser power as a function of angle of the motorized rotatable wave plate. The blue dots correspond to longitudinal excitation and the green ones correspond to transverse polarization. (b) Example of power sweep recording, here with angular velocity of 7.5 degree/s at +100 mV and with longitudinal excitation. The blue curve represents the ionic current and the green curve shows the output power as a function of time. (c) The normalized current as a function of power, which is derived from (b) using the calibration curve in (a).

are plotted based on plasmonic heating at the wavelength of 785 nm. Both of the two current increases exhibit linear dependencies on laser power. The slopes of the two are 9.56×10^{-3} mW^{-1} and 6.88×10^{-3} mW^{-1}, respectively. The ratio between the two polarizations goes to 1.39, which is close to the measured value of 1.57. This supports the statement that localized heating of the nanopore upon plasmon excitation can significantly contribute to the current elevation.

To study the above-mentioned effect of current increase in more detail, we perform ionic current measurements with spectral mappings. Figure 6.3c,d show the mapping results of a nanopore-in-nanocavity upon transverse and longitudinal excitations with Bragg mirror grating structures. Similar to noise increase on the gratings discussed in Figure 4.4, the current increase on gratings at transverse excitation in Figure 6.3c is in line with our expectation due to the excitation of SPPs. This confirms the current increase is due to the plasmonic excitation.

However, comparing Figure 6.3a,b, the simulated slopes based on thermoplasmonics are 2$\sim$3 folds lower than our experimental slopes, which are not totally understood. The strong current increase could be attributed to several reasons. First, our gold nanocavities have morphological variations during the processing (confirmed by SEM), hence the imperfect geometry may cause strong near-field coupling and further lead to huge enhancement. Second, the fact that our experimental enhancement is greater than the simulated one, may indicate that plasmonic induced heating is not the only ongoing process with illumination. Light-induced surface charge density increase has been demonstrated on SiN

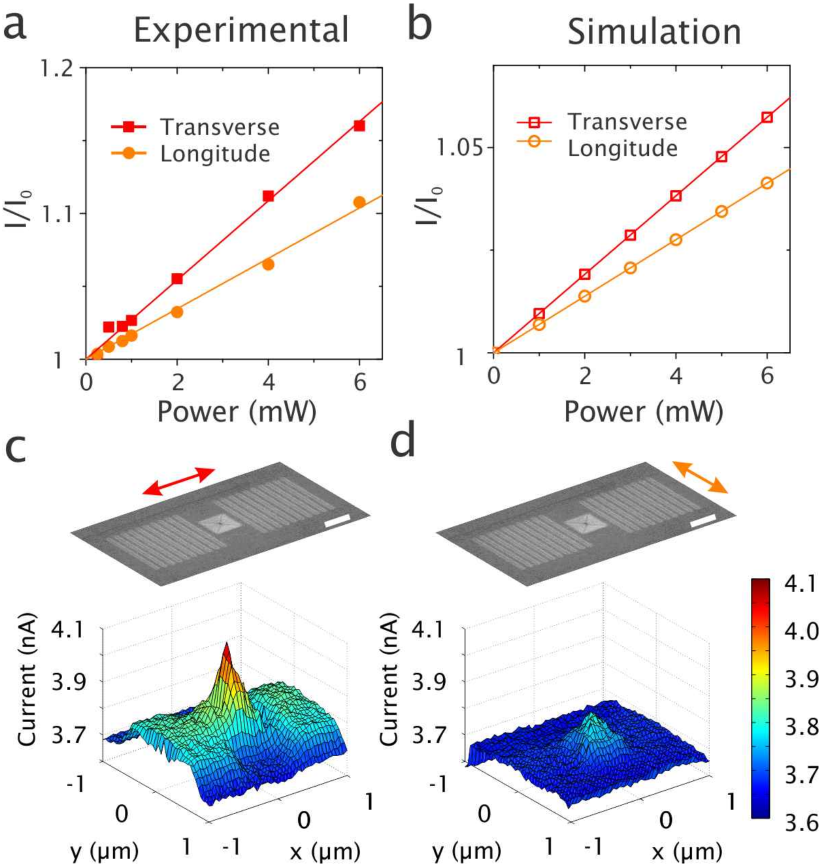

Figure 6.3: Laser-induced ionic current elevation. (a) Experimental normalized current increase as a function of laser power. The red squares stand for the current at the transverse excitations and the orange circles for the current at the longitudinal excitations. (b) Numerical simulation of plasmonic heating induced ionic current increase for both transverse and longitudinal excitations. (c) and (d) The ionic current map at 2 mW. The images of scanning electron microscopy are shown above the ionic current maps. The arrows indicate the direction of polarizations. The white bar is 1 μm.

nanopores [75], which could also be a plausible process occurring in our nanopore system. Moreover, plasmon-induced hot carriers [93] may contribute to the ionic current. All these three possibilities need to be further isolated and characterized.

Photoresistance switching of plasmonic nanopores

The results of this section were published in Nano Letters in the paper "Photoresistance Switching of Plasmonic Nanopores" [221].

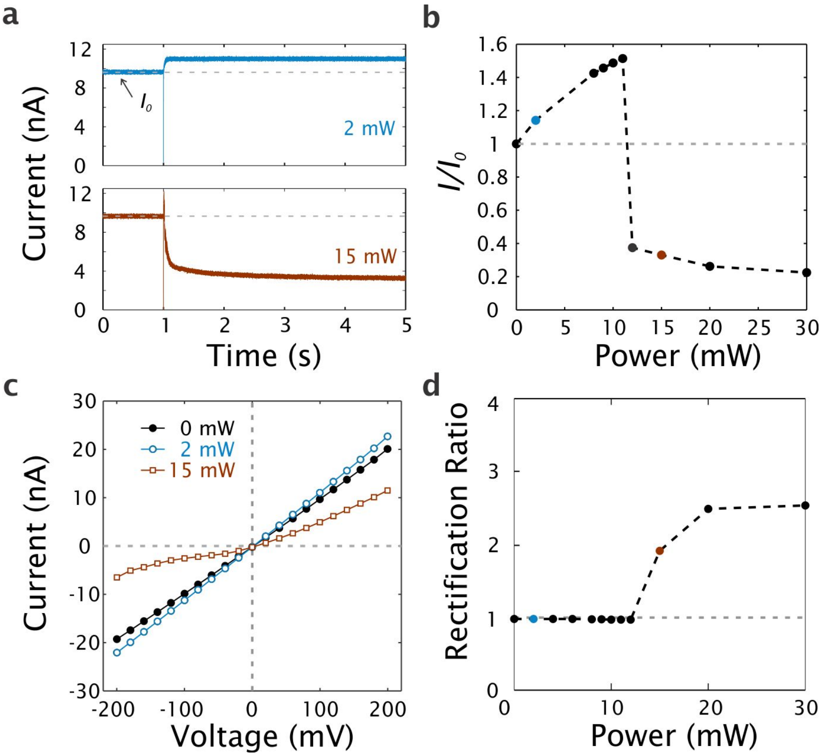

Figure 6.4: Ionic currents upon plasmonic excitation. (a) Ionic current versus time for 2 mW and 15 mW illumination turned on at 1 s, recorded at -100 mV. The sign of the current traces is reversed for clarity. The dashed lines indicate the open-pore current level I_0 before light illumination. (b) Normalized current deviation I/I_0 as a function of laser power at -100 mV. Blue and brown points indicate the laser powers of 2 mW and 15 mW, respectively. The dashed line at $I/I_0 = 1$ divides the figure into a top area of current increase and a bottom area of current decrease. (c) Current-Voltage curves at 0 mW (black), 2 mW (blue) and 15 mW (brown). (d) Rectification ratio γ(100 mV) versus laser power. The dashed line of γ(100 mV) = 1 indicates perfect linearity.

Plasmon-induced resistance switching. From previous simulations and experiments [89, 161], we know that surface plasmons can be resonantly excited in the plasmonic nanocavities at NIR wavelengths. We therefore use a 785 nm laser, tightly focused through a microscope objective (NA 1.2), to illuminate the plasmonic nanopore chips. Figure 6.4a shows examples of time traces without and with laser illumination, recorded at -100 mV. Upon switching on the laser excitation, the current response shows opposite behavior for 2 mW and 15 mW laser power. At 2 mW, the steady-state nanopore current increases, wehereas it instead decreases strongly at 15 mW laser power. We define the baseline without laser illumination as the open-pore current (I_0) and measure how the nanopore current (I) changes upon light illumination at different powers. The normalized current I/I_0 is presented in Figure 6.4b. The current increases monotonically with laser power up to around 12 mW. This is attributed to plasmonic heating and the corresponding increase in the buffer conductivity, as reported for other types of plasmonic nanopores [222]. Above 12 mW, the current level instead decreases dramatically upon plasmon excitation. In the example of Figure 6.4, the photoresistance at 30 mW becomes 500% of the original resting pore resistance. This current decrease is reversible: after switching off the laser illumination, the current level returned to its original value. Qualitatively, the results are the same when switching the polarity of the voltage that is used to monitor the ionic current (to +100 mV, see Figure 6.5). However, the threshold laser power at which excitation results in a current decrease instead of an increase is higher at positive polarity and the magnitude of the current decrease is also slightly lower. This is a first indication of an asymmetry in our system, as discussed further below.

The complete current–voltage (I-V) characteristics was investigated for three cases: (1) without laser illumination, (2) for a plasmon-induced current increase at low laser power, and (3) for a plasmon-induced current decrease at higher laser power. I-V curves in the range between -200 mV and +200 mV are presented in Figure 6.4c. Without laser illumination, the I-V curve (black) is linear and the slope yields a pore resistance of 11.0 MΩ. For a nanopore with a diameter of 10 nm, as determined from TEM images, and using the model by Kowalczyk et al. [132], this gives an effective pore length of 9.1 nm. In agreement with previous reports on other solid-state nanopore systems [132], the effective thickness is significantly thinner than the deposited PECVD SiN (50 nm). We also note that the SiN membrane thickness was not perfectly uniform (as measured by TEM) and we chose the thinnest area to drill our nanopore. The I-V curve is linear also upon illumination with 2 mW laser light, with the pore resistance reduced to 9.1 MΩ. By contrast, at 15 mW illumination, the I-V curve becomes rectified, with a significantly stronger plasmon-induced current decrease at negative voltages. We evaluate the degree of the rectification by defining rectification ratio

$$\gamma(V_{app}) = \frac{I(+V_{app})}{I(-V_{app})}. \tag{6.1}$$

In Figure 6.4d, V_{app} is set at 100 mV and the rectification is hence, calculated as the ratio between the measured current at +100 mV and -100 mV. The rectification ratio stays around 1 (no rectification) up to around 12 mW, followed by a significant increase to around 2.5 at higher powers. Notably, the power at which γ(100mV) starts to increase (12 mW) coincides with the power at which the current starts to drop (see Figure 6.4b).

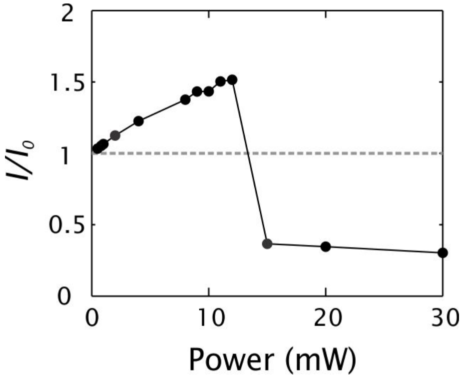

Figure 6.5: Normalized current deviation I/I_0 as a function of laser power at +100 mV. The dashed line of I/I_0 = 1 divides the figure to top area of current increase and bottom area of current decrease.

Rectification in nanopore systems is usually caused by overlapping electric double layers (EDL) in combination with an asymmetric structure, such that the charged nanopore walls partly restrict ions of the same sign from moving through the pore in one direction [223, 224]. Although primarily observed at low salt concentrations (more extended EDLs) [225], rectification has also been reported at high salt concentrations, for example, for conical nanopores in combination with nanoprecipitation [160, 226] or hydrophobic entrances [227, 135]. The rectification in the high-resistance state of our device is also likely related to asymmetry. By contrast, SiN nanopores have been shown to behave as Ohmic devices, with a constant conductance throughout the transmembrane voltage range, both with and without laser illumination [75]. This behavior is in line with our observations at no or weak laser illumination.

To investigate the dynamic response of the plasmon-induced resistance switching, we recorded the ionic current while continuously sweeping the laser power up and down. The laser power was modulated using a motorized rotatable wave plate and a polarizing beam splitter. It was calibrated in the linear power range between 2.3 mW and 16.2 mW, with a sweep rate from 0.05 mW/s to 5.7 mW/s. Details are described in section 6.1 and Figure 6.2. Figure 6.6 presents the ionic current versus laser power during power sweeps ($I-P$ curves).

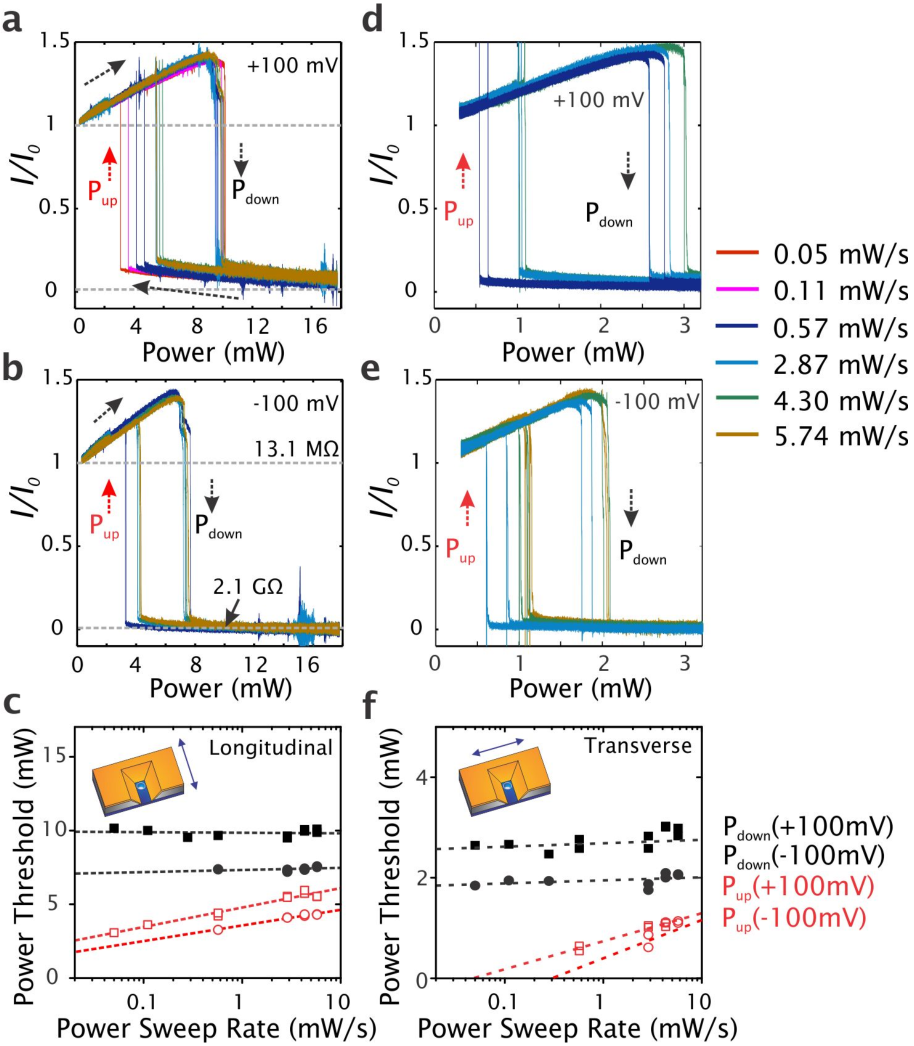

Figure 6.6: Ionic current versus power sweeps. Normalized ionic current at (a) +100 mV and (b) -100 mV during power sweeps at different sweep rates (longitudinal excitation). The gray dashed lines show the photoresistance values of 13.1 MΩ and 2.1 GΩ at the initial resting state and high power state, respectively. (c) Transition thresholds as a function of sweep rate. Normalized ionic current at transverse excitation at (d) +100 mV and (e) -100 mV, during power sweeps at different sweep rates. (f) Transition thresholds (P_{down} and P_{up}) as a function of sweep rate in transverse mode. The thresholds are chosen at I/I_0=0.5. Black solid markers correspond to P_{down} and red hollow markers correspond to P_{up}.

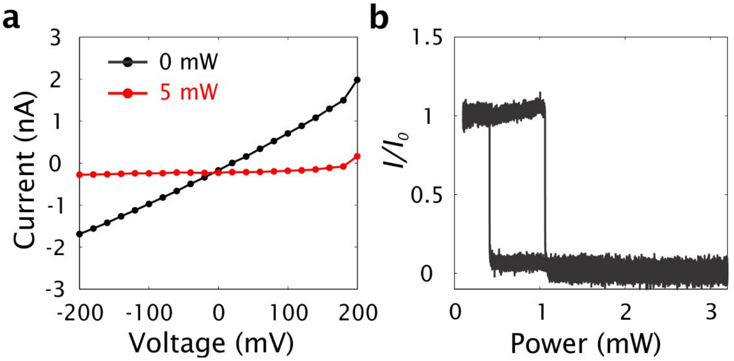

Figure 6.7: Ionic current measurement in 0.1 M HCl (transverse mode). (a) I-V curve at 0 mW (black) and 5 mW (red) (b) Power sweep at +100 mV.

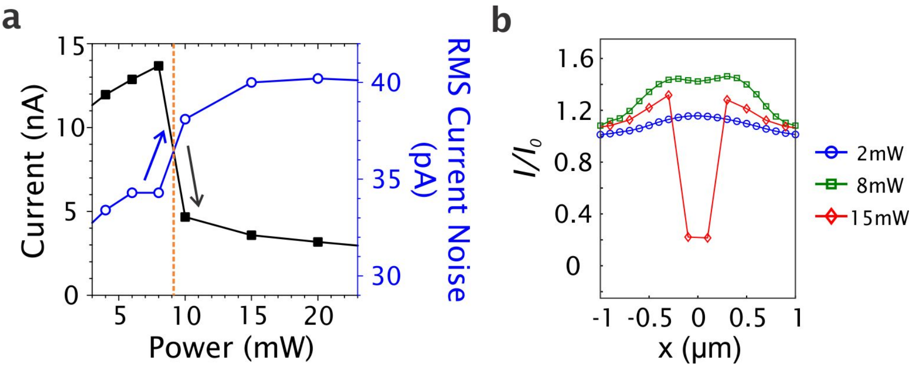

Figure 6.8: Current noise and relative conductance profiles. (a) Nanopore current at 100 mV and RMS current noise filtered at 2 kHz as a function of laser power (transverse excitation aligned with nanopore). (b) Variation in the ionic current through a nanopore as a function of position of the focused laser with respect to the pore center. The three scans were acquired at 100 mV, at 2 mW (blue), 8 mW (green) and 15 mW (red). We note that the scan at 15 mW is measured on a different device from the scans at 2 mW and 8 mW.

In agreement with the results presented in Figure 6.4b, the current increases monotonically with increasing laser power for low powers. This is followed by an abrupt transition from high to low current at a certain laser power (at P_{down}), after which the current decreased further for higher powers. When the power is instead swept from high to low power, a similar behavior is observed, with an abrupt transition (at P_{up}) from low to high current, after which the current follows the initial linear dependence at low powers. Notably, the photoresistance at high power reaches values as high as 2.1 GΩ, which yields an over 150-fold increase over the original resistance of 13.1 MΩ. There is a clear hysteresis in the behavior: P_{down} is considerably higher than P_{up}, showing that a higher laser power is required to reach the high-resistance state than to switch it back to the low resistance state.

The hysteresis is quantitatively investigated in Figure 6.6c, for which the laser powers at $I/I_0 = 0.5$ define the power thresholds for the transitions. Three clear trends are observed. First, P_{up} is always lower than P_{down}, reflecting a similar hysteresis behavior for all sweep rates. Second, while P_{down} is largely independent on the power sweep rate, P_{up} increased with increasing sweep rate, thereby narrowing the hysteresis windows for higher sweep rates. Third, the thresholds are found to be dependent on the transmembrane voltage and they are consistently lower for negative bias. For example, P_{down} shifted from 10 mW at +100 mV to 7 mW at -100 mV (see Figure 6.6c). The power sweep results for transverse excitation were qualitatively the same as for longitudinal excitation (see Figure 6.6d-f), although the threshold for the two transitions were shifted to lower laser powers due to the better coupling of light to plasmons in the transverse mode (illustrated in Figure 6.6c,f).

Origin of the photoresistance switch. In order to understand the origin of the plasmon-induced photoresistance switching, several hypotheses were explored. Various processes are known to affect the ionic current of solid-state nanopores, including changes in the buffer temperature [222] or changes in the surface charge of the nanopore walls [75]. However, although both surface charge and temperature were recently shown to vary upon laser illumination [222, 228, 75], this resulted in monotonic increase in the ionic current upon laser excitation for increasing power. Hence, although such processes are consistent with the initial current increase at low laser powers, they cannot explain the observed abrupt resistance switch and current decrease at higher laser powers. Instead, the photoresistance switch is likely related to blockage of the pore and a corresponding restriction of the ionic flow through the pore at high laser powers. Biomolecules or other nanoparticles that could potentially block a pore were not present in our buffers, as confirmed by dynamic light scattering. Instead, we propose that the photoresistance switch is due to plasmon-induced formation and growth of nanometer-sized gaseous bubble(s) [229, 230, 231] that block the plasmonic nanopore.

We use several reported methods to evaluate if nanobubble blockage is the most pausible explanation for the high resistance state of our plasmonic nanopore. First, we note that a strong decrease in the ionic nanopore conductance has been previously correlated with the presence of gaseous nanobubbles [227]. In that study, experiments were repeated at a high concentration of protons (HCl) to verify that the current decrease corresponded to the pore being blocked by bubbles and not by a volume filled with (nonionic) liquid water. The fact that we observe a pronounced photoresistance switching also in 0.1 M HCl (Figure 6.7) is a strong indication that the high-resistance state is related to vapor that blocks the plasmonic nanopore. Furthermore, the presence of gaseous nanobubbles inside nanopores was also recently correlated with an increase in the nanopore current noise [230]. This is consistent with our observations, as we observe a significant increase in the current noise when the system enters the high-resistance state (Figure 6.8a). Smeets et al [230] also reported that scanning the position of a nanobubble-containing nanopore through a laser focus resulted in a double-peak in the ionic conductance, with a small dip at the focal spot due to nanobubble growth inside the nanopore. Indeed, we sometimes also observed this behavior for our system when scanning at intermediate laser powers close to the switching threshold (Figure 6.8b). All these experimental results match with and strengthen the proposed bubble hypothesis.

We use finite-element simulations to investigate if nanobubble blockage of the nanopore is consistent with the experimental observations, including the rectification behavior for the low-conductance state. We simulated the $I - V$ response of the plasmonic pore-in-cavity using COMSOL Multiphysics 4.3b (see section 6.1). Figure 6.9a illustrates three possible scenarios: 1) an open 10 nm in diameter pore, 2) the same 10 nm nanopore with a bubble on top of the orifice near the gold cavity, and 3) the same nanopore with a bubble facing away from the gold cavity. We used aqueous 1M KCl solution as buffer medium. The surface charge density of the SiN wall was configured as -49 mC/m^2, corresponding to the reported data [218] for SiN at pH 8.0. The closest distance from the bubble to the nanopore wall was chosen as 0.5 nm in order to have overlap between the electric double layers (EDL) of the pore and the bubble (the EDL thickness is only 0.3 nm at 1 M KCl) [232]. The simulated results of $I - V$ curves of the three scenarios are shown in Figure 6.9b. As expected, the open pore (blue curve) gives a linear $I - V$ dependence. Both scenarios with a bubble partially blocking the nanopore (brown full curve and gray dashed curve) result in a significant decrease in the nanopore conductance and nonlinear $I - V$ curves, with opposite rectification behavior. For both bubble scenarios, the preferential current direction is towards the constricted side where the bubble is positioned, as previously also reported for conical nanopores [233]. The

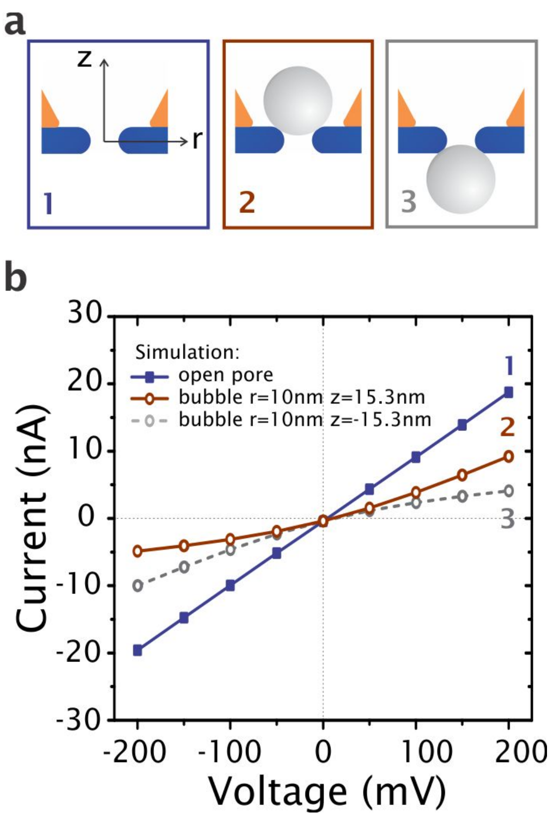

Figure 6.9: Numerical simulation of current-voltage curves of plasmonic nanopores. (a) Schematics that represents the three different simulations. The blue scenario 1 represents the nanopore without any bubble, whereas the brown scenario 2 has a nanobubble on top. The gray scenario 3 has a bubble at the other side of the pore entrance. (b) Simulated I-V curves of three scenarios in panel (a). γ*(100 mV) for scenario 2 is 1.56, whereas* γ*(100 mV) for scenario 3 goes to 0.64.*

rectification behavior observed experimentally (see Figure 6.4c) is in agreement with the simulated results for a bubble that blocks the pore from the top of the membrane near the gold cavity (scenario 2). The opposite rectification behavior was never observed experimentally. Hence, the combined experimental and simulated results strongly indicate that the low-conductance state at high laser power illumination is due to a bubble that blocks the pore and that the bubble formation occurs on the side of the plasmonic cavity. The rectification behavior may also be influenced by the dynamic nature of the bubble-nanopore system,

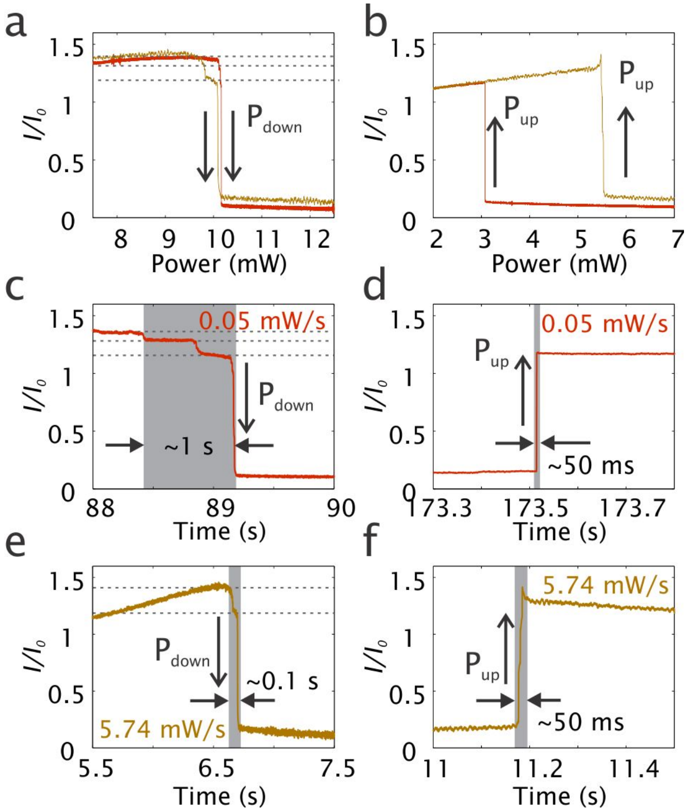

Figure 6.10: Multi-level current steps as a function of illumination power (a-b) and time (c-f), respectively. (a) P_{down} *and (b)* P_{up} *are the zoomed curves of Figure 6.6a. Only the curves with highest velocity (in red) and slowest velocity (in yellow) are shown here. Dashed lines show the normalized current levels. (c-d) The time series of transitions at the power sweep rate of 0.05 mW/s, (e-f) at the power sweep rate of 5.74 mW/s. The gray areas indicate the duration time for each individual transition events.*

as discussed further below.

Work flow of the photoresistance switch. Figure 6.11 depicts the proposed workflow of the photoresistance switch. At low powers, the current increases with increasing laser power, which could be primarily attributed to local plasmonic heating and corresponding increase in buffer conductivity [222]. Nanobubble(s) may be nucleated in this phase and start to grow in size with increasing laser power, but they do not block the ionic current. Upon further increase in illumination power, the current exhibits an abrupt drop to a high-resistance state. This switch corresponds to the lumen of the pore becoming blocked by one (or several) bubble(s), located at the interface between the gold cavity and the SiN pore. We typically observe an abrupt drop with multiple steps in the ionic current (see Figure 6.10), which is likely due to coalescence of multiple bubbles. At even higher powers, the pore lumen is increasingly further blocked by the growing nanobubble. When sweeping back to low power, the abrupt switch to the low resistance state can be attributed to bubble release from the orifice of the pore, which may be accompanied by multiple-step bubble collapse. Potential tiny bubble(s) that remain away from the pore lumen will not significantly affect the ionic current. The recovered current after P_{up} follows the same slope as before the bubble blockage.

The hysteresis observed during laser power sweeps (Figure 6.6) shows that higher powers are required to block the pore with a bubble than to keep the bubble from releasing from the pore when it is already there. This is similar to the hysteresis in the force curves and jump-in/off events that were observed for the interaction between AFM-tips and nanobubbles [234], especially on gold surfaces [235]. This behavior is in good agreement with a capillary force model based on positive forces between the bubble and the AFM tip. We anticipate that the hysteresis in our system is also related to attractive forces between the bubble and the plasmonic pore, which create an energy barrier that needs to be overcome in order to release the bubble from the pore.

The dependence on bias voltage polarity for the transitions for blockade and release may be related to the dynamic nature of the bubble-nanopore system. Previous reports suggested that nanobubbles are negatively charged [236] and they will therefore be pulled towards the pore at negative bias. Negative transmembrane voltage may therefore assist bubble blockage, whereas positive bias does not. This is in agreement with our experimental finding that the transition thresholds for bubble blockage and release shift to higher laser powers for positive bias (see Figure 6.6c). In this respect, we also note that electrophoretic forces may influence how tightly the bubble blocks the pore in the high-resistance state and, in turn, contribute to the rectification.

Nanobubble generation. Plasmon-induced Joule heating and the heterogeneity of the gold/silicon nitride interface are likely playing a role in the nanobubble formation. The plasmonic local heating leads to an estimated nanopore temperature of around 50 °C at P_{down} (using $I/I_0 = 1.5$ before the switching) [222]. This temperature, which is expected to be slightly higher at the gold surface, is sufficiently high to facilitate nucleation of surface nanobubbles [237]. Hence, it is plausible that the formation and growth of gaseous nanobubbles is the result of plasmonic heating. We further note that the abrupt switching occurs at approximately the same temperature (i.e., same I/I_0)

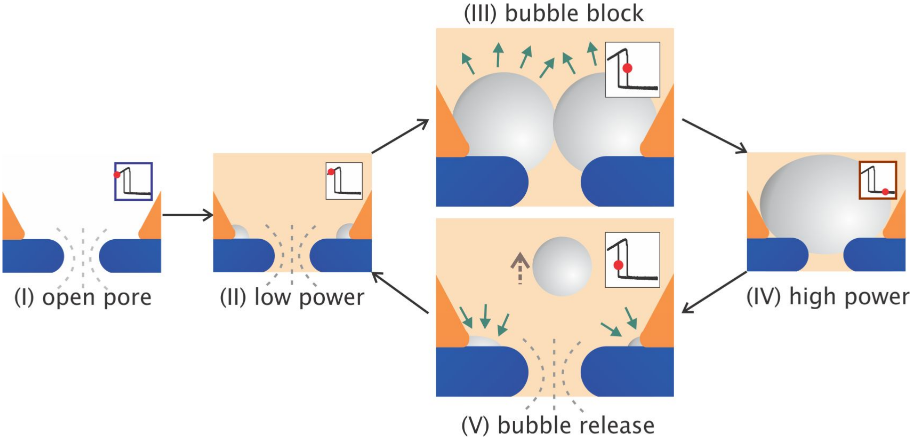

Figure 6.11: Proposed workflow of the photoresistance switch. (I) original state without laser illumination, (II) bubble growth at low power, (III) transition to bubble block, (IV) bubble retention at high power and (V) bubble release that may contain the processes of bubble residues shrink at the interfaces and/or bubbles escape away from the pore entrance. The insets indicate each scenario as a red spot located in the hysteretic $I-P$ curve.

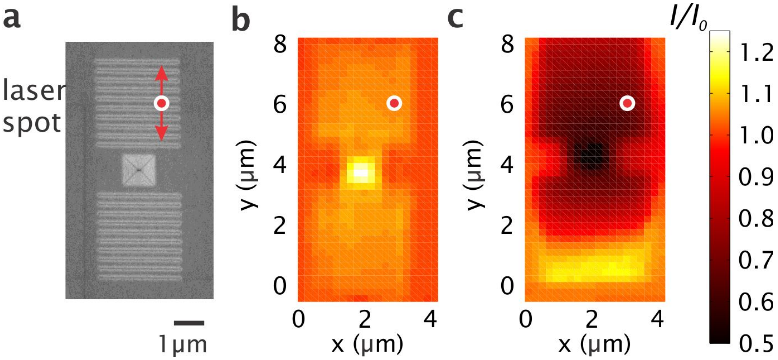

Figure 6.12: Ionic mapping in the x-y plane with transverse excitation at +100 mV. (a) Schematic representation of the laser spot on the plasmonic structure of a nanocavity with gratings. The arrow indicates the transverse polarization, which was used for this measurement. The white and red circle marks the approximate laser spot size. (b) 2D ionic current map by scanning the entire plasmonic structure at 2 mW. (c) 2D ionic current map at 15 mW.

regardless of the power sweep rate (see Figure 6.6), indicating that the process of pore blockage (at P_{down}) does not require a rapid change in temperature. By contrast, the bubble release (at P_{up}) occurs at lower temperatures for decreasing sweep rates. This observation indicates that a rapid change in temperature aids the bubble release, possibly due to forces related to changes of the fluidic flow upon rapid temperature variations.

Finally, we use remote plasmon excitation based on a grating structure on the side of the plasmonic cavity [131, 89] to confirm that the photoresistance switching indeed is a plasmonic effect and not due to, for example, direct light absorption by the buffer medium. Tightly focusing the laser on the gratings allowed for excitation of surface plasmon polaritons (SPPs) (and, in turn, remote excitation of the plasmonic nanocavity) [114] without direct illumination of the nanocavity and the nanopore. The results are presented in Figure 6.12 and unambiguously show a current decrease also by remote plasmon excitation at high (15 mW) laser power.

In conclusion, we demonstrates photoresistance switching of a novel plasmonic nanopore based on a solid-state nanopore located inside a plasmonic gold nanoslit cavity. We have shown that laser light focused onto such plasmonic nanopore can reversibly cause ∼1-2 orders of magnitude photoresistance switching. On the basis of combined results from several different types of measurements, we conclude that the most plausible explanation of the high resistance state is blockage of the nanopore by a bubble. Furthermore, the low-conductance state is accompanied by a rectified $I-V$ response. Finite-element simulations showed that this is in agreement with a bubble that blocks the nanopore from the side of the cavity. To the best of our knowledge, this is the first demonstration of a plasmon-controlled fluidic nanovalve. Moreover, the presented device is also a plasmon-assisted ionic rectifier, which remarkably operates at high salt concentration. Whereas previous reports of systems that were based on long channel lengths (>300 nm) and required a few volts as bias voltage for opening the nanopore [227, 238], our plasmonic nanopores provide a membrane thickness as thin as tens of nanometers or less, and the switching can operate at low (±100 mV) bias voltages with the assistance of light, which allows for use in fast solid-state nanopore sensing applications [151].

There is a growing interest in using bubbles as an active element in nanoscale fluidic devices [239, 240, 241]. Utilizing nanobubbles for rapid and reversible switching of nanopores can accelerate the development of such novel nanofluidic systems and can also help to gain a better understanding of the mechanism of nanobubble formation. By the exploiting high sensitive ionic transport through plasmon-modulated nanobubble-pore systems, our devices provide a unique system to probe the still largely unknown nanobubble properties. We believe the results of this work will help to understand the basic principles of plasmon-assisted fluidic nanosystems.

6.3 Noise Performance

We perform noise measurements upon laser illumination on the two kinds of devices: solid-state nanopore in gold cavity with two SiN layers and solid-state nanopore in thermally oxidized nanocavity. The noise performances of these two in dark conditions have been discussed in section 5.3, which are comparable to that of the state-of-the-art pores and feasible for DNA experiments. Besides, the noise performances of the two devices without the backside SiN layer have been discussed in section 3.3 and 4.2. The proposed nanopore-in-cavity devices may have the advantages of low noise level both in dark and illuminated conditions. We expect the nanopore-in-cavity devices could become the solution to avoid any laser-induced ionic noise.

Noise increase as a function of laser power

Plasmon-induced noise spectral changes are of importance since the photon-matter interaction can practically be probed in terms of ion transport. For nanopore-in-cavity devices with twice SiN depositions, Figure 6.13 shows the noise spectra upon longitudinal excitations at +100 mV. At low frequencies, the amplitude of the 1/f noise monotonically increases with the laser power. As the 1/f noise is rather high in a gold nanocavity channel [131, 148], the changes upon different laser powers in Figure 6.13 are not observable in a huge background in Figure 4.3b.

In the middle frequencies, the Lorentzian component (shown in white dashed line) appears with a corner frequency between 50 Hz and 500 Hz, which is in agreement with our previous study of Lorentzian components. This suggests that thick layers (>50 nm) of SiN are not yet a perfect solution to passivate the silicon-electrolyte interfaces. Since this Lorentzian noise cannot be originated only from plasmonic induced heating [131], other pathways such as charge injections, surface desorption and/or photochemistry, should be considered in the nanopore-in-cavity system.

The study of noise spectra not only enables the improvement of the device performance, but also contributes to a better understanding of plasmon-induced energy transfer, which motivates us to conduct the measurements on thermal oxidized devices.

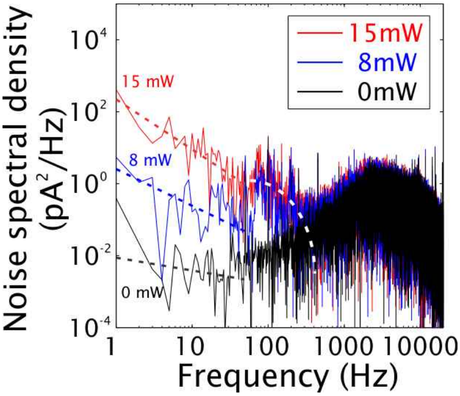

Figure 6.13: Noise spectra of the nanopore-in-cavity with backside SiN at different laser powers on longitudinal excitation. Black, blue and red dashed lines fit the slopes of 1/f noise at 0 mW, 8 mW and 15 mW, whereas the white curve indicates the Lorentzian component in the middle frequency range.

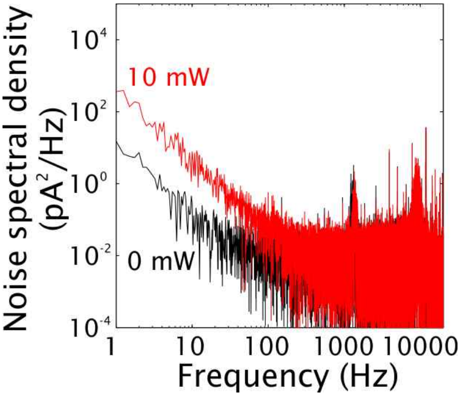

Figure 6.14: Noise spectra of a SiN nanopore in thermally oxidized nanocavity device upon longitudinal excitation at different laser powers at +100 mV.

Noise reduction using thermal oxidization

Thermal oxidation exhibits great performance on backside isolation upon laser illumination. The results of gold-coated thermally-oxidized nanocavities integrated with SiN nanopores are shown in Figure 6.14. Above 100 Hz, the noise spectra with and without longitudinal excitation are almost the same. The Lorentzian component disappears in the spectra of this type of devices, which is in agreement with that of the device without SiN layer in section 5.3. The flicker noise arises upon laser illumination, which we do not fully understand.

6.4 DNA translocations

Since the performance of DNA translocations of a pore-in-cavity device without laser illumination has almost achieved that of a conventional SiN nanopore, the transport process upon plasmonic excitation becomes quite promising. We performed the DNA experiments in the same condition as that in section 5.4. The results are shown in Figure 6.15 and 6.16.

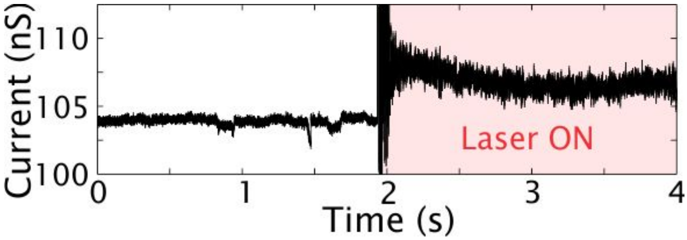

Figure 6.15: DNA experiment at a low power of 2 mW, filtered at 2k Hz. The applied voltage is +200 mV.

Using the solid-state nanopore in a gold nanocavity devices, we are able to detect DNA events in the dark condition. However, since the ionic noise increases with the increasing of the current at the 2 mW, we could not determine the translocation events due to the poor signal-to-noise ratio (SNR) in Figure 6.15. This becomes more serious at high powers in Figure 6.16. At the 12 mW, the current decreases but the noise level becomes much higher than the DNA events detected at 0 mW. Compared to Figure 4.2, the laser-induced noise has been dramatically reduced but the SNR is not sufficient to record the DNA events. As a result, it is difficult to draw a conclusion whether or not we can thread DNA through a nanopore-in-cavity upon laser illumination.

In section 6.3, we can find out that the nanopore in gold-coated thermally-oxidized nanocavities can effectively inhibit the Lorentzian components, providing less-noisy current baseline than the current traces in Figure 6.15 and 6.16. We would suggest to verify the DNA translocation upon laser illumination on such pore-in-cavity devices with thermal oxide.

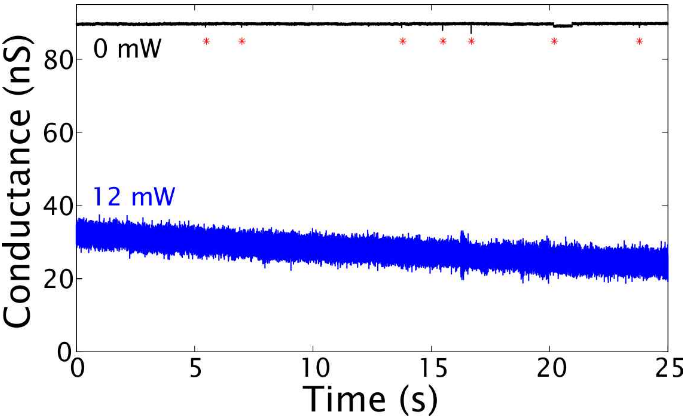

Figure 6.16: DNA experiment at a high power of 12 mW, filtered at 2k Hz.The DNA events are marked with read asterisks.

6.5 Conclusions

We have characterized laser-induced effects on nanopore-in-cavity devices. Besides induced ionic noise, we observe the deviation phenomena of ionic current upon laser illumination which differ from gold nanocavity devices. A plausible explanation could be the plasmon-induced Joule heating. The Lorentzian component(s) of noise is strongly reduced with SiN layer, while ionic current deviations become dominated on the pore-in-cavity devices.

Importantly, we present the first demonstration of a reversible plasmon-controlled nanofluidic valve. We show that plasmonic nanopores (solid-state nanopores integrated with metal nanocavities) can be used as a fluidic switch upon optical excitation. We systematically investigate the effects of laser illumination of single plasmonic nanopores and experimentally demonstrate photoresistance switching where fluidic transport and ion flow are switched on or off. This is manifested as a large (~1-2 order of magnitude) increase in the ionic nanopore resistance, and an accompanying current rectification, upon illumination at high laser powers (tens of milliwatts). At lower laser powers, the resistance decreases monotonically with increasing power, followed by an abrupt transition to high resistances at a certain threshold power. A similar rapid transition, although at a lower threshold power, is observed when the power is instead swept from high to low power. This hysteretic behavior is found to be dependent on the rate of the power sweep. The photoresistance switching effect is attributed to plasmon-induced formation and growth of nanobubbles that reversibly block the ionic current through the nanopore from one side of the membrane. This explanation is corroborated by finite-element simulations of a nanobubble in the nanopore that show the switching and the rectification.

We report high noise levels in DNA experiments upon laser illumination, which cannot provide the recording of DNA translocation events using the pore-in-cavity with twice SiN depositions. We also point out that DNA translocations would be more feasible to be accomplished on thermally oxidized devices due to the reduced noise upon laser illumination.

Chapter 7

Conclusions and Outlook

7.1 Conclusions

Nanopore research has gained great interest because of its capability to probe single molecules. Recently, several research groups and companies have started to invest in the combination of plasmonics with nanopores [222, 228, 87, 201]. In contrast to their results that focus on adding plasmonic components onto conventional nanopore devices, this dissertation aims to make use of the optimized plasmonic nanocavities as fluidic nanopores.

1. Design and Fabrication - from metallic nanocavities to nanopore-in-a-metallic-cavity

In Chapter 2 of this dissertation, two processing flows for the nanocavity were presented. The first method uses e-beam lithography, providing us great flexibility on nanocavity design. The second method makes use of DUV lithography directly on 200 mm wafers. The latter method enables us to fabricate many nanocavities with high reproducibility. This work demonstrating the strength of making nanocavities in a CMOS production environment is in sharp contrast to many other groups working with nanopores fabricated by slow processes.

We further proposed and successfully fabricated pore-in-cavity devices in collaboration with Prof. Dekker's group in TU Delft. These devices combine strong plasmonic-enhanced nanocavities with a solid-state nanopore defined by TEM. As such, we demonstrate the first PECVD SiN nanopore beneath a gold nanocavity, which avoids the high-temperature process in the conventional LPCVD of a stress-free SiN layer.

2. Electric performances of metallic nanopores

By combining an electrical measurement set-up with a Raman microscope, we characterize the ionic properties of our devices in three items: the linearity and conductivity of current-voltage (I-V) response, the noise spectral density and the DNA translocation events, as described in Chapter 3 and 4. These three ionic properties of our nanopore devices are found to be strongly affected due to the introduction of the gold layer.

First, despite that the gold nanocavities all show linear I-V responses, the salt dependent conductance measurement exhibits a higher than predicted device conductivity, indicating that conventional fixed surface charge models do not apply. Although there is no clear conclusion yet, we attribute this phenomenon to excess free charges, induced surface charges and related electron transfer through the gold-electrolyte interfaces.

Second, in dark conditions the noise level is much higher than that of the state-of-the-art SiN nanopores. The increased noise can be found on gold nanocavities due to the lack of any dielectric layer on the membrane. Coating the backside of nanocavity with SiN or thermally oxidizing the silicon nanocavity allows the reduction of the ionic noise, mainly by suppressing the 1/f noise. However, the best noise performance of gold nanocavities with thermal oxide still has about an order of magnitude higher 1/f noise than the conventional SiN nanopores [118].

When translocating DNA molecules through our metallic nanocavities in high salt concentrations, instead of the expected current drops, we observed only events with a current increase – contrary to results for classical dielectric nanopores, where current increase events only occur experimentally for relatively low salt concentrations. Moreover, the events are considerably longer than expected as well. Our results differ from state-of-the-art current drops at 1 M KCl, which may due to unspecific absorption, charge depletion or other effects occurring inside the gold cavity. Although clear DNA events could be recorded, the low fidelity and poor reproducibility make the metal nanocavity device performance difficult to compete with conventional SiN nanopores.

Besides the characterization of the metal nanocavities, also the ionic properties of the nanopore-in-cavity devices are benchmarked (Chapter 5 and 6). The noise is lower than metal cavities but still slightly higher than the state-of-the-art SiN nanopores. We find out that the noise level of the nanopore-in-cavity device is sufficient for single molecule DNA sensing. The better noise performance of the pore-in-cavity devices compared to that of the metallic nanocavities, can be explained by the backside coating with SiN layer. This results in linear I-V curves, good conductivity and the state-of-the-art DNA current blockage and dwelling time (i.e. without laser illumination).

3. Plasmonic induced ionic effects

When shining light onto the metallic nanocavities, we study plasmonic induced effects in terms of the ionic noise we take advantage of voltage-sensitive SERS probes to study the local potential in our nanocavity devices (Chapter 4). We demonstrate that plasmonic induced ionic noise can be highly suppressed by tweaking the layer stack slightly. We also show the relationship between the local potential inside the metallic nanocavity and the electrochemical processes, which promotes our understanding on the ionic behavior of these nanocavity devices.

Similarly, laser-induced ionic responses of pore-in-cavity devices are systematically evaluated (Chapter 6). We report for the first time on the photoresistance switching of plasmonic nanopores, which is also the first plasmon-controlled fluidic nanovalve based on the optical-induced resistance. The observed switching behavior is attributed to the formation of bubbles which block the fluidic channel. The rectification of the I-V curve at high powers, also enables this phenomenon to be used as a plasmonic-controlled ion rectifier.

7.2 Outlook

Plasmonic, metal-covered nanopores for DNA detection are still in their infancy and some scientific and technical hurdles need to be overcome. Especially for their use in sequence application, more work is needed to optimize the SERS readout and control the velocity of stochastic DNA motion. Still, even besides sequencing and as stated below, other aspects and applications can be of interest and justify further research.

Mechanisms of Ionic conduction through Metallic Nanopores

Although we have almost coped with the metallic induced effects, there are several open scientific questions during our study of metallic nanopores. For example, the high device conductivity due to the present of gold layer on top of the nanocavity structures, the current increase instead of current decrease of DNA translocation events at high salts, the exact catalytic process for noise generation and the specific gas(-es) of the generated nanobubbles, still need a lot of further studies.

The origin of high conductivity of metallic nanopores and current increase for DNA events may be attributed to similar hypotheses: the high surface charge density, the motion of electrons induced charge depletion or electron transfer induced by electrochemical processes. Although we are currently limited by the knowledge and methodologies, these hypotheses need to be differentiated with more evidences to fully understand the role of the metals in the nanopores.

The origins of plasmon-induced ionic effects seem to be highly related to chemical processes. On one hand, the origin of current increase upon laser illumination need to be distinguished between Joule heating effects or the effect of inducing surface charges. On the other hand, other electrochemical characterizations and delicate high-pressure experiments could be useful for the understanding of noise or nanobubble generations.

High-fidelity Detection of DNA

Better design of optical enhancement. Optical readout is the key feature of our plasmonic nanopores. A “perfect” plasmonic nanopore design will require a well-controlled deposition of dielectric layers. The lack of dielectrics leads to poor ionic performances of the described plasmonic nanopores. Also better control of the dielectric layer may improve the optical performances. For instance, the sharp curvature at the tip of silicon nanocavities becomes blunt after thermal oxidation. Putting layers of dielectrics beneath the metallic nanostructure can cause a red-shift of the optical resonance, while coating the metal surface may dramatically decrease the electro-magnetic field enhancement. Delicate design needs to be introduced towards “perfect” plasmonic nanopore devices.

Synchronize optical spectroscopy with ionic detections. Using metallic nanopores, we have demonstrated the feasibility of ionic detection and SERS measurements. Simultaneous recording both electrical and optical readout is a “must-do” task in the near future. For DNA sequencing, direct base calling using nanopore SERS method will not be straightforward, but may be proven as a valuable alternative method to the (potentially even more challenging) tunneling currents.

Translocation speed control

Control DNA translocation with trapping force. The control of the DNA translocation speed limits the development of the solid-state nanopore. Optical trapping can generate an attractive force (also called gradient force due to the intensity inhomogeneity) and may turn out as an extra degree of freedom to gently manipulate the DNA translocation over time [242]. Plasmonic trapping, based on the excitation of surface plasmons, has been demonstrated to trap or at least capture short ssDNA molecules [243, 244]. Moreover, different length of DNA (20-40 bases) can be differentiated with the changes in resonant frequency, which is in good agreement with one dimensional lattice vibration theory [244]. Our plasmonic nanocavity has been verified to gently manipulate two 22 nm polystyrene beads inside the two hot spots [152]. In our nanopore-in-cavity system, one could implement plasmonic trapping of DNA with controllable physical confinement which is down to several nanometers and similar to the diameter of a solid-state nanopore.

Regulate DNA transport via plasmonic nanovalves. When threading DNA through our pore-in-cavity devices, the devices can be completely switched off upon laser illumination. Therefore, DNA motion is worth to be investigated in the switching conditions. Besides, we can dynamically control the pore lumen upon plasmonic excitation at low powers. Compared to the fixed-size solid-state nanopores, our pore-in-cavity device can measure the DNA translocations with a tunable barrier size, or even laterally tap DNA strands onto the sidewall with size-tunable nanobubbles.

Alternative applications

Also many other applications can be explored using the described metallic nanopore devices.

Plasmonic nanopores as single-molecule sieves. Optofluidic integration has recently attracted a lot of attentions. The combination of integrated optics with nanofluidics on a single chip scale systems offers novel instruments and devices towards a complete lab-on-a-chip. One useful application could be the separation of single molecules. Taking the advantage of our nanovalves which is optically controlled, one can switch off the nanopore valve when threading the molecule through the pore, and move the molecule into separated channels.

Bibliography

[1] Itzhak Bars, John Terning, Farzad Nekoogar, and Lawrence Maxwell Krauss. *Extra dimensions in space and time.* Springer, 2010.

[2] S. W. Hawking. Black hole explosions?, 1974.

[3] Debnath Bhattacharyya, Shashank Singh, and Niraj Satnalika. Nanotechnology , Big things from a Tiny World : a Review. *Sci. Technol.*, 2:29–38, 2009.

[4] `http://www.nano.gov/nanotech-101/special` Accessible on May 10th, 2015.

[5] Richard P Feynman. There's plenty of room at the bottom. *Eng. Sci.*, 23(5):22–36, 1960.

[6] Luis J Garay. Quantum gravity and minimum length. *International Journal of Modern Physics A*, 10(02):145–165, 1995.

[7] Wallace H Coulter. Means for counting particles suspended in a fluid, October 20 1953. US Patent 2,656,508.

[8] Meni Wanunu. Nanopores: A journey towards DNA sequencing. *Phys. Life Rev.*, 9(2):125–158, July 2012.

[9] Elizabeth Pennisi. Search for Pore-fection. *Science*, 336(6801):534–537, 2012.

[10] Farzin Haque, Jinghong Li, Hai-Chen Wu, Xing-Jie Liang, and Peixuan Guo. Solid-State and Biological Nanopore for Real-Time Sensing of Single Chemical and Sequencing of DNA. *Nano Today*, 8(1):56–74, February 2013.

[11] Tom Z Butler, Mikhail Pavlenok, Ian M Derrington, Michael Niederweis, and Jens H Gundlach. Single-molecule DNA detection with an engineered

MspA protein nanopore. *Proc. Natl. Acad. Sci. U. S. A.*, 105(52):20647–20652, December 2008.

[12] David Wendell, Peng Jing, Jia Geng, Varuni Subramaniam, Tae Jin Lee, Carlo Montemagno, and Peixuan Guo. Translocation of double-stranded DNA through membrane-adapted phi29 motor protein nanopores. *Nat. Nanotechnol.*, 4(11):765–772, November 2009.

[13] Jiali Li, Marc Gershow, Derek Stein, Eric Brandin, and J a Golovchenko. DNA molecules and configurations in a solid-state nanopore microscope. *Nat. Mater.*, 2(9):611–615, September 2003.

[14] AJ Storm, JH Chen, XS Ling, HW Zandbergen, and C Dekker. Fabrication of solid-state nanopores with single-nanometre precision. *Nat. Mater.*, 2(8):537–540, 2003.

[15] Meng-Yue Wu, Ralph M M Smeets, Mathijs Zandbergen, Ulrike Ziese, Diego Krapf, Philip E Batson, Nynke H Dekker, Cees Dekker, and Henny W Zandbergen. Control of shape and material composition of solid-state nanopores. *Nano Lett.*, 9(1):479–484, January 2009.

[16] Ke Liu, Jiandong Feng, Andras Kis, and Aleksandra Radenovic. Atomically Thin Molybdenum Disulfide Nanopores with High Sensitivity for DNA Translocation. *ACS Nano*, 8(3):2504–2511, February 2014.

[17] David B. Wells, Maxim Belkin, Jeffrey Comer, and Aleksei Aksimentiev. Assessing graphene nanopores for sequencing DNA. *Nano Lett.*, 12(8):4117–4123, 2012.

[18] Seung Kyu Min, Woo Youn Kim, Yeonchoo Cho, and Kwang S. Kim. Fast DNA sequencing with a graphene-based nanochannel device. *Nat. Nanotechnol.*, 6(February):162–165, February 2011.

[19] Single-layer Mos, Amir Barati Farimani, Kyoungmin Min, and Narayana R Aluru. DNA Base Detection Using a Single-Layer MoS2. *ACS Nano*, 8(8):7914–7922, 2014.

[20] Ryan Rollings, Edward Graef, Nathan Walsh, Santoshi Nandivada, Mourad Benamara, and Jiali Li. The effects of geometry and stability of solid-state nanopores on detecting single DNA molecules. *Nanotechnology*, 26(4):044001, January 2015.

[21] Binquan Luan, Hongbo Peng, Stas Polonsky, Steve Rossnagel, Gustavo Stolovitzky, and Glenn Martyna. Base-By-Base Ratcheting of Single Stranded DNA through a Solid-State Nanopore. *Phys. Rev. Lett.*, 104(23):1–4, June 2010.

[22] Binquan Luan, Gustavo Stolovitzky, and Glenn Martyna. Slowing and controlling the translocation of DNA in a solid-state nanopore. *Nanoscale*, 4(4):1068, 2012.

[23] Adam R Hall, Andrew Scott, Dvir Rotem, Kunal K Mehta, Hagan Bayley, and Cees Dekker. Hybrid pore formation by directed insertion of α-haemolysin into solid-state nanopores. *Nat. Nanotechnol.*, 5(12):874–877, December 2010.

[24] James a. Cracknell, Deanpen Japrung, and Hagan Bayley. Translocating kilobase RNA through the staphylococcal α-hemolysin nanopore. *Nano Lett.*, 13(6):2500–2505, 2013.

[25] J J Kasianowicz, E Brandin, D Branton, and D W Deamer. Characterization of individual polynucleotide molecules using a membrane channel. *Proc. Natl. Acad. Sci. U. S. A.*, 93(24):13770–13773, November 1996.

[26] Amit Meller, Lucas Nivon, and Daniel Branton. Voltage-Driven DNA Translocations through a Nanopore. *Phys. Rev. Lett.*, 86(15):3435–3438, April 2001.

[27] David W Deamer and Daniel Branton. Characterization of nucleic acids by nanopore analysis. *Acc. Chem. Res.*, 35(10):817–825, October 2002.

[28] Spencer Carson, James Wilson, Aleksei Aksimentiev, and Meni Wanunu. Smooth DNA Transport through a Narrowed Pore Geometry. *Biophys. J.*, 107(10):2381–2393, November 2014.

[29] Daniel Fologea, Eric Brandin, James Uplinger, Daniel Branton, and Jiali Li. DNA conformation and base number simultaneously determined in a nanopore. *Electrophoresis*, 28(18):3186–3192, September 2007.

[30] Arnold J Storm, Cornelis Storm, Jianghua Chen, Henny Zandbergen, Jean-François Joanny, and Cees Dekker. Fast DNA translocation through a solid-state nanopore. *Nano Lett.*, 5(7):1193–1197, July 2005.

[31] Peng Chen, Toshiyuki Mitsui, Damon B. Farmer, Jene Golovchenko, Roy G. Gordon, and Daniel Branton. Atomic Layer Deposition to Fine-Tune the Surface Properties and Diameters of Fabricated Nanopores. *Nano Lett.*, 4(7):1333–1337, July 2004.

[32] Joseph Larkin, Robert Henley, David C Bell, Tzahi Cohen-Karni, Jacob K Rosenstein, and Meni Wanunu. Slow DNA Transport through Nanopores in Hafnium Oxide Membranes. *ACS Nano*, 7(11):10121–10128, October 2013.

[33] Meni Wanunu and Amit Meller. Chemically modified solid-state nanopores. *Nano Lett.*, 7(6):1580–1585, June 2007.

[34] Deqiang Wang, Stefan Harrer, Binquan Luan, Gustavo Stolovitzky, Hongbo Peng, and Ali Afzali-Ardakani. Regulating the Transport of DNA through Biofriendly Nanochannels in a Thin Solid Membrane. *Sci. Rep.*, 4:3985, January 2014.

[35] Zhipeng Tang, Bo Lu, Qing Zhao, Jiajun Wang, Kaifu Luo, and Dapeng Yu. Surface Modification of Solid-State Nanopores for Sticky-Free Translocation of Single-Stranded DNA. *Small*, 10(21):4332–4339, 2014.

[36] Brett N Anderson, Murugappan Muthukumar, and Amit Meller. pH Tuning of DNA Translocation Time through Organically Functionalized Nanopores. *ACS Nano*, 7(2):1408–1414, December 2012.

[37] Daniel Fologea, James Uplinger, Brian Thomas, David S McNabb, and Jiali Li. Slowing DNA translocation in a solid-state nanopore. *Nano Lett.*, 5(9):1734–1737, September 2005.

[38] Bo Lu, David P. Hoogerheide, Qing Zhao, Hengbin Zhang, Zhipeng Tang, Dapeng Yu, and Jene a. Golovchenko. Pressure-controlled motion of single polymers through solid-state nanopores. *Nano Lett.*, 13(7):3048–3052, 2013.

[39] David P Hoogerheide, Bo Lu, and Jene a Golovchenko. Pressure-Voltage Trap for DNA near a Solid-State Nanopore. *ACS Nano*, 8(7):7384–7391, June 2014.

[40] Hengbin Zhang, Qing Zhao, Zhipeng Tang, Song Liu, Qingtao Li, Zhongchao Fan, Fuhua Yang, Liping You, Xuemei Li, Jingmin Zhang, and Dapeng Yu. Slowing down DNA translocation through solid-state nanopores by pressure. *Small*, 9(24):4112–4117, 2013.

[41] Meni Wanunu, Will Morrison, Yitzhak Rabin, Alexander Y Grosberg, and Amit Meller. Electrostatic focusing of unlabelled DNA into nanoscale pores using a salt gradient. *Nat. Nanotechnol.*, 5(2):160–165, February 2010.

[42] Yuhui He, Makusu Tsutsui, Ralph H. Scheicher, Chun Fan, Masateru Taniguchi, and Tomoji Kawai. Mechanism of How Salt-Gradient-Induced Charges Affect the Translocation of DNA Molecules through a Nanopore. *Biophys. J.*, 105(3):776–782, August 2013.

[43] Yuhui He, Makusu Tsutsui, Ralph H Scheicher, Fan Bai, Masateru Taniguchi, and Tomoji Kawai. Thermophoretic Manipulation of DNA

Translocation through Nanopores. *ACS Nano*, 7(1):538–546, December 2012.

[44] Gerald M Cherf, Kate R Lieberman, Hytham Rashid, Christopher E Lam, Kevin Karplus, and Mark Akeson. Automated forward and reverse ratcheting of DNA in a nanopore at 5-Åprecision. *Nat. Biotechnol.*, 30(4):344–348, February 2012.

[45] Brett Gyarfas, Felix Olasagasti, Seico Benner, Daniel Garalde, Kate R Lieberman, and Mark Akeson. Mapping the position of DNA polymerase-bound DNA templates in a nanopore at 5 A resolution. *ACS Nano*, 3(6):1457–1466, June 2009.

[46] Elizabeth a Manrao, Ian M Derrington, Andrew H Laszlo, Kyle W Langford, Matthew K Hopper, Nathaniel Gillgren, Mikhail Pavlenok, Michael Niederweis, and Jens H Gundlach. Reading DNA at single-nucleotide resolution with a mutant MspA nanopore and phi29 DNA polymerase. *Nat. Biotechnol.*, 30(1):349–353, March 2012.

[47] Andrew H Laszlo, Ian M Derrington, Brian C Ross, Henry Brinkerhoff, Andrew Adey, Ian C Nova, Jonathan M Craig, Kyle W Langford, Jenny Mae Samson, Riza Daza, Kenji Doering, Jay Shendure, and Jens H Gundlach. Decoding long nanopore sequencing reads of natural DNA. *Nat. Biotechnol.*, 32(1):829–833, June 2014.

[48] Andrew H Laszlo, Ian M Derrington, Henry Brinkerhoff, Kyle W Langford, Ian C Nova, Jenny Mae Samson, Joshua J Bartlett, Mikhail Pavlenok, and Jens H Gundlach. Detection and mapping of 5-methylcytosine and 5-hydroxymethylcytosine with nanopore MspA. *Proc. Natl. Acad. Sci. U. S. A.*, 110(47):18904–18909, October 2013.

[49] Jacob Schreiber, Zachary L Wescoe, Robin Abu-Shumays, John T Vivian, Baldandorj Baatar, Kevin Karplus, and Mark Akeson. Error rates for nanopore discrimination among cytosine, methylcytosine, and hydroxymethylcytosine along individual DNA strands. *Proc. Natl Acad. Sci. USA*, 110(47):18910–18915, 2013.

[50] Robert K. Neely, Jochem Deen, and Johan Hofkens. Optical mapping of DNA: Single-molecule-based methods for mapping genomes. *Biopolymers*, 95(5):298–311, 2011.

[51] Robert K. Neely, Peter Dedecker, Jun-ichi Hotta, Giedré Urbanavičiuté, Saulius Klimašauskas, and Johan Hofkens. DNA fluorocode: A single molecule, optical map of DNA with nanometre resolution. *Chem. Sci.*, 1(4):453, 2010.

[52] Ossama N Assad, Nicolas Di Fiori, Allison H Squires, and Amit Meller. Two Color DNA Barcode Detection in Photoluminescence Suppressed Silicon Nitride Nanopores. *Nano Lett.*, 15(1):745–752, 2015.

[53] `http://www.nabsys.com/Nabsys/media/Nabsys/Files/ASHG2012-structural-variants_1.pdf?ext=.pdf` Accessible on May 10th, 2015.

[54] Alon Singer, Meni Wanunu, Will Morrison, Heiko Kuhn, Maxim Frank-Kamenetskii, and Amit Meller. Nanopore based sequence specific detection of duplex DNA for genomic profiling. *Nano Lett.*, 10(2):738–742, February 2010.

[55] Alon Singer, Srinivas Rapireddy, Danith H. Ly, and Amit Meller. Electronic barcoding of a viral gene at the single-molecule level. *Nano Lett.*, 12(3):1722–1728, 2012.

[56] James Clarke, H.C. Wu, Lakmal Jayasinghe, Alpesh Patel, Stuart Reid, and Hagan Bayley. Continuous base identification for single-molecule nanopore DNA sequencing. *Nat. Nanotechnol.*, 4(4):265–270, 2009.

[57] Erik C Yusko, Jay M Johnson, Sheereen Majd, Panchika Prangkio, Ryan C Rollings, Jiali Li, Jerry Yang, and Michael Mayer. Controlling protein translocation through nanopores with bio-inspired fluid walls. *Nat. Nanotechnol.*, 6(1):253–260, February 2011.

[58] Joseph E Reiner, Arvind Balijepalli, Joseph W F Robertson, Bryon S Drown, Daniel L Burden, and John J Kasianowicz. The effects of diffusion on an exonuclease\nanopore-based DNA sequencing engine. *J. Chem. Phys.*, 137(21):214903, December 2012.

[59] Winston Timp, Allison M. Nice, Edward M. Nelson, Volker Kurz, Kim McKelvey, and Gregory Timp. Think Small: Nanopores for Sensing and Synthesis. *IEEE Access*, 2:1396–1408, 2014.

[60] Kimberly Venta, Gabriel Shemer, and Matthew Puster. Differentiation of Short Single-Stranded DNA Homopolymers in Solid-State Nanopores. *ACS Nano*, 7(5):4629–4636, 2013.

[61] I. M. Derrington, T. Z. Butler, M. D. Collins, E. Manrao, M. Pavlenok, M. Niederweis, and J. H. Gundlach. Nanopore DNA sequencing with MspA. *Proc. Natl. Acad. Sci. U. S. A.*, 107(37), August 2010.

[62] Makusu Tsutsui, Masateru Taniguchi, Kazumichi Yokota, and Tomoji Kawai. Identifying single nucleotides by tunnelling current. *Nat. Nanotechnol.*, 5(4):286–290, April 2010.

[63] Shuo Huang, Jin He, Shuai Chang, Peiming Zhang, Feng Liang, Shengqin Li, Michael Tuchband, Alexander Fuhrmann, Robert Ros, and Stuart Lindsay. Identifying single bases in a DNA oligomer with electron tunnelling. *Nat. Nanotechnol.*, 5(12):868–873, November 2010.

[64] Aleksandar P. Ivanov, Emanuele Instuli, Catriona McGilvery, Geoff Baldwin, David W. McComb, Tim Albrecht, and Joshua B. Edel. DNA Tunneling Detector Embedded in a Nanopore. *Nano Lett.*, 11(1):279–285, December 2011.

[65] Axel Fanget, Floriano Traversi, Sergey Khlybov, Pierre Granjon, Arnaud Magrez, László Forró, and Aleksandra Radenovic. Nanopore integrated nanogaps for DNA detection. *Nano Lett.*, 14(1):244–249, 2014.

[66] Pei Pang, BA Ashcroft, Weisi Song, and Peiming Zhang. Fixed Gap Tunnel Junction for Reading DNA Nucleotides. *ACS Nano*, 8(12):11994–12003, 2014.

[67] David Rodriguez-Larrea and Hagan Bayley. Multistep protein unfolding during nanopore translocation. *Nat. Nanotechnol.*, 8:288–295, March 2013.

[68] Christian B Rosen, David Rodriguez-Larrea, and Hagan Bayley. Single-molecule site-specific detection of protein phosphorylation with a nanopore. *Nat. Biotechnol.*, 32:179–181, January 2014.

[69] Jeff Nivala, Douglas B Marks, and Mark Akeson. Unfoldase-mediated protein translocation through an α-hemolysin nanopore. *Nat. Biotechnol.*, 31(1):247–250, February 2013.

[70] Misha Soskine, Annemie Biesemans, Marc De Maeyer, and Giovanni Maglia. Tuning the size and properties of ClyA nanopores assisted by directed evolution. *J. Am. Chem. Soc.*, 135(36):13456–13463, 2013.

[71] Misha Soskine, Annemie Biesemans, Benjamien Moeyaert, Stephen Cheley, Hagan Bayley, and Giovanni Maglia. An Engineered ClyA Nanopore Detects Folded Target Proteins by Selective External Association and Pore Entry. *Nano Lett.*, 12(9):4895–4900, August 2012.

[72] Veerle Van Meervelt, Misha Soskine, and Giovanni Maglia. Detection of Two Isomeric Binding Configurations in a Protein-Aptamer Complex with a Biological Nanopore. *ACS Nano*, 8(12):12826–12835, 2014.

[73] Calin Plesa, Stefan W. Kowalczyk, Ruben Zinsmeester, Alexander Y. Grosberg, Yitzhak Rabin, and Cees Dekker. Fast translocation of proteins through solid state nanopores. *Nano Lett.*, 13(2):658–663, 2013.

[74] Jacob K. Rosenstein, Meni Wanunu, Christopher A. Merchant, Marija Drndić, and Kenneth L. Shepard. Integrated nanopore sensing platform with sub-microsecond temporal resolution. *Nat. Methods*, 9:487–492, 2012.

[75] Nicolas Di Fiori, Allison Squires, Daniel Bar, Tal Gilboa, Theodore D. Moustakas, and Amit Meller. Optoelectronic control of surface charge and translocation dynamics in solid-state nanopores. *Nat. Nanotechnol.*, 8:946–951, November 2013.

[76] William L Barnes, Alain Dereux, and Thomas W Ebbesen. Surface plasmon subwavelength optics. *Nature*, 424:824–830, 2003.

[77] Richard L McCreery. *Raman spectroscopy for chemical analysis*, volume 225. John Wiley & Sons, 2005.

[78] Masatoshi Osawa, Naoki Matsuda, Katsumasa Yoshii, and Isamu Uchida. Charge transfer resonance Raman process in surface-enhanced Raman scattering from p-aminothiophenol adsorbed on silver: Herzberg-Teller contribution. *J. Phys. Chem.*, 98:12702–12707, 1994.

[79] M Fleischmann, P J Hendra, and A J McQuillan. Raman spectra of pyridine adsorbed at a silver electrode. *Chem. Phys. Lett.*, 26:163–166, 1974.

[80] Lukas Novotny and Niek van Hulst. Antennas for light. *Nat. Photonics*, 5(2):83–90, February 2011.

[81] Jiaqi Li, Chang Chen, Hilde Jans, Xiumei Xu, Niels Verellen, Ingrid Vos, Yasuaki Okumura, Victor V. Moshchalkov, Liesbet Lagae, and Pol Van Dorpe. 300 mm Wafer-level, ultra-dense arrays of Au-capped nanopillars with sub-10 nm gaps as reliable SERS substrates. *Nanoscale*, 6:12391–12396, 2014.

[82] Christian Steuwe, Clemens F. Kaminski, Jeremy J. Baumberg, and Sumeet Mahajan. Surface enhanced coherent anti-stokes raman scattering on nanostructured gold surfaces. *Nano Lett.*, 11(12):5339–5343, 2011.

[83] Arif E Cetin, Ahmet F Coskun, Betty C Galarreta, Min Huang, David Herman, Aydogan Ozcan, and Hatice Altug. Handheld high-throughput plasmonic biosensor using computational on-chip imaging. *Light Sci. Appl.*, 3(1):e122, 2014.

[84] Chang Chen. *Plasmonic nanopores for direct molecular identification.* PhD thesis, KU Leuven, 2011.

[85] Eric C Le Ru and Pablo G Etchegoin. Single-molecule surface-enhanced Raman spectroscopy. *Annu. Rev. Phys. Chem.*, 63:65–87, May 2012.

[86] S Kumar and S Cherukulappurath. Millimeter-sized Suspended Plasmonic Nanohole Arrays for Surface-Tension-Driven Flow-through SERS. *Chem. Mater.*, 26(22):6523–6530, 2014.

[87] Michael P Cecchini, Aeneas Wiener, Vladimir Turek, Hyangah Chon, Sangyeop Lee, Aleksandar P Ivanov, David W McComb, Jaebum Choo, Tim Albrecht, Stefan a Maier, and Joshua B Edel. Rapid Ultra-Sensitive Single Particle Surface Enhanced Raman Spectroscopy using Metallic Nanopores. *Nano Lett.*, 13(10):4602–4609, 2013.

[88] Kuan Yu Chen, An Ting Lee, Chia Chun Hung, Jer Shing Huang, and Ya Tang Yang. Transport and trapping in two-dimensional nanoscale plasmonic optical lattice. *Nano Lett.*, 13(9):4118–4122, 2013.

[89] Chang Chen, James Andell Hutchison, Pol Van Dorpe, Ronald Kox, Iwijn De Vlaminck, Hiroshi Uji-I, Johan Hofkens, Liesbet Lagae, Guido Maes, and Gustaaf Borghs. Focusing plasmons in nanoslits for surface-enhanced Raman scattering. *Small*, 5(24):2876–2882, December 2009.

[90] Chang. Chen, Jian. Ye, Yi. Li, Liesbet. Lagae, Tim. Stakenborg, and Pol. Van Dorpe. Detection of DNA Bases and Oligonucleotides in Plasmonic Nanoslits Using Fluidic SERS. *IEEE J. Sel. Top. Quantum Electron.*, 19(3):4600707 – 4600707, 2012.

[91] Albert Polman. Solar steam nanobubbles. *ACS Nano*, 7(1):15–18, 2013.

[92] David Erickson, David Sinton, and Demetri Psaltis. Optofluidics for energy applications. *Nat. Photonics*, 5(10):583–590, September 2011.

[93] Mark L. Brongersma, Naomi J. Halas, and Peter Nordlander. Plasmon-induced hot carrier science and technology. *Nat. Nanotechnol.*, 10(1):25–34, January 2015.

[94] Ronald Kox. *Nanopore-based Nanofluidic Transistors.* PhD thesis, KU Leuven, 2010.

[95] K Malachowski, R Verbeeck, T Dupont, C Chen, Y Li, S Musa, T Stakenborg, D Tezcan, and P Van Dorpe. Wafer Scale Processing of Plasmonic Nanoslit Arrays in 200mm CMOS Fab Environment. *ECS Trans.*, 50(12):413–422, 2013.

[96] F Laermer and A Schilp. United states patent 5501893, 1996.

[97] Ken Healy, Birgitta Schiedt, and Alan P Morrison. Solid-state nanopore technologies for nanopore-based DNA analysis. *Nanomedicine*, 2(6):875–897, December 2007.

[98] M Rhee and M.A. Burns. Nanopore sequencing technology: research trends and applications. *Trends Biotechnol.*, 24(12):580–586, 2006.

[99] Minsoung Rhee and Mark a Burns. Nanopore sequencing technology: nanopore preparations. *Trends Biotechnol.*, 25(4):174–81, April 2007.

[100] Sang Ryul Park, Hongbo Peng, and Xinsheng S Ling. Fabrication of nanopores in silicon chips using feedback chemical etching. *Small*, 3(1):116–119, January 2007.

[101] Z Siwy and A Fuliński. Fabrication of a synthetic nanopore ion pump. *Phys. Rev. Lett.*, 89:198103, 2002.

[102] Lindsay T Sexton, Lloyd P Horne, and Charles R Martin. Developing synthetic conical nanopores for biosensing applications. *Mol. Biosyst.*, 3(10):667–685, October 2007.

[103] Zhipeng Huang, Xuanxiong Zhang, Manfred Reiche, Lifeng Ltu, Woo Lee, Tomohiro Shimizu, Stephan Senz, and Ulrich Gösele. Extended arrays of vertically aligned Sub-10 nm diameter [100] Si nanowires by metal-assisted chemical etching. *Nano Lett.*, 8(9):3046–3051, 2008.

[104] Teena James, Yevgeniy V Kalinin, Chih-Chieh Chan, Jatinder S Randhawa, Mikhail Gaevski, and David H Gracias. Voltage-gated ion transport through semiconducting conical nanopores formed by metal nanoparticle-assisted plasma etching. *Nano Lett.*, 12(7):3437–3442, July 2012.

[105] H Chang, F. Kosari, G. Andreadakis, MA Alam, G. Vasmatzis, and R. Bashir. DNA-mediated fluctuations in ionic current through silicon oxide nanopore channels. *Nano Lett.*, 4(8):1551–1556, 2004.

[106] Ruoshan Wei, Daniel Pedone, Andreas Zürner, Markus Döblinger, and Ulrich Rant. Fabrication of Metallized Nanopores in Silicon Nitride Membranes for Single-Molecule Sensing. *Small*, 6(13):1406–1414, July 2010.

[107] Mariam Ayub, Aleksandar Ivanov, Jongin Hong, Phillip Kuhn, Emanuele Instuli, Joshua B Edel, and Tim Albrecht. Precise electrochemical fabrication of sub-20 nm solid-state nanopores for single-molecule biosensing. *J. Phys. Condens. Matter*, 22(45):454128, November 2010.

[108] Ronald Kox, Chang Chen, Guido Maes, Liesbet Lagae, and Gustaaf Borghs. Shrinking solid-state nanopores using electron-beam-induced deposition. *Nanotechnology*, 20(11):115302, March 2009.

[109] Ronald Kox, Stella Deheryan, Chang Chen, Nima Arjmandi, Liesbet Lagae, and Gustaaf Borghs. Local solid-state modification of nanopore surface charges. *Nanotechnology*, 21(33):335703, August 2010.

[110] Anmiv S Prabhu, Kevin J Freedman, Joseph W F Robertson, Zhorro Nikolov, John J Kasianowicz, and Min Jun Kim. SEM-induced shrinking of solid-state nanopores for single molecule detection. *Nanotechnology*, 22(42):425302, 2011.

[111] Miao Zhang, Torsten Schmidt, Fatemeh Sangghaleh, Niclas Roxhed, Ilya Sychugov, and Jan Linnros. Oxidation of nanopores in a silicon membrane: self-limiting formation of sub-10 nm circular openings. *Nanotechnology*, 25(35):355302, 2014.

[112] Meng-Yue Wu, Ping Chen, Ulrike Ziese, Paul F a Alkemade, Huub W M Salemink, and Henny W Zandbergen. TEM study of locally coated nanopore fabricated by ion-beam-induced deposition in a thin membrane. *Micron*, 41(6):609–614, August 2010.

[113] Meng-Yue Wu, Diego Krapf, Mathijs Zandbergen, Henny Zandbergen, and Philip E. Batson. Formation of nanopores in a SiN/SiO2 membrane with an electron beam. *Appl. Phys. Lett.*, 87(11):113106, 2005.

[114] Chang Chen, Niels Verellen, Kristof Lodewijks, Liesbet Lagae, Guido Maes, Gustaaf Borghs, and Pol Van Dorpe. Groove-gratings to optimize the electric field enhancement in a plasmonic nanoslit-cavity. *J. Appl. Phys.*, 108(3):034319, 2010.

[115] Giuseppe Tarabella, Clara Santato, Sang Yoon Yang, Salvatore Iannotta, George G. Malliaras, and Fabio Cicoira. Effect of the gate electrode on the response of organic electrochemical transistors. *Appl. Phys. Lett.*, 97, 2010.

[116] Daniel C Harris. *Quantitative Chemical Analysis*, volume 42. W. H. Freeman; Eighth Edition edition (May 15, 2010), 2007.

[117] R M M Smeets, N H Dekker, and C Dekker. Low-frequency noise in solid-state nanopores. *Nanotechnology*, 20(9):095501, March 2009.

[118] R M M Smeets, U F Keyser, N H Dekker, and C Dekker. Noise in solid-state nanopores. *Proc. Natl. Acad. Sci. U. S. A.*, 105(2):417–421, January 2008.

[119] Bert Sakmann and Erwin Neher. *Single-channel recording.* Springer Science & Business Media, 2009.

[120] Stefan W Kowalczyk, David B Wells, Aleksei Aksimentiev, and Cees Dekker. Slowing down DNA Translocation through a Nanopore in Lithium Chloride. *Nano Lett.*, 12(2):1038–1044, January 2012.

[121] `http://www.comsol.com/comsol-multiphysics` Accessible on May 10th, 2015.

[122] Juan Liu, Maksim Kvetny, Jingyu Feng, Dengchao Wang, Baohua Wu, Warren Brown, and Gangli Wang. Surface Charge Density Determination of Single Conical Nanopores Based on Normalized Ion Current Rectification. *Langmuir*, 28(2):1588–1595, December 2011.

[123] R.M.M. Smeets, U.F. Keyser, D. Krapf, M.Y. Wu, H. Nynke, and C. Dekker. Salt dependence of ion transport and DNA translocation through solid-state nanopores. *Nano Lett.*, 6(1):89–95, 2006.

[124] Aigars Piruska, Sean Branagan, Donald M Cropek, Jonathan V Sweedler, and Paul W Bohn. Electrokinetically driven fluidic transport in integrated three-dimensional microfluidic devices incorporating gold-coated nanocapillary array membranes. *Lab Chip*, 8(10):1625–1631, October 2008.

[125] Aigars Piruska, Sean P Branagan, Alexandra B Minnis, Zhen Wang, Donald M Cropek, Jonathan V Sweedler, and Paul W Bohn. Electrokinetic control of fluid transport in gold-coated nanocapillary array membranes in hybrid nanofluidic-microfluidic devices. *Lab Chip*, 10(10):1237–44, May 2010.

[126] Carlos Escobedo, Alexandre G Brolo, Reuven Gordon, and David Sinton. Optofluidic Concentration: Plasmonic Nanostructure as Concentrator and Sensor. *Nano Lett.*, 12(3):1592–1596, February 2012.

[127] Shailabh Kumar, Nathan J. Wittenberg, and Sang Hyun Oh. Nanopore-induced spontaneous concentration for optofluidic sensing and particle assembly. *Anal. Chem.*, 85(2):971–977, 2013.

[128] Peng Gao and CR Martin. Voltage Charging Enhances Ionic Conductivity in Gold Nanotube Membranes. *ACS Nano*, 8(8):8266–8272, 2014.

[129] Ruoshan Wei, Volker Gatterdam, Ralph Wieneke, Robert Tampé, and Ulrich Rant. Stochastic sensing of proteins with receptor-modified solid-state nanopores. *Nat. Nanotechnol.*, 7(March):257–263, March 2012.

[130] Harold Kwok, Matthew Waugh, José Bustamante, Kyle Briggs, and Vincent Tabard-Cossa. Long Passage Times of Short ssDNA Molecules through Metallized Nanopores Fabricated by Controlled Breakdown. *Adv. Funct. Mater.*, 24(48):7745–7753, 2014.

[131] Yi Li, Chang Chen, Sarp Kerman, Pieter Neutens, Liesbet Lagae, Guido Groeseneken, Tim Stakenborg, and Pol Van Dorpe. Harnessing Plasmon Induced Ionic Noise in Metallic Nanopores. *Nano Lett.*, 13(4):1724–1729, March 2013.

[132] Stefan W Kowalczyk, Alexander Y Grosberg, Yitzhak Rabin, and Cees Dekker. Modeling the conductance and DNA blockade of solid-state nanopores. *Nanotechnology*, 22(31):315101, July 2011.

[133] Weihua Guan and Mark a Reed. Electric field modulation of the membrane potential in solid-state ion channels. *Nano Lett.*, 12(12):6441–6447, December 2012.

[134] Takumi Sannomiya, Harald Dermutz, Christian Hafner, Janos Vörös, and Andreas B Dahlin. Electrochemistry on a localized surface plasmon resonance sensor. *Langmuir*, 26(10):7619–7626, May 2010.

[135] Matthew Pevarnik, Ken Healy, Matthew Davenport, Joseph Yen, and Zuzanna S Siwy. A hydrophobic entrance enhances ion current rectification and induces dewetting in asymmetric nanopores. *Analyst*, 137(13):2944–2950, March 2012.

[136] Mingkan Zhang, Ye Ai, Ashutosh Sharma, Sang W Joo, Dong-Soo Kim, and Shizhi Qian. Electrokinetic particle translocation through a nanopore containing a floating electrode. *Electrophoresis*, 32(14):1864–1874, July 2011.

[137] J Wang, AJ Davenport, HS Isaacs, and BM Ocko. Surface Charge-Induced Ordering of the Au (111) Surface. *Science*, 255(5050):1416–1418, 1992.

[138] Meni Wanunu, Devora Cohen-Karni, R.R. Robert R Johnson, Lauren Fields, Jack Benner, Neil Peterman, Yu Zheng, Michael L M.L. Michael L Klein, and Marija Drndic. Discrimination of Methylcytosine from Hydroxymethylcytosine in DNA Molecules. *J. Am. Chem. Soc.*, 133(3):486–492, December 2011.

[139] Matthew Pevarnik, Ken Healy, Maria Eugenia Toimil-Molares, Alan Morrison, Sonia E Létant, and Zuzanna S Siwy. Polystyrene Particles Reveal Pore Substructure As They Translocate. *ACS Nano*, 6(8):7295–7302, July 2012.

[140] B.M. Venkatesan, A.B. Shah, J.M. Zuo, and Rashid Bashir. DNA sensing using nanocrystalline surface-enhanced Al2O3 nanopore sensors. *Adv. Funct. Mater.*, 20:1266–1275, 2010.

[141] Kyle N Knust, Dzmitry Hlushkou, Robbyn K Anand, Ulrich Tallarek, and Richard M Crooks. Electrochemically mediated seawater desalination. *Angew. Chem., Int. Ed.*, 52(31):8107–8110, July 2013.

[142] Gregory F Schneider, Stefan W Kowalczyk, Victor E Calado, Gregory Pandraud, Henny W Zandbergen, Lieven M K Vandersypen, and Cees Dekker. DNA translocation through graphene nanopores. *Nano Lett.*, 10(8):3163–3167, August 2010.

[143] Vincent Tabard-Cossa, Dhruti Trivedi, Matthew Wiggin, Nahid N Jetha, and Andre Marziali. Noise analysis and reduction in solid-state nanopores. *Nanotechnology*, 18(30):305505, August 2007.

[144] Michael Zwolak, Johan Lagerqvist, and Massimiliano Di Ventra. Quantized Ionic Conductance in Nanopores. *Phys. Rev. Lett.*, 103(12):1–4, September 2009.

[145] Matthew R. Powell, Ivan Vlassiouk, Craig Martens, and Zuzanna S. Siwy. Nonequilibrium 1/f Noise in Rectifying Nanopores. *Phys. Rev. Lett.*, 103(24):9–12, December 2009.

[146] Sergey Bezrukov and John Kasianowicz. Current noise reveals protonation kinetics and number of ionizable sites in an open protein ion channel. *Phys. Rev. Lett.*, 70(15):2352–2355, 1993.

[147] C. Tasserit, A. Koutsioubas, D. Lairez, G. Zalczer, and M. C. Clochard. Pink Noise of Ionic Conductance through Single Artificial Nanopores Revisited. *Phys. Rev. Lett.*, 105(26):1–4, December 2010.

[148] Z. Siwy and a. Fuliński. Origin of 1/f^{α} Noise in Membrane Channel Currents. *Phys. Rev. Lett.*, 89(15):1–4, September 2002.

[149] David P. Hoogerheide, Slaven Garaj, and Jene a. Golovchenko. Probing Surface Charge Fluctuations with Solid-State Nanopores. *Phys. Rev. Lett.*, 102(25), June 2009.

[150] Philip S. Waggoner, Aaron T. Kuan, Stas Polonsky, Hongbo Peng, and Stephen M. Rossnagel. Increasing the speed of solid-state nanopores. *J. Vac. Sci. Technol. B*, 29(3):032206, 2011.

[151] Cees Dekker. Solid-state nanopores. *Nat. Nanotechnol.*, 2(4):209–215, April 2007.

[152] Chang Chen, Mathieu L. Juan, Yi Li, Guido Maes, Gustaaf Borghs, Pol Van Dorpe, and Romain Quidant. Enhanced optical trapping and arrangement of nano-objects in a plasmonic nanocavity. *Nano Lett.*, 12(1):125–132, 2012.

[153] Takahito Ohshiro, Kazuki Matsubara, Makusu Tsutsui, Masayuki Furuhashi, Masateru Taniguchi, and Tomoji Kawai. Single-molecule electrical random resequencing of DNA and RNA. *Sci. Rep.*, 2:501, January 2012.

[154] Kee-Hyun Paik, Yang Liu, Vincent Tabard-Cossa, Matthew J Waugh, David E Huber, J Provine, Roger T Howe, Robert W Dutton, and Ronald W Davis. Control of DNA Capture by Nanofluidic Transistors. *ACS Nano*, 6(8):6767–6775, July 2012.

[155] Zhijun Jiang and Derek Stein. Electrofluidic gating of a chemically reactive surface. *Langmuir*, 26(11):8161–8173, June 2010.

[156] Sung-Wook Nam, Michael J Rooks, Ki-Bum Kim, and Stephen M Rossnagel. Ionic field effect transistors with sub-10 nm multiple nanopores. *Nano Lett.*, 9(5):2044–2048, May 2009.

[157] Guillaume Chansin, Rafael Mulero, Jongin Hong, Min Jun Kim, Andrew DeMello, and Joshua B Edel. Single-molecule spectroscopy using nanoporous membranes. *Nano Lett.*, 7(9):2901–2906, September 2007.

[158] François Mavré, Robbyn K Anand, Derek R Laws, Kwok-Fan Chow, Byoung-Yong Chang, John a Crooks, and Richard M Crooks. Bipolar Electrodes: A Useful Tool for Concentration, Separation, and Detection of Analytes in Microelectrochemical Systems. *Anal. Chem.*, pages 8766–8774, September 2010.

[159] Gabriel Loget, Dodzi Zigah, and Laurent Bouffier. Bipolar Electrochemistry: from materials science to motion and beyond. *Acc. Chem. Res.*, pages 2513–2523, 2013.

[160] Matthew R Powell, Michael Sullivan, Ivan Vlassiouk, Dragos Constantin, Olivier Sudre, Craig C Martens, Robert S Eisenberg, and Zuzanna S Siwy. Nanoprecipitation-assisted ion current oscillations. *Nat. Nanotechnol.*, 3:51–57, January 2008.

[161] Chang Chen, Francesca Clemente, Ronald Kox, Liesbet Lagae, Guido Maes, Gustaaf Borghs, and Pol Van Dorpe. Raman scattered photon transmission through a single nanoslit. *Appl. Phys. Lett.*, 96(6):061108, 2010.

[162] Kristof Lodewijks, Willem Van Roy, Gustaaf Borghs, Liesbet Lagae, and Pol Van Dorpe. Boosting the figure-of-merit of LSPR-based refractive index sensing by phase-sensitive measurements. *Nano Lett.*, 12(3):1655–1659, 2012.

[163] Jon S Donner, Guillaume Baffou, David McCloskey, and Romain Quidant. Plasmon-assisted optofluidics. *ACS Nano*, 5(7):5457–5462, July 2011.

[164] G. Baffou, R. Quidant, and C. Girard. Heat generation in plasmonic nanostructures: Influence of morphology. *Appl. Phys. Lett.*, 94(15):153109, 2009.

[165] Guillaume Baffou, Christian Girard, and Romain Quidant. Mapping Heat Origin in Plasmonic Structures. *Phys. Rev. Lett.*, 104(13):1–4, April 2010.

[166] Suljo Linic, Phillip Christopher, and David B Ingram. Plasmonic-metal nanostructures for efficient conversion of solar to chemical energy. *Nat. Mater.*, 10(12):911–921, December 2011.

[167] Scott C. Warren and Elijah Thimsen. Plasmonic solar water splitting. *Energy Environ. Sci.*, 5(1):5133, 2012.

[168] Sergio Navalon, Maykel de Miguel, Roberto Martin, Mercedes Alvaro, and Hermenegildo Garcia. Enhancement of the catalytic activity of supported gold nanoparticles for the Fenton reaction by light. *J. Am. Chem. Soc.*, 133(7):2218–2226, February 2011.

[169] M. Jamal Deen, S. L. Rumyantsev, and M. Schroter. On the origin of 1/f noise in polysilicon emitter bipolar transistors. *J. Appl. Phys.*, 85(2):1192, 1999.

[170] Wenbo Hou and Stephen B. Cronin. A review of surface plasmon resonance-enhanced photocatalysis. *Adv. Funct. Mater.*, 23(13):1612–1619, 2013.

[171] Marcel Pourbaix. *Atlas of electrochemical equilibria in aqueous solutions.* National Association of Corrosion Engineers, 1974.

[172] S J Heerema, G F Schneider, M Rozemuller, L Vicarelli, H W Zandbergen, and C Dekker. 1/f noise in graphene nanopores. *Nanotechnology*, 26(7):74001, 2015.

[173] Ilwhan Oh, Joohong Kye, and Seongpil Hwang. Enhanced photoelectrochemical hydrogen production from silicon nanowire array photocathode. *Nano Lett.*, 12(1):298–302, 2012.

[174] Chong Liu, Jinyao Tang, Hao Ming Chen, Bin Liu, and Peidong Yang. A Fully Integrated Nanosystem of Semiconductor Nanowires for Direct Solar Water Splitting. *Nano Lett.*, 13(1):2989–2992, 2013.

[175] Dong Liu, Leilei Li, Yang Gao, Chengming Wang, Jun Jiang, and Yujie Xiong. The Nature of Photocatalytic “Water Splitting” on Silicon Nanowires. *Angew. Chem. Int. Ed.*, 127(10):3023–3028, 2015.

[176] N. R. Mathews, P. J. Sebastian, X. Mathew, and V. Agarwal. Photoelectrochemical characterization of porous Si. *Int. J. Hydrogen Energy*, 28:629–632, 2003.

[177] Stephen E. Fosdick, Kyle N. Knust, Karen Scida, and Richard M. Crooks. Bipolar electrochemistry. *Angew. Chem. Int. Ed.*, 52(40):10438–10456, 2013.

[178] François Mavré, Kwok-Fan Chow, Eoin Sheridan, Byoung-Yong Chang, John a. Crooks, and Richard M. Crooks. A Theoretical and Experimental Framework for Understanding Electrogenerated Chemiluminescence (ECL) Emission at Bipolar Electrodes. *Anal. Chem.*, 81(15):6218–6225, August 2009.

[179] Stephen E Fosdick and Richard M Crooks. Bipolar electrodes for rapid screening of electrocatalysts. *J. Am. Chem. Soc.*, 134(2):863–866, January 2012.

[180] Robbyn K Perdue, Derek R Laws, Dzmitry Hlushkou, Ulrich Tallarek, and Richard M Crooks. Bipolar electrode focusing: the effect of current and electric field on concentration enrichment. *Anal. Chem.*, 81(24):10149–10155, December 2009.

[181] Christian Ulrich, Olof Andersson, Leif Nyholm, and Fredrik Björefors. Formation of molecular gradients on bipolar electrodes. *Angew. Chem., Int. Ed.*, 47(16):3034–3036, January 2008.

[182] C Chad Harrell, Punit Kohli, Zuzanna Siwy, and Charles R Martin. DNA-nanotube artificial ion channels. *J. Am. Chem. Soc.*, 126(48):15646–15647, December 2004.

[183] Meni Wanunu, Tali Dadosh, Vishva Ray, Jingmin Jin, Larry McReynolds, and Marija Drndić. Rapid electronic detection of probe-specific microRNAs using thin nanopore sensors. *Nat. Nanotechnol.*, 5(11):807–814, October 2010.

[184] Chang Chen, James Andell Hutchison, Francesca Clemente, Ronald Kox, Hiroshi Uji-I, Johan Hofkens, Liesbet Lagae, Guido Maes, Gustaaf Borghs, and Pol Van Dorpe. Direct evidence of high spatial localization of hot spots in surface-enhanced Raman scattering. *Angew. Chem., Int. Ed.*, 48(52):9932–9935, January 2009.

[185] Emiliano Cortés, Pablo G PG Etchegoin, Eric C Le Ru, Alejandro Fainstein, María E Vela, Roberto C Salvarezza, E Cortés, and EC Le Ru. Monitoring the Electrochemistry of Single Molecules by Surface-Enhanced Raman Spectroscopy. *J. Am. Chem. Soc.*, 132(51):18034–18037, December 2010.

[186] AJ Wilson and KA Willets. Visualizing site-specific redox potentials on the surface of plasmonic nanoparticle aggregates with super-localization SERS microscopy. *Nano Lett.*, 14(2):939–945, 2014.

[187] Li Cui, Bo Liu, David Vonlanthen, Marcel Mayor, Yongchun Fu, Jian-Feng Li, and Thomas Wandlowski. In situ gap-mode Raman spectroscopy on single-crystal Au(100) electrodes: tuning the torsion angle of 4,4'-biphenyldithiols by an electrochemical gate field. *J. Am. Chem. Soc.*, 133(19):7332–7335, May 2011.

[188] Bo Liu, Alfred Blaszczyk, Marcel Mayor, and Thomas Wandlowski. Redox-switching in a viologen-type adlayer: an electrochemical shell-isolated nanoparticle enhanced raman spectroscopy study on Au (111)-(1× 1) single crystal electrodes. *ACS Nano*, 5(7):5662–5672, 2011.

[189] De-Yin Wu, Jian-Feng Li, Bin Ren, and Zhong-Qun Tian. Electrochemical surface-enhanced Raman spectroscopy of nanostructures. *Chem. Soc. Rev.*, 37(5):1025–1041, May 2008.

[190] Fan Ni, Helena Feng, Lo Gorton, and TM Cotton. Electrochemical and SERS studies of chemically modified electrodes: Nile Blue A, a mediator for NADH oxidation. *Langmuir*, 6(1):66–73, 1990.

[191] Aurélie Bouchet, Emeline Descamps, Pascal Mailley, Thierry Livache, François Chatelain, and Vincent Haguet. Contactless electrofunctionalization of a single pore. *Small*, 5(20):2297–303, October 2009.

[192] Jie Liu, Clément Hébert, Pascale Pham, Fabien Sauter-Starace, Vincent Haguet, Thierry Livache, and Pascal Mailley. Electrochemically induced maskless metal deposition on micropore wall. *Small*, 8(9):1345–1349, 2012.

[193] Jie Liu, Pascale Pham, Vincent Haguet, Fabien Sauter-Starace, Loïc Leroy, André Roget, Emeline Descamps, Aurélie Bouchet, Arnaud Buhot, Pascal Mailley, and Thierry Livache. Polarization-induced local pore-wall functionalization for biosensing: From micropore to nanopore. *Anal. Chem.*, 84(7):3254–3261, 2012.

[194] Stephen E Fosdick, John a Crooks, Byoung-Yong Chang, and Richard M Crooks. Two-dimensional bipolar electrochemistry. *J. Am. Chem. Soc.*, 132(27):9226–9227, July 2010.

[195] Sean P Branagan and Paul W Bohn. Plasmonic response of electrified metal-liquid interfaces during faradaic and non-faradaic reactions by enhanced optical transmission. *Analyst*, 137(17):3932–3939, September 2012.

[196] PJ Murphy and MS LaGrange. Raman spectroscopy of gold chloro-hydroxy speciation in fluids at ambient temperature and pressure: a re-evaluation of the effects of pH and chloride concentration. *Geochim. Cosmochim. Acta*, 62(21):3515–3526, 1998.

[197] Shouzhong Zou, Ho Yeung H. Chan, Christopher T. Williams, and Michael J. Weaver. Formation and Stability of Oxide Films on Platinum-Group Metals in Electrochemical and Related Environments As Probed by Surface-Enhanced Raman Spectroscopy: Dependence on the Chemical Oxidant. *Langmuir*, 16(2):754–763, January 2000.

[198] Xiaowei Zhang, Jing Li, Xiaofang Jia, Dongyue Li, and Erkang Wang. Full-featured electrochemiluminescence sensing platform based on the multichannel closed bipolar system. *Anal. Chem.*, 86(11):5595–5599, 2014.

[199] Eoin Sheridan, Dzmitry Hlushkou, Kyle N Knust, Ulrich Tallarek, and Richard M Crooks. Enrichment of cations via bipolar electrode focusing. *Anal. Chem.*, 84(17):7393–7399, September 2012.

[200] Haili He, Xiaolong Xu, and Yongdong Jin. Wet-chemical enzymatic preparation and characterization of ultrathin gold-decorated single glass nanopore. *Anal. Chem.*, 86(10):4815–4821, May 2014.

[201] Colin R. Crick, Pablo Albella, Binghao Ng, Aleksandar P. Ivanov, Tyler Roschuk, Michael P. Cecchini, Fernando Bresme, Stefan A. Maier, and Joshua B. Edel. Precise Attolitre Temperature Control of Nanopore Sensors using a Nanoplasmonic Bullseye. *Nano Lett.*, 15(1):553–559, 2015.

[202] William H Pitchford, Hyung-jun Kim, Aleksandar P Ivanov, Hyun-mi Kim, Jae-seok Yu, Robin J Leatherbarrow, Tim Albrecht, Ki-bum Kim, and Joshua B Edel. Synchronized Optical and Electronic Detection of Biomolecules Using a Low Noise Nanopore Platform. *ACS Nano*, 9(2):1740–1748, 2015.

[203] Liqiang Jing, Wei Zhou, Guohui Tian, and Honggang Fu. Surface tuning for oxide-based nanomaterials as efficient photocatalysts. *Chem. Soc. Rev.*, 42:9509–9549, 2013.

[204] Anneli Hoggard, Lin Yung Wang, Lulu Ma, Ying Fang, Ge You, Jana Olson, Zheng Liu, Wei Shun Chang, Pulickel M. Ajayan, and Stephan Link. Using the plasmon linewidth to calculate the time and efficiency of electron transfer between gold nanorods and graphene. *ACS Nano*, 7:11209–11217, 2013.

[205] Marissa Wood and Bo Zhang. Bipolar Electrochemical Method for Dynamic In Situ Control of Single Metal Nanowire Growth. *ACS Nano*, 9(3):2454–2464, 2015.

[206] Agnieszka Rutkowska, Kevin J Freedman, Justyna Skalkowska, Minjun Jun Kim, Joshua B. Edel, and Tim Albrecht. Electrodeposition and Bipolar Effects in Metallized Nanopores and Their Use in the Detection of Insulin. *Anal. Chem.*, 87(4):2337–2344, 2015.

[207] Ioana Dumitrescu, Robbyn K Anand, Stephen E Fosdick, and Richard M Crooks. Pressure-driven bipolar electrochemistry. *J. Am. Chem. Soc.*, 133(13):4687–4689, April 2011.

[208] Derek Stein, Maarten Kruithof, and Cees Dekker. Surface-Charge-Governed Ion Transport in Nanofluidic Channels. *Phys. Rev. Lett.*, 93(3):1–4, July 2004.

[209] Frank van der Heyden, Derek Stein, and Cees Dekker. Streaming Currents in a Single Nanofluidic Channel. *Phys. Rev. Lett.*, 95(11):9–12, September 2005.

[210] Ruoshan Wei, Thomas G. Martin, Ulrich Rant, and Hendrik Dietz. DNA Origami Gatekeepers for Solid-State Nanopores. *Angew. Chem., Int. Ed.*, 51(20):4864–4867, April 2012.

[211] A. Storm, J. Chen, H. Zandbergen, and C. Dekker. Translocation of double-strand DNA through a silicon oxide nanopore. *Phys. Rev. E*, 71(5):1–10, May 2005.

[212] Jiali Li and David S Talaga. The distribution of DNA translocation times in solid-state nanopores. *J. Phys. Condens. Matter*, 22(45):454129, November 2010.

[213] Song Liu, Bo Lu, Qing Zhao, Ji Li, Teng Gao, Yubin Chen, Yanfeng Zhang, Zhongfan Liu, Zhongchao Fan, Fuhua Yang, Liping You, and Dapeng Yu. Boron nitride nanopores: Highly sensitive DNA single-molecule detectors. *Adv. Mater.*, 25(33):4549–4554, 2013.

[214] Calin Plesa and Cees Dekker. Data analysis methods for solid-state nanopores. *Nanotechnology*, 26(8):84003, 2015.

[215] Aleksandar P Ivanov, Kevin J Freedman, Min Jun Kim, Tim Albrecht, and Joshua B Edel. High Precision Fabrication and Positioning of Nanoelectrodes in a Nanopore. *ACS Nano*, 8(2):1940–1948, January 2014.

[216] Agnieszka Rutkowska, Joshua B Edel, and Tim Albrecht. Mapping the Ion Current Distribution in Nanopore/Electrode Devices. *ACS Nano*, 7(1):547–555, December 2012.

[217] Guillaume a T Chansin, Jongin Hong, Jonathan Dusting, Andrew J DeMello, Tim Albrecht, and Joshua B Edel. Resizing metal-coated nanopores using a scanning electron microscope. *Small*, 7(19):2736–2741, October 2011.

[218] Yuhui He, Makusu Tsutsui, Chun Fan, Masateru Taniguchi, and Tomoji Kawai. Controlling DNA Translocation through Gate Modulation of Nanopore Wall Surface Charges. *ACS Nano*, 5(7):5509–5518, June 2011.

[219] Clemens Kubeil. The Role of Nanopore Geometry for the Rectification of Ionic Currents. *J. Phys. Chem. C*, 115(16):7866–7873, 2011.

[220] Dmitry Momotenko, Fernando Cortés-Salazar, Jacques Josserand, Shujuan Liu, Yuanhua Shao, and Hubert H Girault. Ion current rectification and rectification inversion in conical nanopores: a perm-selective view. *Phys. Chem. Chem. Phys*, 13(12):5430–5440, March 2011.

[221] Yi Li, F Nicoli, C Chen, L Lagae, Henny W Zandbergen, Cees Dekker, Pol Van Dorpe, and Magnus P Jonsson. Photoresistance Switching of Plasmonic Nanopores. *Nano Lett.*, 15(1):776–782, 2015.

[222] Magnus P Jonsson and Cees Dekker. Plasmonic Nanopore for Electrical Profiling of Optical Intensity Landscapes. *Nano Lett.*, 13(3):1029–1033, February 2013.

[223] Wei Guo, Ye Tian, and Lei Jiang. Asymmetric ion transport through ion-channel-mimetic solid-state nanopores. *Acc. Chem. Res.*, 46(12):2834–2846, 2013.

[224] M Nishizawa, V P Menon, and C R Martin. Metal nanotubule membranes with electrochemically switchable ion-transport selectivity. *Science (80-.).*, 268(5211):700–702, 1995.

[225] Z. Siwy. Ion-Current Rectification in Nanopores and Nanotubes with Broken Symmetry. *Adv. Funct. Mater.*, 16(6):735–746, April 2006.

[226] Laura Innes, Matthew R. Powell, Ivan Vlassiouk, Craig Martens, and Zuzanna S. Siwy. Precipitation-Induced Voltage-Dependent Ion Current Fluctuations in Conical Nanopores. *J. Phys. Chem. C*, 114(18):8126–8134, May 2010.

[227] Matthew R. Powell, Leah Cleary, Matthew Davenport, Kenneth J. Shea, and Zuzanna S. Siwy. Electric-field-induced wetting and dewetting in single hydrophobic nanopores. *Nat. Nanotechnol.*, 6:798–802, October 2011.

[228] Francesca Nicoli, Daniel Verschueren, Misha Klein, Cees Dekker, and Magnus P. Jonsson. DNA Translocations through Solid-State Plasmonic Nanopores. *Nano Lett.*, 14(12):6917–6925, 2014.

[229] Lydéric Bocquet. Nanofluidics: bubbles as osmotic membranes. *Nat. Nanotechnol.*, 9(4):249–251, 2014.

[230] R. Smeets, U. Keyser, M. Wu, N. Dekker, and C. Dekker. Nanobubbles in Solid-State Nanopores. *Phys. Rev. Lett.*, 97(8):1–4, August 2006.

[231] Gaku Nagashima, Edlyn V. Levine, David P. Hoogerheide, Michael M. Burns, and Jene a. Golovchenko. Superheating and Homogeneous Single Bubble Nucleation in a Solid-State Nanopore. *Phys. Rev. Lett.*, 113(2):024506, July 2014.

[232] Z. Siwy, I. Kosińska, A. Fuliński, and C. Martin. Asymmetric Diffusion through Synthetic Nanopores. *Phys. Rev. Lett.*, 94(4):048102, February 2005.

[233] Ye Ai, Mingkan Zhang, S.W. Joo, M.A. Cheney, and Shizhi Qian. Effects of electroosmotic flow on ionic current rectification in conical nanopores. *J. Phys. Chem. C*, 114(9):3883–3890, 2010.

[234] Wiktoria Walczyk and Holger Schönherr. Characterization of the Interaction between AFM Tips and Surface Nanobubbles. *Langmuir*, 30(24):7112–7126, June 2014.

[235] Maria Holmberg, Anders Ku, Jø rgen Garnæ s, and Knud A Mø rch. Nanobubble Trouble on Gold Surfaces. *Langmuir*, 19(25):10510–10513, 2003.

[236] Nikolai F Bunkin, Stanislav O Yurchenko, Nikolai V Suyazov, and Alexey V Shkirin. Structure of the nanobubble clusters of dissolved air in liquid media. *J. Biol. Phys.*, 38(1):121–152, January 2012.

[237] Shangjiong Yang, Stephan M Dammer, Nicolas Bremond, Harold J W Zandvliet, E Stefan Kooij, and Detlef Lohse. Characterization of nanobubbles on hydrophobic surfaces in water. *Langmuir*, 23(13):7072–7077, June 2007.

[238] SN Sergei N Smirnov, Ivan V Vlassiouk, and NV Nickolay V Lavrik. Voltage-gated hydrophobic nanopores. *ACS Nano*, 5(9):7453–7461, August 2011.

[239] Jongho Lee, Tahar Laoui, and Rohit Karnik. Nanofluidic transport governed by the liquid/vapour interface. *Nat. Nanotechnol.*, 9:317–323, March 2014.

[240] Chenglong Zhao, Yuliang Xie, Zhangming Mao, Yanhui Zhao, Joseph Rufo, Shikuan Yang, Feng Guo, John D Mai, and Tony Jun Huang. Theory and experiment on particle trapping and manipulation via optothermally generated bubbles. *Lab Chip*, 14(2):384–391, January 2014.

[241] Chenglong Zhao, Yongmin Liu, Yanhui Zhao, Nicholas Fang, and Tony Jun Huang. A reconfigurable plasmofluidic lens. *Nat. Commun.*, 4:2305, January 2013.

[242] Changjun Min, Zhe Shen, Junfeng Shen, Yuquan Zhang, Hui Fang, Guanghui Yuan, Luping Du, Siwei Zhu, Ting Lei, and Xiaocong Yuan. Focused plasmonic trapping of metallic particles. *Nat. Commun.*, 4:2891, 2013.

[243] Abhay Kotnala and Reuven Gordon. Quantification of high-efficiency trapping of nanoparticles in a double nanohole optical tweezer. *Nano Lett.*, 14(2):853–856, 2014.

[244] Abhay Kotnala, Skyler Wheaton, and Reuven Gordon. Playing the notes of DNA with light: extremely high frequency nanomechanical oscillations. *Nanoscale*, 7:2295–2300, 2015.

Scientific Contributions

Journal contributions

1. **Li, Y.**; Nicoli, F.; Chen, C.; Lagae, L.; Groeseneken, G.; Stakenborg, T.; Zandbergen, H.; Dekker, C.; Van Dorpe, P.; Jonsson, M. Photoresistance Switching of Plasmonic Nanopores. *Nano Lett.* **2015**, *15* (1), 776-782.

2. **Li, Y.**; Chen, C.; Kerman, S.; Neutens, P.; Lagae, L.; Groeseneken, G.; Stakenborg, T.; Van Dorpe, P. Harnessing Plasmonic Induced Ionic Noise in Metallic Nanopores. *Nano Lett.* **2013**, *13* (4), 1724-1729.

3. Li, J.; Ye, J.; Chen C.; **Li, Y.**; Verellen, N.; Moshchalkov, V.; Lagae, L.; Van Dorpe, P. Revisiting the surface sensitivity of nanoplasmonic biosensors, *ACS Photonics* **2015**, *2* (3), 425–431.

4. Chen, C.; Juan, M. L.; **Li, Y.**; Maes, G.; Borghs, G.; Van Dorpe, P.; Quidant, R. *Nano Lett.* **2012**, *12* (1), 125–132.

5. Chen, C.; Ye, J.; **Li, Y.**; Lagae, L.; Stakenborg, T.; Van Dorpe, P. *IEEE J. Sel. Topics Quantum Electron.* **2012**, 99.

6. **Li, Y.***; Chen, C.*; Lagae, L.; Groeseneken, G.; Stakenborg, T.; Van Dorpe, P. Probing Local Potential in Metallic Nanopores by EC-SERS. *in preparation.* (*equally contributions)

7. **Li, Y.**; Jonsson, M.; Chen, C.; Willems, K.; Cornelissen, S.; Neutens, P.; Lagae, L.; Groeseneken, G.; Stakenborg, T.; Zandbergen, H.; Dekker, C.; Van Dorpe, P. Tailoring the Ionic Characteristics of Metallic Nanopores for Single Molecule Sensing. *in preparation.*

8. Chen, C.*; **Li, Y.***; Kerman, S.; Neutens, P.; Willems, K.; Cornelissen, S.; Lagae, L.; Stakenborg, T.; Van Dorpe, P. Nanopore fluidic SERS for single bases detection on a single stranded DNA. *in preparation.* (*equally contributions)

Conference contributions

1. **Li, Y.**; Chen, C.; Willems, K.; Kerman, S.; Lagae, L.; Groeseneken, G.; Stakenborg, T.; Van Dorpe, P. Probing the Local Potential in Metallic Nanopores by ElectroChemical Active Surface Enhanced Raman Spectroscopy (EC-SERS). *Nanoplasmonics - Faraday Discussion 178.* London, United Kingdom, 16-18 February **2015**.

2. **Li, Y.**; Chen, C.; Jonsson, M.; Nicoli, F.; Willems, K.; Kerman, S.; Lagae, L.; Groeseneken, G.; Stakenborg, T.; Zandbergen, H.; Dekker, C.; Van Dorpe, P. Plasmonic-fluidic hybrid nanopores. *Biophysical Society 59th Annual Meeting.* Baltimore, United States, 7-11 February **2015**.

3. Kerman, S.; Chen, C.; **Li, Y.**; Lagae, L.; Stakenborg, T.; Van Dorpe, P. Raman Spectroscopy and Optical Trapping of 20 nm Polystyrene Particles in Plasmonic Nanopores. *Nanophotonics V: Vol. 9126. Conference on Nanophotonics V.* Brussels, Belgium, 13-17 Apr **2014** (pp. 912612-912612).

4. Li, J.; Chen, C.; **Li, Y.**; Verellen, N.; Lagae, L.; Van Dorpe, P. Investigation of the correlation between the bulk and surface sensing performance in plasmonic crystals. *Nanophotonics V: Vol. 9126. Conference on Nanophotonics V.* Brussels, Belgium, 13-17 Apr **2014** (pp. 91261P-91261P).

5. Chen, C.; **Li, Y.**; Kerman, S.; Neutens, P.; Maes, G.; Lagae, L.; Stakenborg, T.; Van Dorpe, P. Plasmonic nanoslit for Fluidic SERS: a Strategy towards Genome Sequencing. *13th IEEE Conference on Nanotechnology (IEEE-NANO).* Beijing, China, 5-8 Aug **2013** (pp. 553-556).

6. Malachowski, K.; Verbeeck, R.; Dupont, T.; Chen, C.; **Li, Y.**; Musa, S.; Stakenborg, T.; Tezcan, D.; Van Dorpe, P. Wafer Scale Processing of Plasmonic Nanoslit Arrays in 200 mm CMOS Fab Environment. *ECS Transactions: Vol. 50 (12). ECS Fall Meeting Symposium J6: Microfabricated and Nanofabricated Systems for MEMS/NEMS.* Honolulu, United States, 7-12 Oct **2012** (pp. 413-422).

7. Chen, C.; Juan, M.; **Li, Y.**; Lagae, L.; Quidant, R.; Van Dorpe, P. Engineered plasmonic nanoslit-cavity for optical trapping and molecular sensing. *MRS Spring Meeting Symposium N: Control of Light at the Nanoscale.* Strasbourg, France, 14-18 May **2012**.

8. **Li, Y.**; Chen, C.; Cornelissen, S.; Neutens, P.; Musa, S.; Lagae, L.; Groeseneken, G.; Stakenborg, T.; Van Dorpe, P. Asymmetric current response in a metallic nanoslit. *Nanopore Conference.* Lanzarote, Spain, 2-7 February **2012**.

Curriculum Vitae

Date of birth:: Feb 20th, 1985

Place of birth:: Tianjin, China

Educations

- 2010-2015: Ph.D. in Electrical Engineering, KU Leuven / imec, Belgium
- 2007-2010: M.Sc. in Biomedical Engineering, Zhejiang University, China
- 2003-2007: B.Sc. in Biomedical Engineering, Zhejiang University, China

Awards

- The imec Scientific Excellence Award (2014-2015)

FACULTY OF ENGINEERING SCIENCE
DEPARTMENT OF ELECTRICAL ENGINEERING
MICAS DIVISION
Kasteelpark Arenberg 10
B-3001 Heverlee
Yi.Li@imec.be